TU
TECHNISCHE
UNIVERSITÄT
WIEN
Vienna University of Technology

Diplomarbeit

Characterization of CFRP (Carbon Fiber Reinforced Polymers) –

Influence of defects on material properties

Ausgeführt zum Zwecke der Erlangung des akademischen Grades eines Diplom-Ingenieurs unter der Leitung von

Univ.Ass. Mag.rer.nat. Marta Rodriguez-Hortala
E 308
Institut für Werkstoffwissenschaft und Werkstofftechnologie

und

O.Univ.Prof. Dipl.-Ing. Dr.techn. Hans-Peter Degischer
E 308
Institut für Werkstoffwissenschaft und Werkstofftechnologie

eingereicht an der Technischen Universität Wien
Fakultät für Maschinenwesen und Betriebswissenschaften

Michael Holzmeier
Matrikelnummer: 0325824

Auhofstraße 231/3/7
1130 Wien

Wien, am 25.05.2011   _____

Acknowledgments

Abstract

Because of their high stiffness and strength in combination with low weight, fiber reinforced polymers (FRP) are used commonly. Though design, dimensioning and manufacturing of such structures varies a lot compared to monolithic light weight materials like aluminum alloys for example. Whilst dimensioning using finite element methods is no longer a big issue, the correlation between voids, which are always inherent in composite structures, and their effect on the types of failure of fiber com²posite components are still not entirely investigated. Two unidirectional carbon fiber reinforced plastic (UD-CFRP) laminates produced by hand lay-up technique and hot pressing, having different porosity content, and furthermore pultruded tubes are studied within this thesis. Therefore, the composites' architecture is analyzed (light microscopy, scanning electron microscopy and computed tomography) to identify and characterize existing defects within the microstructure of the samples. Furthermore the mechanical parameters like Young's, and shear modulus, stress and strain at failure are determined by bending and torsion tests. Thermal parameters like glass transition temperature and coefficient of thermal expansion are studied using DMA, DSC and TMA. Bending and torsion tests with acoustic emission (AE) measurements reveal local damage much earlier than global failure. The different amounts of porosity of the two laminates underline the importance of the adequate curing cycle. The stiffness is 15% higher and the strength 16% higher in case of laminates with a lower fraction of porosities tested parallel to the fiber orientation. The step by step damage of the material using load cycles cannot be verified. Fractographic investigation of the damaged samples reveals the different appearance of the laminates compared to the pultruded tubes. Moreover typical fractographic features of the tension and compression face, like cusps, DAFF (Directly Attributed Fiber Failure), scallops, kinkband terraces and ply splitting of the bending sample are shown. Thermal testing illustrates the different area of application considering the temperature as the glass transition temperature of the tubes is around 80°C and therefore much lower compared to the glass transition temperature of the laminates (208°C). Though results of the glass transition temperature measured in three different ways show a wide scatter of the values of about $\pm 15\%$. Dilatometry (TMA) illustrates the orthotropic material behavior. Due to the negative coefficient of thermal expansion (CTE) of the carbon fiber the overall CTE of the material is 0µm/m°C parallel to the fiber direction and 28µm/m°C perpendicular to the fiber direction.

Zusammenfassung

Faserverstärkte Kunststoffe werden aufgrund ihrer hohen Steifigkeit und Festigkeit bei sehr geringem Gewicht immer häufiger eingesetzt. Die Auslegung, Berechnung und Fertigung solcher Strukturen unterscheidet sich aber wesentlich von derer monolithischer Leichtbauwerkstoffe wie zum Beispiel Aluminiumlegierungen. Während die Dimensionierung mithilfe finiter Elemente Methoden mittlerweile kein Hindernis mehr darstellt, sind die Zusammenhänge der unterschiedlichen Fehler, welche in Verbund-Bauteilen immer vorhanden sind, und die daraus resultierende Versagensart noch nicht gänzlich erforscht. In der hier vorliegenden Arbeit wird deshalb das Versagen von zwei handlaminierten und heiß gepressten, unidirektional-kohlefaserverstärkten Kunststofflaminaten, mit unterschiedlichem Porenanteil (Lufteinschlüsse), sowie von pultrudierten Rohren erforscht. Hierfür werden die Materialien zunächst mithilfe von bildgebenden Methoden (Lichtmikroskopie, Rasterelektronenmikroskopie und Computer Tomographie) untersucht, um die vorhandenen Defekte identifizieren und charakterisieren zu können. Durch mechanische Prüfung (Biegung und Torsion) werden die Materialparameter wie der Elastizitäts- und Schubmodul, die Bruch-Biege- und Torsionsspannung, sowie Bruchdehnungen bestimmt. Mittels thermischer Analysen (DMA, DSC und TMA) werden Kennwerte wie die Glasübergangstemperatur und der Wärmeausdehnungskoeffizient bestimmt, um eine möglichst vollständige Materialcharakterisierung zu erhalten. Die mechanischen Versuchsreihen werden jeweils auch mit akustischen Emissionsmessungen durchgeführt, da das erste, lokale Versagen bei derartigen Materialien schon weitaus früher auftritt, als das globale. Der unterschiedliche Porengehalt der beiden Laminate zeigt die Wichtigkeit des richtigen Aushärtezyklus auf. Ebenso sind die Steifigkeitswerte um bis zu 17% und die Festigkeitswerte um bis zu 16% höher im Falle geringerer Porosität. Der Schädigungsfortschritt in den Proben mit Hilfe von stufenweise ansteigenden Belastungszyklen kann nicht bestätigt werden. Fraktographische Untersuchungen an geschädigten Proben zeigten das unterschiedliche Erscheinungsbild der pultrudierten Proben im Vergleich zu den laminierten Proben. Des Weiteren konnten die typischen unterschiedlichen Bruchmerkmale wie cusps, DAFF (Directly Attributed Fiber Failure) und scallops auf der Zugseite, und Knickbänder und Matrixbruch auf der Druckseite der Biegeproben gezeigt werden. Die thermische Analyse veranschaulicht das unterschiedliche Temperatur-Einsatzgebiet der beiden Materialien, da die Glasübergangstemperatur der Rohre mit 80°C weit unter der, der Laminate liegt (208°C). Jedoch zeigten die Ergebnisse der Glasübergangstemperatur der drei unterschiedlichen Messmethoden eine relative große Streuung von bis zu ±15%. Dilatometerversuche (TMA) illustrieren das orthotrope Ausdehnungsverhalten des Materials. Aufgrund des negativen Ausdehnungskoeffizienten der Kohlefaser entlang der Faserrichtung beträgt die Gesamtausdehnung der Proben in diese Richtung 0μm/m°C und quer dazu 28μm/m°C.

1 Introduction

1.1 Historical Evolution of Fiber Reinforced Materials

Fiber reinforced materials are not a human invention since similar structures already existed millions of years ago [1]. The oldest analogon found in nature may be wood with its fibrous cellulose embedded in lignin as a kind of matrix material arranged in cylindrical shapes. But also more difficult lay ups can be found in nature. Figure 1-1 a) shows a longitudinal section of a bamboo stick. It appears very similar to a 0°/90° continuous carbon fiber/epoxy resin laminate given in figure 1-1 b). Another example of a unidirectional (UD) reinforcement is depicted in figure 1-1 c) showing the cross section of a Paracortex-cell of merino wool. Also the human body uses this "technology" as bones consist of fibers arranged in a way to absorb stresses best possibly.

a)   b)   c)
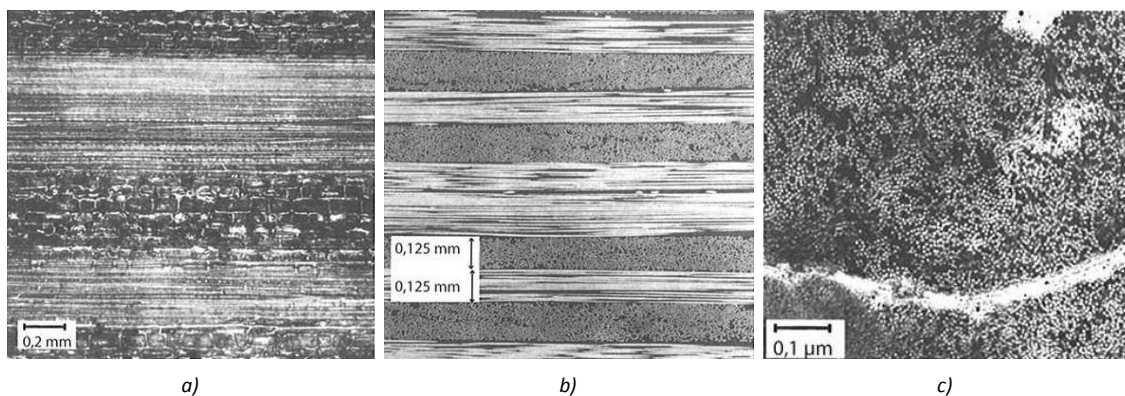
Fig. 1-1 a): Longitudinal section of a bamboo stick [1]
b): 0°/90° carbon fiber/epoxy resin laminate [1]
c): Cross section of a Paracortex-cell of merino wool [1]

First technical application was the use of paper reinforced phenol-resin plates for the construction of sailplane wings (1936). Six years later (1942) unsaturated polyester resin reinforced with glass fiber, originally used for electrical isolation, was employed for airplanes. These discontinuous FRP (fiber reinforced polymers) exhibited unsatisfactory mechanical properties caused by the vast shrinking of the polymer leading to poor bonding between fibers and resin. Further improvement was achieved by implementation of epoxy resins but the real breakthrough came along with the enhancement of polymers at the beginning of the 20th century [1]. Since then the use of CFRP (carbon fiber reinforced polymer) is increasing steadily as given in figure 1-2, showing the use of CFRP by means of Airbus' product families. The mass fraction of CFRP applied in airplanes started at 5% in the early 1970s and reached 30% with the A400M launched in 2008. Meanwhile Boeings latest airliner 787 consists of 50% (weight) or 80% (volume) of composite material (fig. 1-3). In comparison to the predecessor, the Boeing 777, only 12% composite material was used [31].
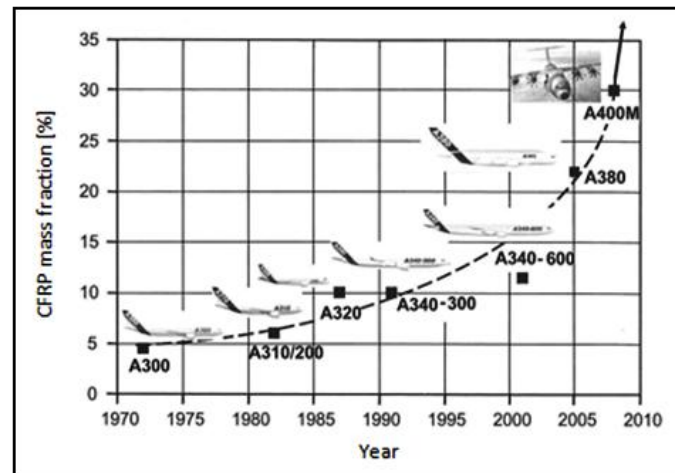
Fig. 1-2: CFRP mass fraction in Airbus' product family [1]
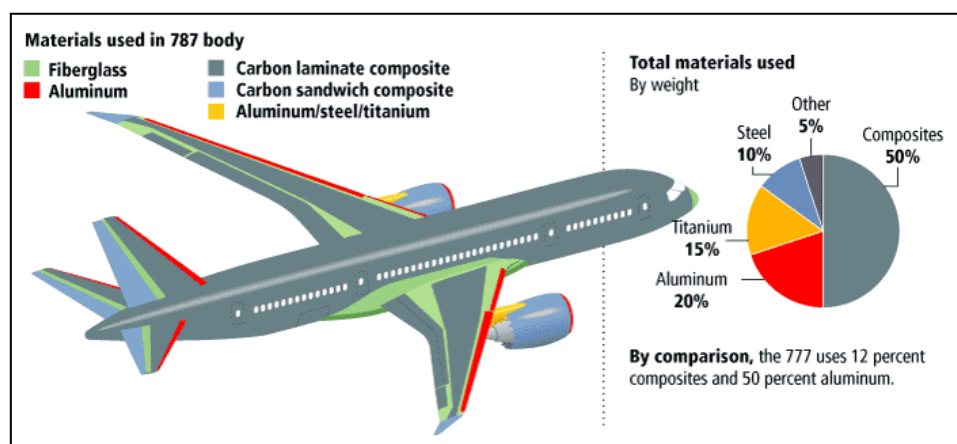
Fig. 1-3: Materials used for Boeings' 787 [31]

1.2 Materials and Properties of Fiber Reinforced Materials

Meanwhile a wide range of reinforcement fibers and matrix materials are used. Figure 1-4 gives an overview about the classification of fibers and table 1-2 comprises the material properties of the most important fibers [30]. Glass and ceramic fiber show isotropic material behavior whilst the others exhibit anisotropic material behavior due to their molecular structure. This is clearly demonstrated by the Young's modulus and the coefficient of thermal expansion (CTE) parallel (0°) and perpendicular (90°) to the fiber orientation. The Young's modulus can be two orders of magnitude lower perpendicular to the fibers compared to the modulus alongside the fibers. Especially the CTE alongside the fiber is remarkable as the fiber contracts when exposed to elevated temperature. Furthermore natural fibers like flax and hemp are used as demand for renewable materials is increasing. For use in high temperature applications ceramic fibers like aluminum oxide and silicon carbide are employed.
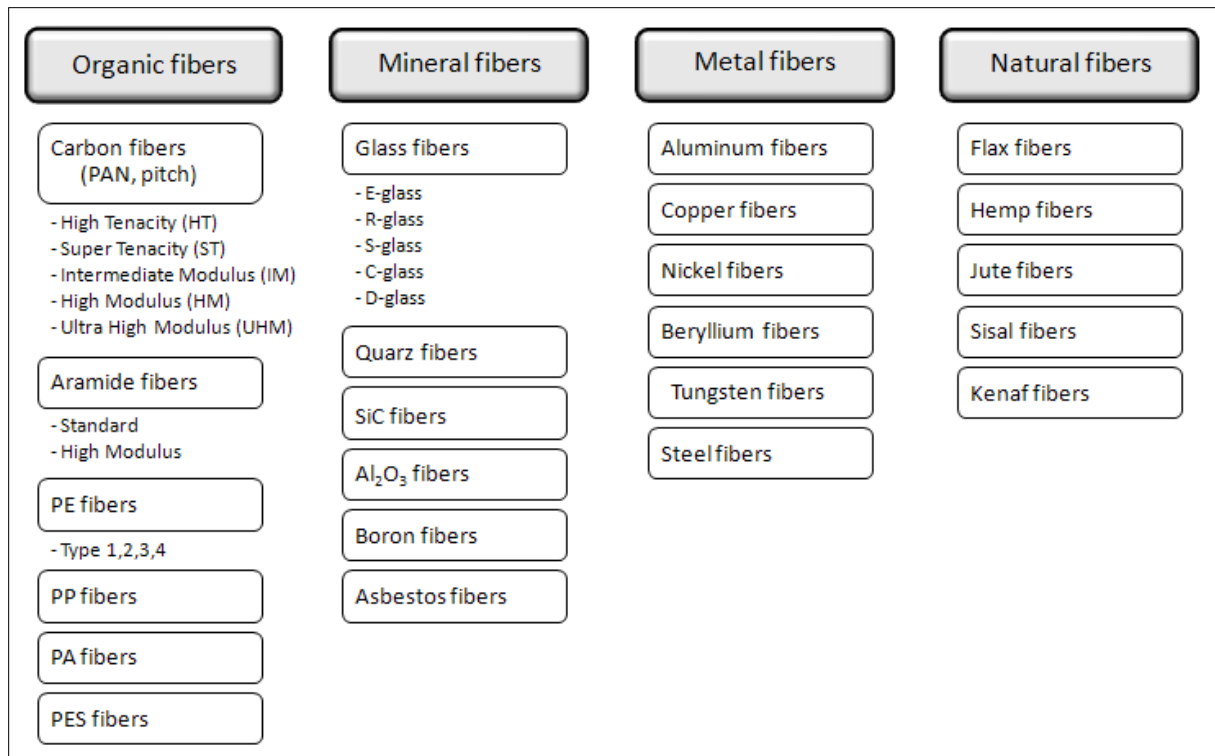
Fig.1-4: Classification of fibers according to [30]

Fiber type	Density [g/cm³]	Young's modulus (0°) [GPa]	Young's modulus (90°) [GPa]	Poisson's ratio	Tensile strength [GPa]	Coefficient of thermal expansion (0°) [10^{-6}/°C]	Coefficient of thermal expansion (90°) [10^{-6}/°C]
Glass	2,1 - 2,5	55 - 85	55 - 85	0,22	1,7 - 4,5	5,1	3,5 - 7,2
Carbon	1,7 - 1,9	230 - 450	15 - 28	0,20	2,1 - 4,5	-1,1 - -0,5	12,5 - 31
Aramide	1,5	67 - 130	5,4	0,32	2,8 - 3,6	-2	12,5 - 17
PBO	1,5	180 - 270	1,8	0,34	5,8	-6	-
PE	0,97	89 - 116	-	-	2,7- 3,6	-12	-
Flax	1,0 - 1,5	22 - 37	-	-	0,4 - 0,7	-	-

Tab. 1-2: Important material properties of reinforcement fibers. Average values taken from [30]

Matrix materials can be distinguished in polymer-, metal-, ceramic-, glass- and carbon systems. Polymer matrix systems can be split into thermosets, thermoplastics and elastomer matrix systems. Elastomer matrix composites are only applied for components exposed to uni-, or bi-axial tensile stress like timing belts, conveyor belts, tires or pressure hoses. The matrix used is usually defined by the mechanical and thermal requirements but also chemical resistance and pot-life can be restrictive parameters. The advantage of thermosets over thermoplastics is the easy processing as most of them offer low viscosity also at room temperature. Examples of thermosets are: epoxy-, unsaturated polyester-, vinyl ester- and phenol resin. Thermoplastic matrix systems used are: Polypropylene (PP),

polyethylene terephthalate (PET), polyamide (PA), polyphenylene sulfide (PPS) and polyether ether ketone (PEEK).

1.3 Production of CFRP

A huge variety of manufacturing processes has been developed depending on the materials used, product geometry, manufacturing costs and so on. The most common processes for continuous CFRP according to [22] are:

- − Hand lay-up technique
- − Vacuum bag molding
- − Autoclave curing
- − Resin transfer molding
- − Pressure molding
- − Thermal expansion molding
- − Resin injection molding
- − Winding technique
- − Pultrusion method

Details of the manufacturing processes relevant for this thesis are given in chapter 4.1. The others are well described in [2].

1.4 Application of CFRP

Due to their cost intensive production CFRP, at the beginning, were used for aviation and space applications only. But as new production methods were developed and demand increased steadily, CFRP are nowadays found in a wide range of application fields. The main advantages of CFRP are their high strength and stiffness combined with a low density. Figure 1-6 depicts the specific strength and stiffness of steel, aluminum and titanium compared to glass-, aramide-, PE- and carbon-fiber in longitudinal direction.
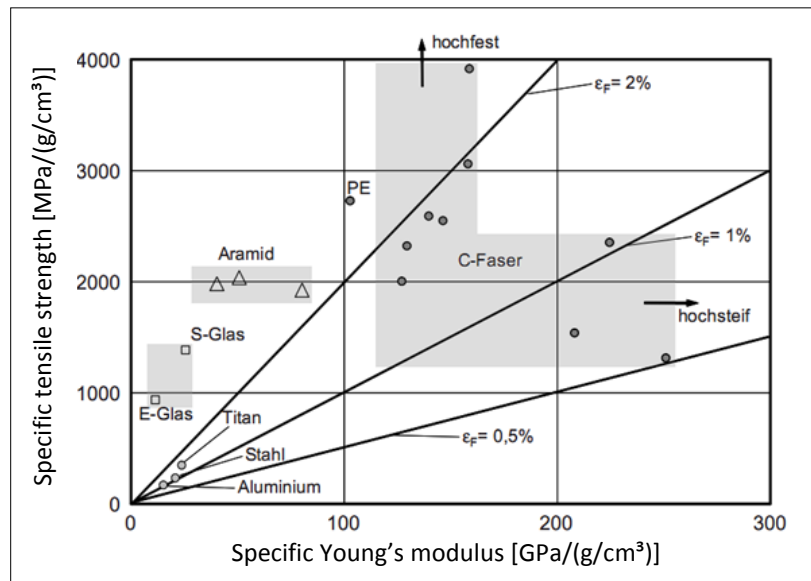
Fig. 1-6: Illustration of specific stiffness and strength of steel, aluminum and titanium compared with common fiber materials in longitudinal direction [8]

1.4.1 Aviation Industry

At the beginning continuous GFRP (glass fiber reinforced polymers) were used instead of wood due to better weather resistance, smooth surface and constant material properties. Initially only applied for low loaded cover panels or interior application they were later used for load bearing primer structures. Meanwhile fuel consumption plays an important role forcing the industry to work on fuel saving engines as well as to further reduce the overall weight of their aircrafts which is realized by the replacement of light metals by FRP as given in figure 1-2 and 1-3.

1.4.2 Automotive Industry

Especially the possibility of creating complex shapes was the driving force for the automotive industry to employ FRP. Thus it did not last long until this material found its way from airplanes to trains, buses and automobiles. Driver cabs and cover panels for trains and self supporting omnibus trims can be found as well as CFRP monocoques for racing cars. Moreover drive shafts and leaf springs made of continuous CFRP are solved engineering problems.

1.4.3 Sports Industry

CFRP are meanwhile used for badminton and tennis rackets, bicycle frames and components, skis snowboards and many other applications. Despite the smooth surface and the low density optical appearance is the most important reason especially for the use of CFRP. Furthermore continuously reinforced GFRP are used for nearly every type of boat hulls and also sails are produced out of FRP.

1.4.4 Further Applications

Mechanical engineers deployed FRP for fast moving and/or accelerated systems like wind turbines, welding-, and assembling-robots. Moreover CFRP pressing-rolls are used because of the low moment of inertia and the high stiffness. Pipeline constructions benefit from the good resistance to most chemicals and due to the electrical isolation of GFRP they are widely used for printed circuit boards and other electrical applications. Latest efforts are made in the field of protheses were CFRP are used as artificial shanks or ankles.

2 State of the Art

J. M. Hodgkinson [4] gives the best overview of the different mechanical test methods and procedures including problem solving and data analysis and should therefore be mentioned first. J. P. Hou and C. Ruiz [33] showed that the strain rate plays an important role when testing matrix dominated parameters like compression strength, Poisson's ratio, in-plane shear modulus and shear strength whilst fiber dominated parameters like tensile modulus and strength are strain rate independent. K. Morioka, Y. Tomita [34] proved the influence of the lay-up sequence on the mechanical properties and the different fracture behavior of $(0/0)_S$, $(0/90)_S$ and $(0/90/\pm45)_S$ laminates. The index "s" means symmetrical laminate lay-up. Intralaminar fracture toughness tests combined with acoustic emission (AE) measurements have been performed by M. Iwamoto et al. [28] using three different types of unidirectional CFRP (epoxy 3601/T300/62,5f-UD, epoxy 3631/T800/61,0f-UD, epoxy 1908/AS4/62,0f-UD) showing the effect of bridging fibers on the intralaminar fracture toughness. Further tests using the AE technique have been carried out by M.Bourchak et al. [10], testing woven CFRP under tensile load, finding, that first AE events can already be recorded at 27% of the ultimate tensile strength. M. Surgeon and M. Wevers [12] revealed CFRP characteristics using modal acoustic emission (MAE) testing. Latest efforts were made manufacturing composites using carbon nanotubes (CNT). N. G. Sahooa et al. [35] demonstrated that the tensile modulus of PU can be increased by a factor of five and the tensile strength by a factor of four using CNT. J. N. Coleman [36] as well depicted the improved material parameters of polymers filled with carbon nanotubes. Investigations in the field of simulation and non destructive testing (NDT) were carried out by G. Busse et al. [32]. Emile S. Greenhalgh [3] extensively studied the failure mechanism of a variety of composites and H. Huang and R. Talreja [37] determined the "Effects of void geometry on elastic properties of unidirectional fiber reinforced composites".

3 Experimental

3.1 Material

3.1.1 Material Production

3.1.1.1 Laminates

All laminates were manufactured at IMDEA Materials in Madrid by hand lamination and hot pressing using Hexcel HexPly® AS4/8552 RC34 AW194 unidirectional (UD) prepregs with a nominal fiber volume fraction of 58%. AS4 is a high strength carbon fiber and 8552 identifies the epoxy resin. The endless fiber reinforced prepreg was stored at -18°C and cut manually into pieces of 200x200mm, stacked and pressed at 0,2MPa for about three hours using two different temperature cycles. Both the C0 and the C3 laminates were heated up to 180°C at 10°C/min but cooled at 8°C/min to different temperature levels, 110°C and 130°C. After maintaining this temperature level for 10 minutes the laminates were heated up to 180°C again at 8°C/min and kept at this temperature for 120 minutes after being cooled down to room temperature at 10°C/min. Figure 3-1 shows these two curing cycles.
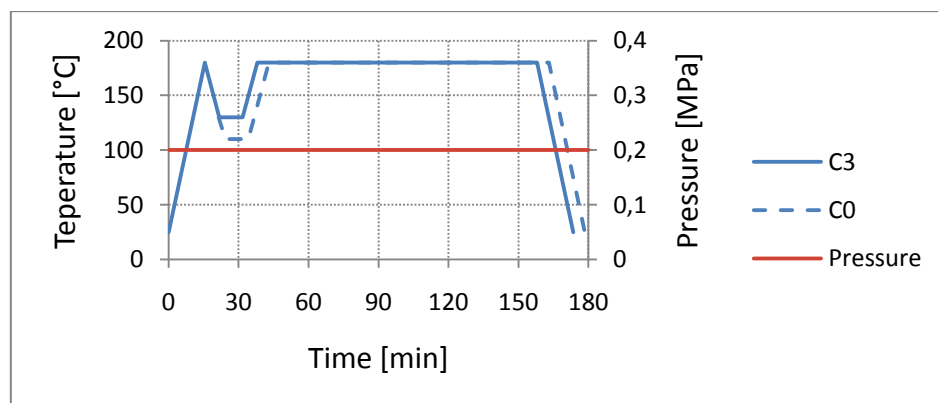
Fig. 3-1: Curing cycle of laminates C0 and C3

3.1.1.2 Tubes

The pultruded tubes were delivered by SECAR Technologie GmbH in Mürzzuschlag. Pultrusion is a continuous process to manufacture a variety of profiles with a constant cross section. Fiber bundles are pulled through a resin bath before entering the heated die that cures the material. The last step is the cutting of the material which is done by a simple cut off saw [2]. The original sample length was 1000mm. The reinforcement fiber is Tenax® STS40 F13 high tenacity carbon fiber surrounded by epoxy resin L20 [26]. Figure 3-2 gives a schematic view of a pultrusion process [22].

Fig. 3-2: Layout of a pultrusion process [22]

3.1.2 Sample Description

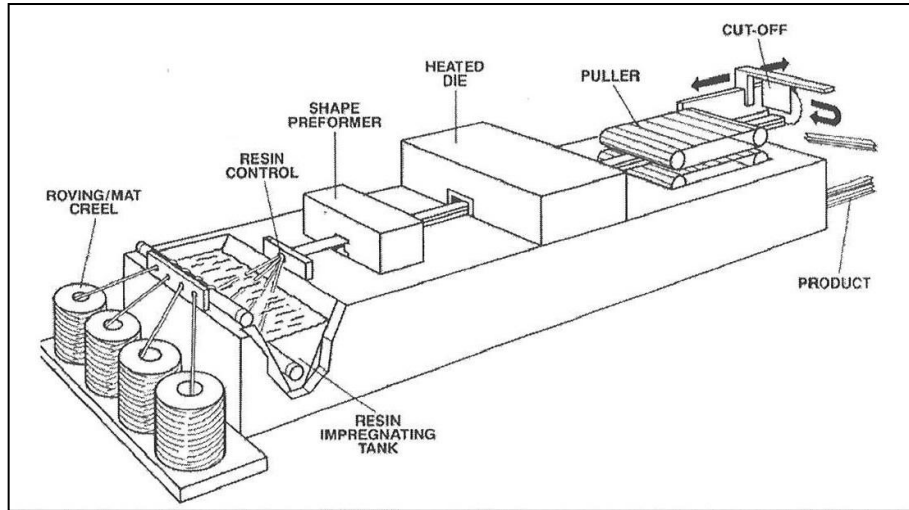Table 3-1 shows the significant data of the samples studied within this thesis. The only difference between samples "A" and "B" is the number of layers used for manufacturing. Information about the fibers and the neat resin according to the datasheets [24, 26] is given in tables 3-2 and 3-3 respectively.

Sample code	Matrix	Fiber	Fiber orientation	Number of layers	Nominal thickness (mm)	Manufacturing process, product	Nominal fiber fraction (volume %)
A-C0	HexPly 8552	HS AS4	UD 0°	10	2	Hand lamination - hot pressing, plate	58[1]
A-C3	HexPly 8552	HS AS4	UD 0°	10	2		58[1]
B-C0	HexPly 8552	HS AS4	UD 0°	16	3		58[1]
B-C3	HexPly 8552	HS AS4	UD 0°	16	3		58[1]
P10	L20	HT Tenax STS	UD 0°	-	$\emptyset_o$ = 10 $\emptyset i$ = 8	Pultrusion, tube	60[2]

[1] According to Hexcel HexPly® AS4/8552 RC34 AW194 data sheet [24]

[2] According to Secar Technology GmbH, Mürzzuschlag

Table 3-1: Specimen data

Fiber type	Density [g/cm²]	Nominal fiber diameter [µm]	Tensile strength [MPa]	Tensile modulus [GPa]	Failure strain [%]
AS4	1,79	7,1	4400	231	1,8
STS40 F13	1,77	7,0	4000	240	1,7

Table 3-2: Comparison of the fibers used for laminates and tubes according to the product datasheets [25, 27]

Resin type	Density [g/cm²]	Tensile strength [MPa]	Tensile modulus [GPa]
Hexply 8552	1,30	121	4,7
L20	1,15	70	3,4

Table 3-3: Comparison of the resins used for laminates and tubes according to the product datasheets [24, 26]

3.2 Microscopic Analysis

3.2.1 Light Optical Microscopy (LOM)

First characterization of the material was done by embedding samples of both types of laminates C0 and C3 and the pultruded tubes with fiber orientation of 0° and 90° in Araldit® epoxy resin. After several grinding and polishing steps (table 3-4) with a Struers Tegra Force-5 the samples were observed with a Zeiss Axioplan microscope at different magnifications. Picture processing was done using the programs "Image J" and "Axio Vision", both offering different advantages and disadvantages. The former was used to determine the fiber diameter and the fiber area fraction of the samples. The latter to calculate the porosity area fraction. To verify the nominal fiber diameter of 7,1µm, single fiber diameters were measured and the contrast (white: resin, black: fibers) of whole LOM pictures was analyzed automatically.

For automated measurements the following editing steps of the pictures were necessary and proceeded with "Image J" (fig. 3-3 to fig. 3-5):

1) Enhance contrast and brightness to an appropriate level (fig. 3-3 a, b)
2) Create a binary black and white picture (fig. 3-4 a, b)
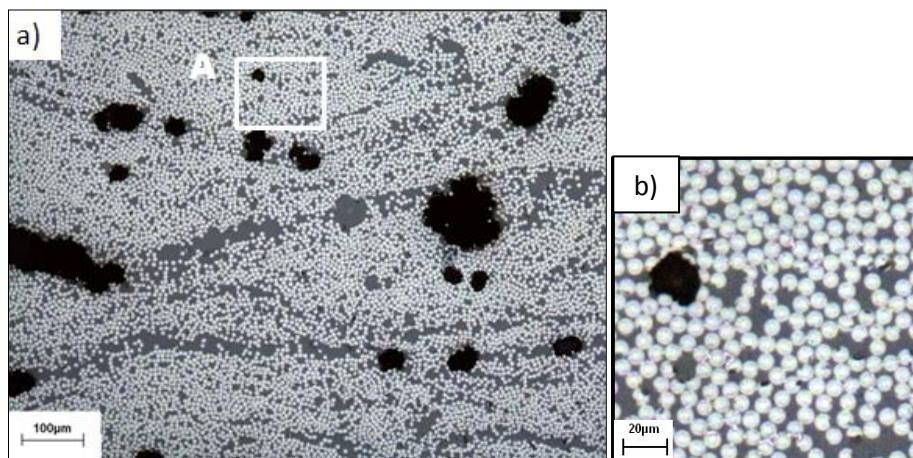3) Separate fibers by using the "Watershed" operation (fig. 3-5 a, b)

Fig. 3-3 a) Step 1: LOM picture with enhanced brightness and contrast
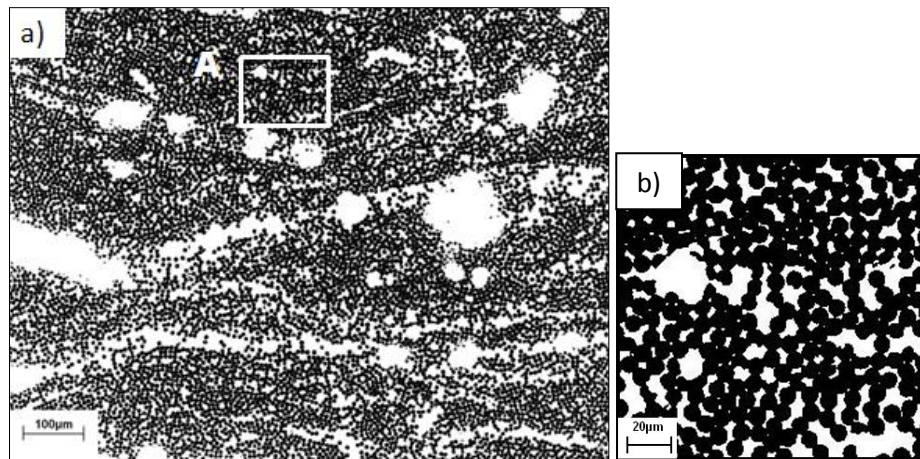*b) Detail A*

Fig. 3-4 a) Step 2: Binary black and white picture (white: resin and pores, black: fibers)
b) Detail A
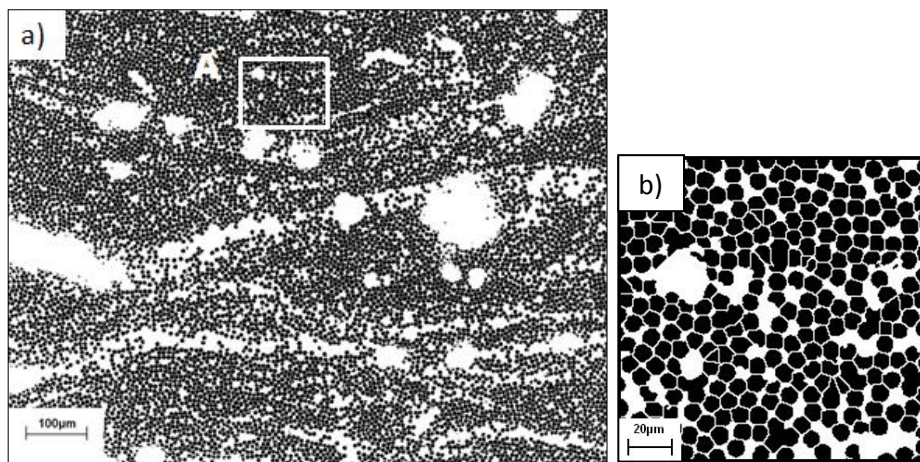
Fig.3-5 a) Step 3: Picture with again separated fibers
b) Detail A

To determine the porosity area fraction six single pictures were assembled to a panorama picture to analyze a bigger cross section. Figure 3-6 a) shows the original picture. In figure 3-6 b) the black specimen boarder has been removed not to be recognized by the program and figure 3-6 c) shows the voids segmented for evaluation (marked by green boundaries).

Fig. 3-6 a) Original LOM panorama picture

Fig. 3-6 b) Picture with removed black surrounding

Fig. 3-6 c) Voids found for evaluation (green boundaries)

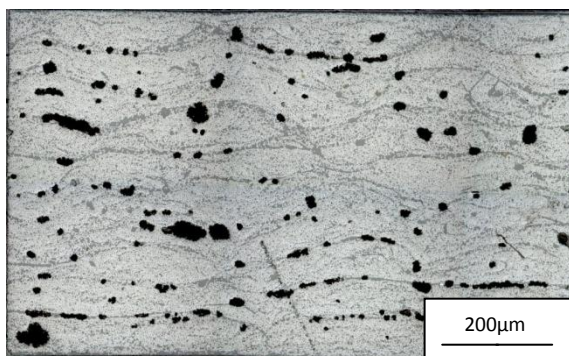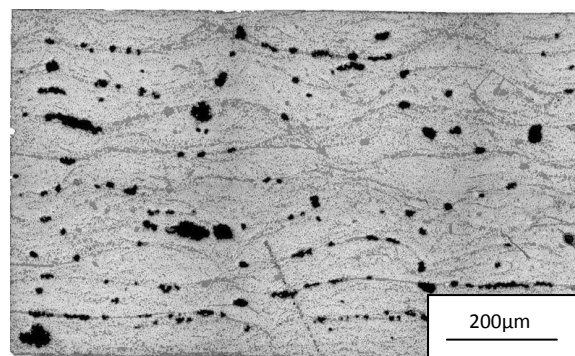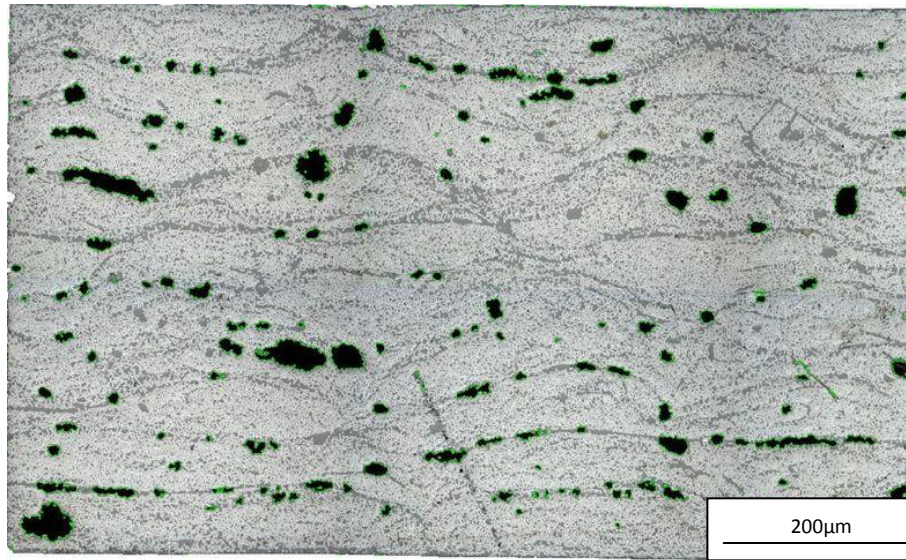| Step	Polishing Cloths	Lubricant	Suspension	Time (min)	Force (N)	Rotational speed (rpm)
1	SiC 320	Water	-	2	10/30	300
2	MD-largo	Struers blue	DP-9µm	8	30/180	150
3	MD-dur	Struers blue	DP-3µm	8	30/180	150
4	MD-nap	Struers red	DP-1µm	5	30/180	150
5	MD-chem	Water	OP-S	2	10/30	150
6	MD-chem	Water	-	2	10/30	150

Table 3-4: Details of the grinding and polishing steps for LOM sample preparation

3.2.2 Scanning Electron Microscopy (SEM) - Fractography

SEM analysis was used to observe of the fracture surfaces after mechanical testing (three point-, four point bending and torsion test) with a Philips XL 30 SE microscope (fig. 3-7). Samples were coated with a thin gold layer using an Agar Sputter Coater and an Edwards RV3 vacuum pump to achieve electrical conductivity and therefore enable SEM microscopy.

Fig. 3-7: Phillips XL 30 SE microscope [21]

3.2.3 Computed Tomography (CT)

To obtain three dimensional information about the microstructure of the samples X-ray CT scans were performed at the University of Applied Sciences Upper Austria using a Sub-µm-CT "Nanotom". Tubes were investigated before and after mechanical testing, laminates only after mechanical testing complementary to the 2D SEM fractography. CT data was also used to calculate the porosity volume fraction to be compared to the 2D data provided by LOM. Voxel size was $(9,5\mu m)^3$ in case of the laminates and $(12\mu m)^3$ in case of the tubular specimen providing a resolution of diameter >20µm and >30µm respectively.

3.3 Mechanical Analysis

3.3.1 Three Point Bending

To obtain the mechanical properties of the laminates, at first a three point bending test was performed. Although having the disadvantage of shear forces and a maximum bending moment only in the middle of the sample, this test was done to have comparable data for the following Dynamical Mechanical Analysis (DMA). The test was operated according to DIN EN ISO 14125 standard [5] on a Zwick Z050 testing assembly using fixed supports and a 50kN load cell. The test configuration is shown in figure 3-8. Samples tested had the following geometry: 100mmx15mmx1,8mm ($L_t$xbxh). And were tested parallel (0°) and perpendicular (90°) to the fiber orientation. Samples were loaded with a crosshead speed of 5mm/min until failure.
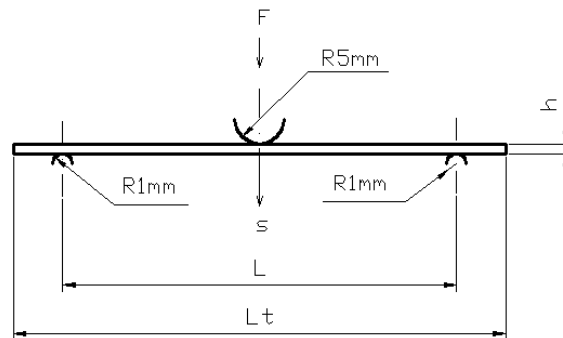

Fig. 3-8: Three point bending test setup and sample geometry

The applied force and the movement of the crosshead were measured and hence the flexural stress and strain were calculated using the following equations given in the standard [5].

$$\sigma_f = \frac{3FL}{2bh^2}\left[1 + 6\left(\frac{s}{L}\right)^2 - 3\left(\frac{sh}{L^2}\right)\right]$$

$$\varepsilon = 6\frac{sh}{L^2} + \frac{h}{L}\left[62{,}17\left(\frac{s}{L}\right)^5 - 24{,}37\left(\frac{s}{L}\right)^3\right]$$

σf ... Flexural stress [MPa] ε ... Flexural strain [%]
F ... Force [N] L ... Support span [=80mm]
b ... Sample width [mm] h ... Sample thickness [mm]
s ... Crosshead displacement [mm]

The term in square brackets is used because of high deflections. The Young's modulus was calculated as the quotient of the differences of the flexural stress and the strain of the outer fiber between 0,05% and 0,25% of the failure strain.

$$E_f = \frac{\sigma' - \sigma''}{10(\varepsilon' - \varepsilon'')}$$

Ef ... Young's modulus [GPa]
σ' ... Flexural stress at ε' [MPa] ε' ... 0,05% of the failure strain [%]
σ'' ... Flexural stress at ε'' [MPa] ε'' ... 0,25% of the failure strain [%]

The uncertainty of the measurement of the force, support span, sample width, sample thickness and the deflection affects the calculation of the flexural stress and strain and therefore as well the determination of the Young's modulus. By calculating the systematical error the quality of a measurement can be testified. The equations of the relative failure of the flexural stress, the flexural strain and the Young's modulus using the partial derivatives are given below.

$$\frac{\delta\sigma_f}{\sigma_f} = \frac{\delta F}{F} + \frac{\delta L}{L} + \frac{\delta b}{b} + 2\frac{\delta h}{h} + \frac{\delta K}{K}$$

The factor δK/K refers to the Term in square brackets and is separated into

$$a = 6\left(\frac{s}{L}\right)^2 \quad \text{and} \quad b = 3\left(\frac{sh}{L^2}\right)$$

With the use of these two new variables the factor δK/K can be calculated.

$$\frac{\delta K}{K} = \frac{\delta a + \delta b}{1 + 6\left(\frac{s}{L}\right)^2 - 3\left(\frac{sh}{L^2}\right)}$$

The absolute errors δa and δb equal

$$\delta a = 2a\left[\left(\frac{\delta s}{s}\right) + \left(\frac{\delta L}{L}\right)\right]$$

$$\delta b = b\left[\left(\frac{\delta s}{s}\right) + \left(\frac{\delta h}{h}\right) + 2\left(\frac{\delta L}{L}\right)\right]$$

The relative failure of the flexural strain can be calculated in the same way.

$$\frac{\delta \varepsilon}{\varepsilon} = \frac{\delta s}{s} + \frac{\delta h}{h} + 2\frac{\delta L}{L} + \frac{\delta J}{J}$$

The factor δJ/J refers to the term in square brackets and is again separated into

$$c = 62{,}17\left(\frac{s}{L}\right)^5 \quad \text{and} \quad d = -24{,}37\left(\frac{s}{L}\right)^3$$

With the use of these two new variables the factor δJ/J can be calculated.

$$\frac{\delta J}{J} = \frac{\delta c + \delta d}{62{,}17\left(\frac{s}{L}\right)^5 - 24{,}37\left(\frac{s}{L}\right)^3}$$

The absolute errors δc and δd equal

$$\delta c = 3c\left[\left(\frac{\delta s}{s}\right) + \left(\frac{\delta L}{L}\right)\right]$$

$$\delta b = 5d\left[\left(\frac{\delta s}{s}\right) + \left(\frac{\delta L}{L}\right)\right]$$

Consequently the relative failure of the Young's modulus can be calculated as

$$\frac{\delta E_f}{E_f} = \frac{2\delta \sigma}{\sigma' - \sigma''} + \frac{2\delta \varepsilon}{\varepsilon' - \varepsilon''}$$

The estimated measurement errors and the results of the relative error calculation for the three point bending test are given in table 3-5.

δF [%]	δL [mm]	δb [mm]	δh [mm]	δs [mm]	$\delta\sigma_f/\sigma_f$ [%]	$\delta\varepsilon/\varepsilon$ [%]	$\delta E_f/E_f$ [%]
± 0,05	± 0,01	± 0,01	± 0,01	± 0,01	± 1,3	± 0,7	± 7

Table 3-5: Errors of the measurement readings (force F, support span L, sample width b, sample thickness h and deflection s) and results of the relative error calculation of the flexural stress, flexural strain and Young's modulus

3.3.2 Four Point Bending

The four point bending test bears the advantage of a constant bending moment between the two pressure rams and consequently uniform shear forces and shear stresses. The test was done according to the DIN EN ISO 14125 standard on a Zwick Z050 testing assembly using fixed supports, a 50kN load cell and a crosshead speed of 5mm/min. Sample geometry was the same as in case of the three point bending test 100mmx15mmx1,8mm ($L_t$xbxh fig.3-9). The test configuration is shown in figure 3-9. One aim of this thesis was to show the gradual damage of the specimen during testing using load cycles and acoustic emission (AE) measurements (see chapter 3.3.4). Therefore first results were evaluated after three loading-unloading steps with the reversal points at 300, 600 and 850N. Further samples were tested using nine loading-unloading cycles. In this case the reversal points were 300, 600, 700, 750, 800, 850, 900, 950 and 1000N. Crosshead speed was again 5mm/min.
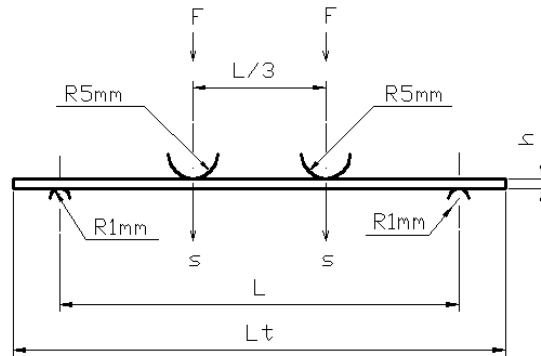

Fig. 3-9: Four point bending test setup and sample geometry

The applied force and the movement of the crosshead were measured and hence the flexural stress and strain were calculated using the following equations given in the standard [5].

$$\sigma_f = \frac{FL}{bh^2}$$

$$\varepsilon = \frac{540sh}{L^2}$$

σ_f ... Flexural stress [MPa] ε ... Flexural strain [%]

F ... Force [N] L ... Support span [=81mm]

b ... Sample width [mm] h ... Sample thickness [mm]

s ... Crosshead displacement [mm]

As the formula for high strain leads to unrealistic results it was not employed in case of the four point bending test. The Young's modulus was either calculated as the quotient of the differences of the flexural stress and the strain of the outer fiber between 0,05% and 0,25% of the failure strain or as secant modulus between the reversal points considering testing with hysteresis loops.

$$E_f = \frac{\sigma' - \sigma''}{10(\varepsilon' - \varepsilon'')}$$

E_f … Young's modulus [GPa]

σ' … Flexural stress at ε' [MPa]

σ'' … Flexural stress at ε'' [MPa]

ε' … 0,05% of the failure strain, or strain at the lower reversal point considering loading with hysteresis loops

ε'' … 0,25% of the failure strain, or strain at the upper intersection point considering loading with hysteresis loops

The uncertainty of the measurement of the force, support span, sample width, sample thickness and the deflection affects the calculation of the flexural stress and strain and therefore as well the determination of the Young's modulus. By calculating the systematical error the quality of a measurement can be testified. The equations of the relative failure of the flexural stress, the flexural strain and the Young's modulus using the partial derivatives are given below.

$$\frac{\delta\sigma_f}{\sigma_f} = \frac{\delta F}{F} + \frac{\delta L}{L} + \frac{\delta b}{b} + 2\frac{\delta h}{h}$$

$$\frac{\delta\varepsilon}{\varepsilon} = \frac{\delta s}{s} + \frac{\delta h}{h} + 2\frac{\delta L}{L}$$

$$\frac{\delta E_f}{E_f} = \frac{2\delta\sigma_f}{\sigma' - \sigma''} + \frac{2\delta\varepsilon}{\varepsilon' - \varepsilon''}$$

The estimated measurement errors and the results of the relative error calculation of the four point bending test are given in table 3-6.

δF [%]	δL [mm]	δb [mm]	δh [mm]	δs [mm]	$\delta\sigma_f/\sigma_f$ [%]	$\delta\varepsilon/\varepsilon$ [%]	$\delta E_f/E_f$ [%]
± 0,05	± 0,01	± 0,01	± 0,01	± 0,01	± 1,2	± 0,6	± 6

Table 3-6: Errors of the measurement readings (force L, support span L, sample width b, sample thickness s and deflection s) and results of the relative error calculation of the flexural stress, flexural strain and Young's modulus

3.3.3 Torsion

The torsion tests were operated in cooperation with the TVFA (Technische Versuchs- und Forschungsanstalt GmbH der Technischen Universität Wien) on a universal torsion machine. To assure safe clamping of the specimen an aluminum plug was necessary not to destroy the samples as well as a slotted copper bush for sufficient friction and therefore avoid slippage between the steel grips and the samples (fig. 3-10). The clamping length L1 of the tube samples was between 135mm and 140mm, the total length Lt=200mm, the outer diameter D1=10mm and the inner diameter D2=8mm. The specimens were stressed either continuously until failure or using loading loops. In

both cases the twisting speed was 6°/min. The torque and the twist angle were recorded and the torsion stress-strain values were calculated according to the following equations [19].

$$\tau = \frac{16 M_t D_1}{\pi (D_1^4 - D_2^4)}$$

$$\gamma = \frac{D_1 \theta \pi}{180 L_1}$$

τ ... Torsion stress [MPa] γ ... Torsion strain [rad]

M_t ... Torque [Nm] θ ... Twisting angle [°]

D_1 ... Outer sample diameter [mm] L_1 ... Clamping length [mm]

D_2 ... Inner sample diameter [mm]

The shear modulus was calculated as the quotient of the differences of the shear stress and the strain between the reversal points of the load cycles or between 0,0025 and 0,0045rad of the shear strain without loading unloading cycles according to the following equation.

$$G = \frac{\tau' - \tau''}{\gamma' - \gamma''}$$

G ... Shear modulus [GPa]

τ' ... Torsion stress [MPa] at lower reversal point γ' ... Torsion strain [rad] at lower (reversal) point

τ'' ... Torsion stress [MPa] at upper reversal point γ'' ... Torsion strain [rad] at upper (reversal) point
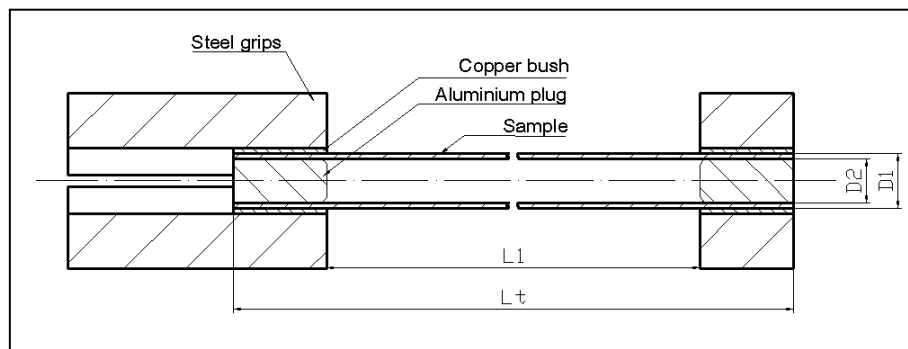

Fig. 3-10: Torsion test setup

The uncertainty of the measurement of the torque, sample diameters, twisting angle and the clamping length affects the calculation of the torsion stress and torsion strain and therefore as well the determination of the shear modulus. By calculating the systematical error the quality of a measurement can be testified. The equations of the relative failure of the torsion stress, the torsion strain and the shear modulus using the partial derivatives are given below.

$$\frac{\delta\tau}{\tau} = \frac{\delta M_t}{M_t} + \frac{\delta D_1}{D_1} + 4\frac{(\delta D_1 + \delta D_2)}{D_1^4 - D_2^4}$$

$$\frac{\delta\gamma}{\gamma} = \frac{\delta D_1}{D_1} + \frac{\delta\theta}{\theta} + \frac{\delta L_1}{L_1}$$

$$\frac{\delta G}{G} = \frac{2\delta\tau}{\tau' - \tau''} + \frac{2\delta\gamma}{\gamma' - \gamma''}$$

The estimated measurement errors and the results of the relative error calculation of the torsion test are given in table 3-7.

δM_t [%]	δD_1 [mm]	δD_2 [mm]	$\delta\Theta$ [°]	δL_1 [mm]	$\delta\tau/\tau$ [%]	$\delta\gamma/\gamma$ [%]	$\delta G/G$ [%]
± 0,1	± 0,01	± 0,01	± 0,001	± 0,01	± 0,1	± 0,1	± 4

Table 3-7: Errors of the measurement readings (torque M_t, outer sample diameter D_1, inner sample diameter D_2, twisting angle Θ and span length L_1) and results of the relative error calculation of the torsion stress, torsion strain and shear modulus

3.3.4 Acoustic Emission (AE) Measurements

To gain information about the damage occurring during mechanical loading a piezo electrical sensor (fig. 3-11) was placed on the sample to record sound waves in situ. The sensor was attached to an amplifier recording the AE signal at four different amplifications (fig. 3-12) permitting to choose the signal that fits best in accordance with the threshold. To ensure high quality of the measurement silicon paste was used as a couplant and a clamp or elastic band fixed the sensor on the test specimen. Signals were recorded during four point bending (fig. 3-13) and torsion (fig. 3-14) tests whilst continuous loading until failure and loading-unloading cycles with different hysteresis loops. Loading-unloading cycles were performed with continuous increase of the force level as well as loading of the specimen at the same level to determine the effects of friction.
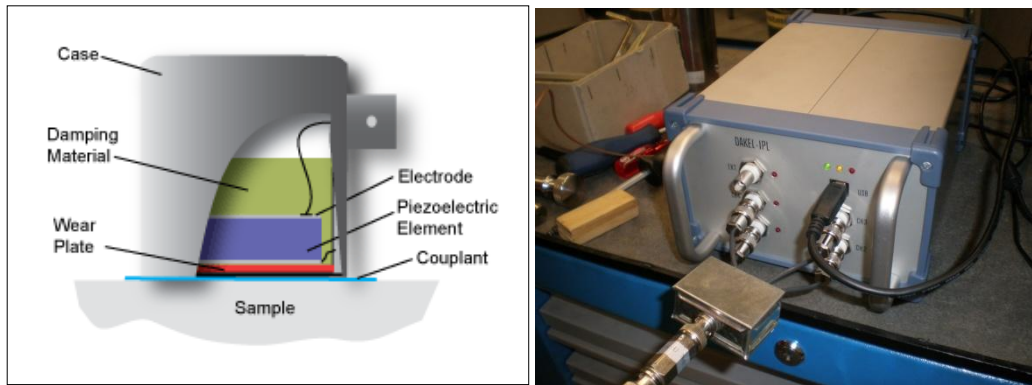
Left: Fig. 3-11: Components of a piezo electrical sensor [20]

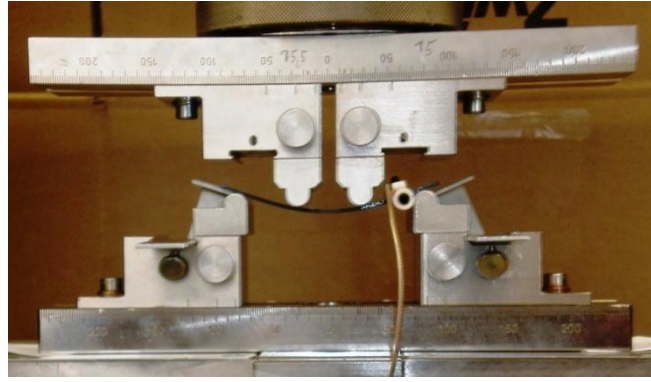Right: Fig. 3-12: Pre amplifier and main amplifier for acoustic emission measurements

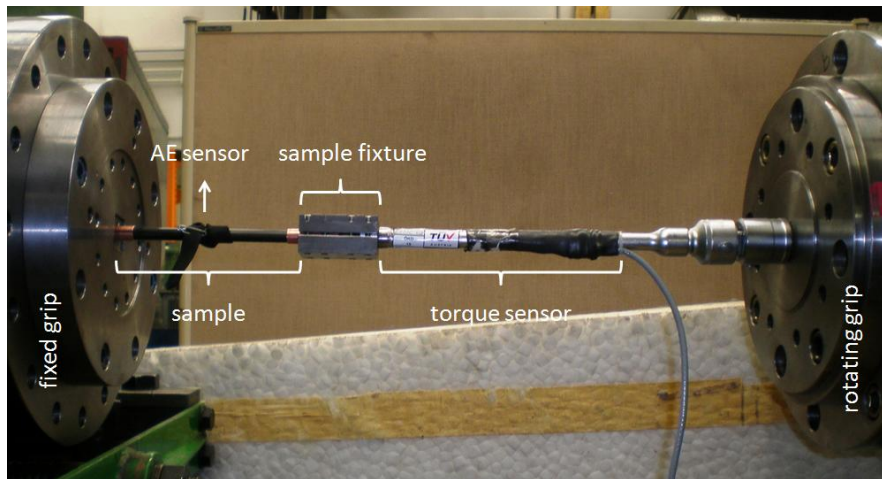*Fig. 3-13: Four point bending with acoustic emission measurement test setup*

Fig. 3-14: Torsion with acoustic emission measurement test setup

3.3.5 Interlaminar Fracture Toughness

3.3.5.1 Mode I

This test was performed in cooperation with IMDEA materials in Madrid according to the ASTM D 5528 standard [9] on an INSTRON 3384 universal testing machine using a double cantilever beam (DCB). As the same samples were employed for mode I and II tests the original sample dimensions were 200mmx25mmx3mm. A 3µm thin and 25mm long PTFE foil was embedded in the middle of the 16 layers across the whole width of the specimen simulating an initial crack. Furthermore two loading blocks were adhesively bonded to the samples using Loctite Hysol® 9466 A&B two component Epoxy adhesive. Therefore the surface was roughened with adhesive paper to apply the glue and cured for at least 10 hours at room temperature. Moreover the specimen sides were painted white and a blue ink scale improved crack length measurements. Figure 3-15 shows a drawing of the specimen ready for testing and figure 3-16 the clamped specimen.
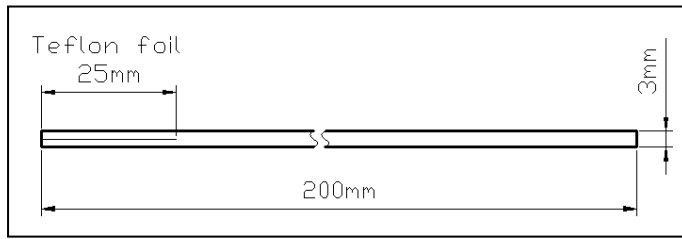
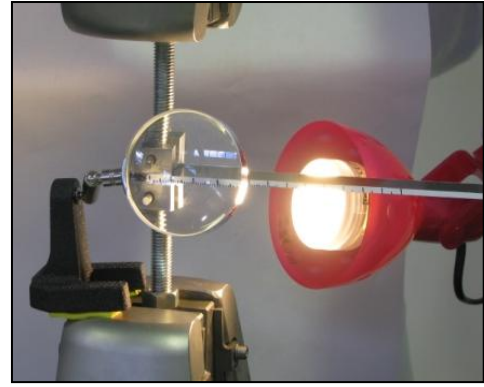*Fig. 3-15: Sample geometry for IFT mode I*   *Fig. 3-16: IFT mode I test set up*

After mounting the sample in the test machine it was loaded until the crack reached a total length of 30mm. Subsequently the sample was unloaded and loaded again until the crack propagated another 10mm. The procedure was repeated four times resulting in a final crack length of 70mm. Testing speed was 1mm/min. To ensure easy handling and accurate precision of the crack propagation measurement a magnifying glass was used.

Load and displacement during the test were recorded and thus the critical interlaminar fracture toughness G_{Ic} was calculated according to the following equation. The area underneath the curve was approximated by a rectangle.

$$G_{Ic} = \frac{A}{a * w}$$

G_{Ic} ... Critical interlaminar fracture toughness mode I [J/mm²]
A ... Total approximated area underneath the force-displacement diagram [J]
a ... Total crack growth [mm]   *w ... Sample width [mm]*

3.3.5.2 Mode II

This experiment was also carried out in cooperation with IMDEA materials in Madrid using a INSTRON 3384 universal testing machine. The Interlaminar fracture toughness test mode II follows a three point bending test using an end notched flexure (ENF) specimen (fig. 3-17). Therefore samples from mode I test were cut in length to leave an initial crack of 40mm and were stressed continuously with a deformation speed of 1mm/min until crack propagation occurred. The flexural load and the displacement were recorded during the test and hence the critical fracture toughness G_{IIc} was calculated according to the following equation.

$$G_{IIc} = \frac{9Pa^2d}{2w(0{,}25L^3 + 3a^{3})}$$

G_{IIc} ... Critical fracture toughness mode II [J/mm²]

P ... Flexural load [N]   *w ... Sample width [mm]*

a ... Initial crack length [mm]   *L ... Span length [mm]*
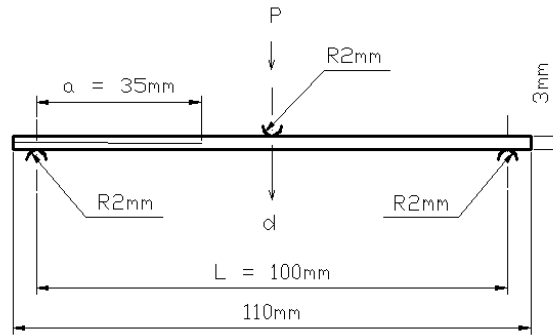
d ... Displacement [mm]

Fig. 3-17: Test specimen for IFT mode II

3.4 Thermo-Mechanical Analysis

3.4.1 DMA (Dynamic Mechanical Analysis)

DMA is a method to measure mechanical and thermal parameters of materials under thermal and cyclic mechanical loading. With the use of different fixtures a wide range of mechanical tests, like compression, tension, shear or flexural tests, can be carried out [13, 15].

Due to the viscoelastical behavior of CFRP the frequency of the stress and strain curves are equal but a phase shift between them can be determined as seen in figure 3-18. The lag of the strain ranges between 0°, for ideal elastic material, and 90°, for ideal viscous material.
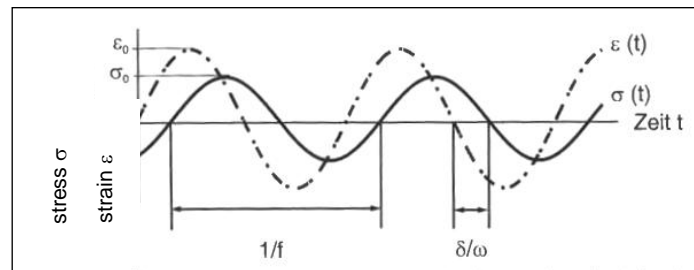

Fig. 3-18: Loss factor tan δ due to the lag of the strain [15]

Thus the complex modulus E* and the loss factor tan δ are defined as followed, according to [15]

$$E^* = E' + iE''$$

$$\tan \delta = \frac{E''}{E'}$$

where E' represents the real component, called storage modulus, and E'' the imaginary component, called loss modulus (fig. 3-19).
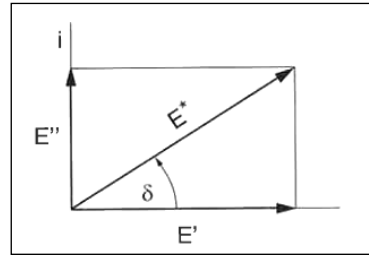

Fig. 3-19: Storage modulus E', loss modulus E'' and loss factor tan δ defining the complex modulus E [15]*

The test method used was a three point bending test on a TA Instruments 2980 dynamic mechanical analyzer. The three point bending fixture is given in figure 3-20 a). Sample geometry was 60mmx4mmx1,5mm, the amplitude of the deformation 70µm, the loading frequency 1Hz and the distance between the supports 50mm. Only laminates were analyzed using DMA. Samples C0 and C3-DMA-01 to 03 were tested without prior mechanical loading whereas samples C0 and C3-DMA-04 and 05 were loaded cyclic up to 90% of the maximum average bending force before DMA samples were cut out of the middle of the four point bending samples. Storage modulus, loss modulus and loss factor were recorded between 25 and 300°C with a heating rate of 5°C per minute. The parameters appraised were the storage modulus and the glass transition temperature. The latter was determined from the storage modulus (tangent at inflection point) as well as from the loss factor curves (maximum of loss factor) (fig. 3-20 b).
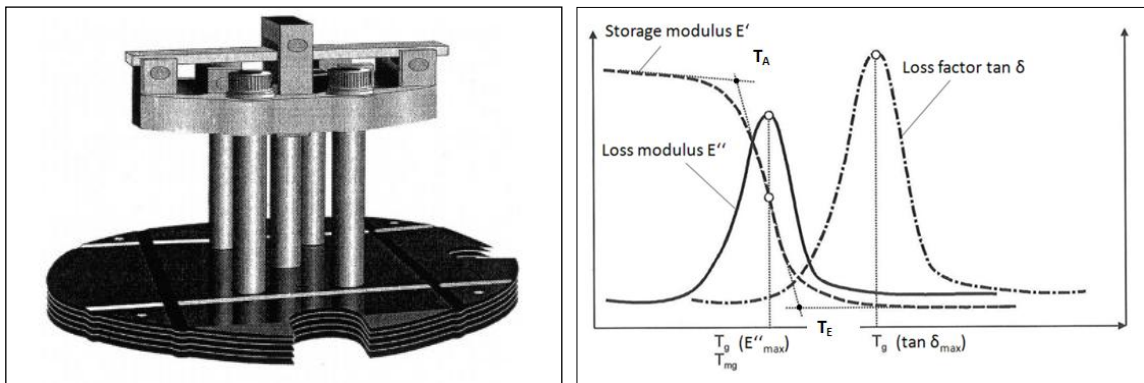
a)   *b)*

Fig. 3-20 a): Fixture of the TA Instruments 2980 for three point bending [18]

Fig. 3-20 b): Determination of the glass transition temperature with DMA [13]

3.4.2 DSC (Differential Scanning Calorimetry)

This method is used for thermoanalytic measurements whereby a sample and a reference with known specific heat capacity are heated and the input of heat is measured to keep the sample and the reference on the same temperature level. Hence endothermic (e.g.: melting, glass transition, vaporization) and exothermic (crystallization, polymerization, cross linking) processes can be described (fig. 3-21 a) [13, 15]. Figure 3-21 b) shows the principle assembly of a heat flow DSC chamber.
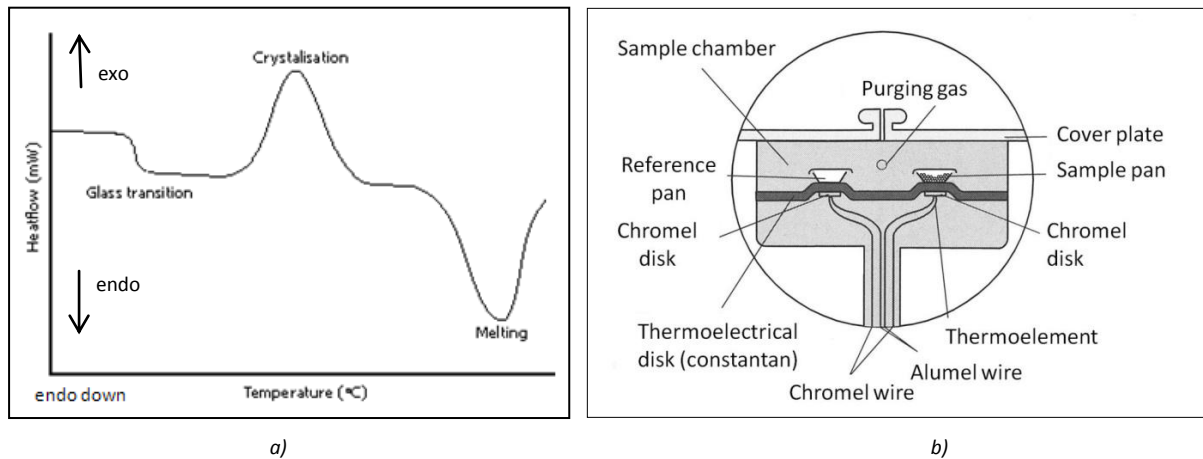

a)

b)

Fig. 3-21 a): schematic DSC curve showing glass transition, crystallization and melting [38]

Fig. 3-21 b): principle of a heat flow DSC chamber [15]

The system used was a TA Q2000 Calorimeter from TA Instruments. This system offers the opportunity of modulated DSC (MDSC) measurements. Thus the heat flow can be separated into a reversible and a non reversible part facilitating the evaluation as the step defining the glass transition temperature is more distinct in case of the reversible heat flow curve.

Specimen weight was around 20mg in case of the laminates and 15mg in case of the pultruded tubes. Slices were cut out using a circular saw and were grinded manually to be capsuled in standard aluminum pans afterwards. Temperature modulation was ±1°C/min and measurements took place between 25-300°C with a heating rate of 3, 5 and 10°C/min. The reference was an empty pan and therefore air.

3.4.3 Dilatometry

Coefficient of linear expansion measurement was done by TMA with the help of a TA Instruments TMA 2940 analyzer and a quartz glass probe. Sample dimension was 15mmx5mmx1,8mm for laminates and fiber orientation 0° or 90° (fig. 3-22 a). Thermal expansion measurement of the tubes alongside fiber orientation (0°) was done using 90° segments with a length of 15mm (fig. 3-22 b). To measure the expansion perpendicular to the fiber plane circular specimen were employed (fig 3-22 c). The temperature range for laminates C0 and C3 with 0° fiber orientation was

0-180°C and 0-300°C for laminates with 90° fiber orientation. Pultruded tubes were tested within a temperature range between 0-150°C for 0° and 0-200°C for 90° fiber orientation. After cooling the samples for 5 minutes at 0°C the specimens were heated at 3°C/min until the desired temperature was reached. According to the standard [7] measurements were repeated to ensure total curing of the samples to eliminate irreversible effects distorting the results. The coefficient of thermal expansion was measured at room temperature (25°C) and below glass transition temperature of the corresponding samples. For each specimen type three samples were tested whilst loaded with a constant force of 0,1N. The glass transition temperature was evaluated at the intersection of the tangent below and above the glass transition temperature.
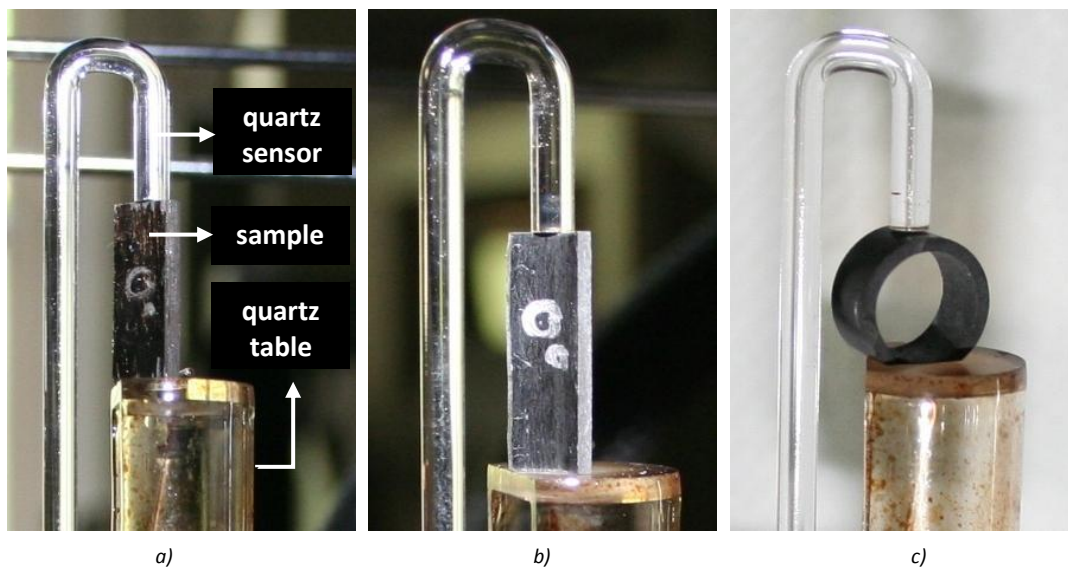
a)   b)   c)

Fig. 3-22: Samples fixed for dilatometry tests

a): Laminates for measurement parallel and perpendicular to the fiber direction had the same shape

b): 90° segment of the tubes for measurements parallel to the fiber direction

c): Circular specimen of the tubes for measurements perpendicular to the fiber direction

4 Results

4.1 Microscopic Analysis

4.1.1 Light Optical Microscopy (LOM)

Fiber diameter was measured using four different LOM samples. Two corresponding to curing cycle C0 and another two corresponding to curing cycle C3. Figures 4-1 a)-d) show the histograms of the automated measurement and table 4-1 the minimal, the maximal and the average value of the automatic and manual "Image J" measurement.

a)   b)

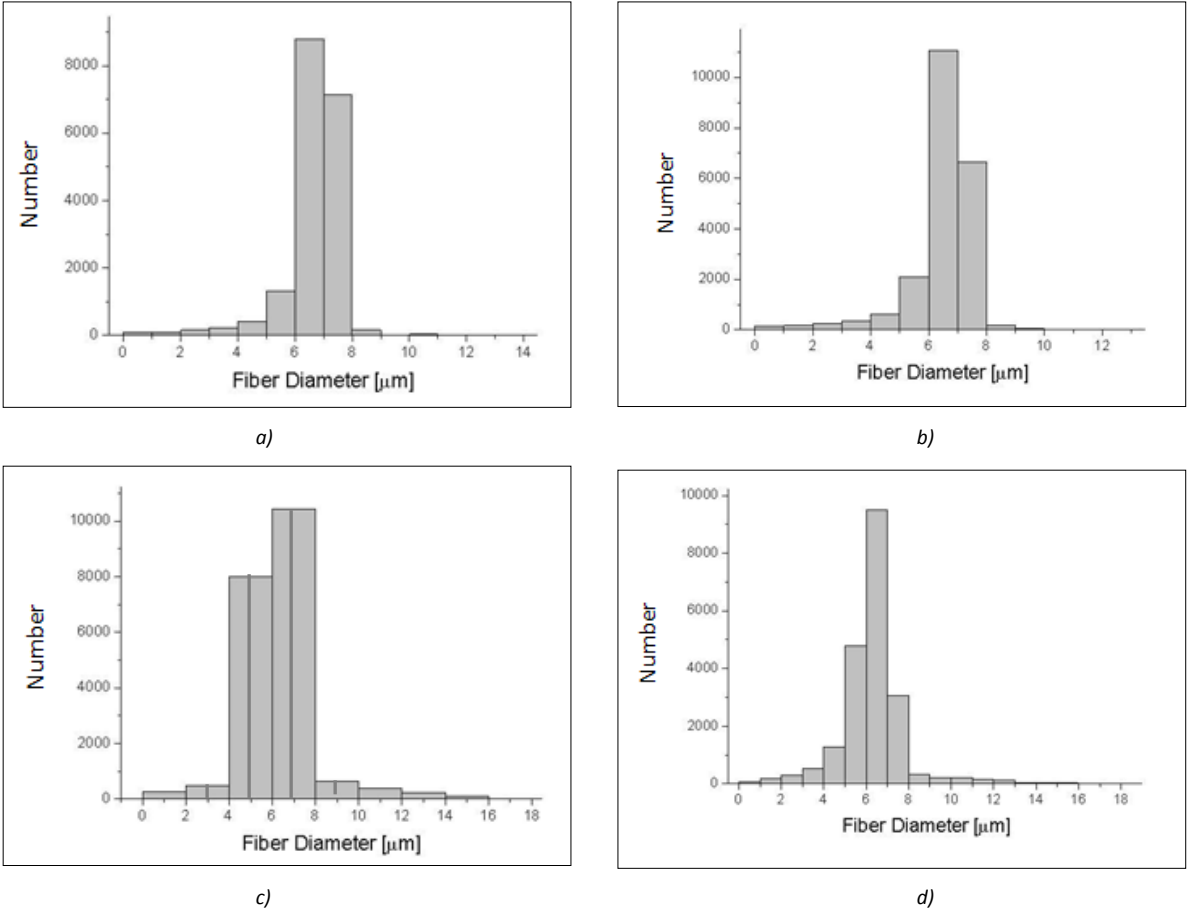c)   d)

Fig. 4-1: Histograms of the automatically measured fiber distribution

a) Sample C0-LOM01   b) Sample C0-LOM02

c) Sample C3-LOM01   d) Sample C3-LOM02

Sample code	Automatically measured fibers				Manually measured fibers			
	Number of fibers found	Min. fiber Ø [µm]	Max. fiber Ø [µm]	Average fiber Ø [µm]	Number of fibers measured	Min. fiber Ø [µm]	Max. fiber Ø [µm]	Average fiber Ø [µm]
C0-LOM01	18466	0,6	13,1	6,7 ± 1,1	40	6,2	8,0	7,1 ± 0,5
C0-LOM02	21557	0,6	12,8	6,6 ± 1,1	40	6,3	7,8	7,0 ± 0,4
C3-LOM01	20649	0,6	27,5	6,3 ± 1,6	40	6,5	7,9	7,2 ± 0,4
C3-LOM02	20912	0,6	23,9	6,3 ± 1,8	40	6,4	8,0	7,2 ± 0,4

Table 4-1: Results of the by-hand and automated measurement of the fiber diameter using "Image J"

Calculation of the fiber area fraction was done using the same samples. Table 4-2 gives the results of the fiber fraction using "Image J" as analyzing tool and the fiber fraction resulting from the number of fibers found times the nominal fiber diameter of 7,1µm [25].

Sample code	Number of fibers found	Area of fibers found [µm²]	Total picture area [µm²]	Fiber fraction Image J [%]	Mean fiber fraction [%]	Fiber fraction $\emptyset_f$ = 7,1 µm [%]	Mean fiber fraction [%]
C0-LOM01	18466	667*10³	1326*10³	50,3	50,7 ± 0,6	55,1	57,6 ± 3,5
C0-LOM02	21557	726*10³	1422*10³	51,1		60,0	
C3-LOM01	20649	702*10³	1453*10³	48,3	48,4 ± 0,1	56,3	56,6 ± 0,4
C3-LOM02	20912	704*10³	1455*10³	48,4		56,9	

Table 4-2: Results of the calculation of the fiber fraction using "Image J"

Evaluation of the porosity was executed on the same samples using panorama pictures consisting of six single. Table 4-3 contains the number, the total void area and the void fraction of the analyzed images obtained with "Axio Vision".

Sample code	Number of voids found	Total area of voids found [µm²]	Total picture area [µm²]	Void fraction [%]	Mean void fraction [%]
C0-Pan01	688	312*10³	7442*10³	4,2	4,0 ± 0,3
C0-Pan02	1305	259*10³	6817*10³	3,8	
C3-Pan01	248	101*10³	7275*10³	1,4	1,5 ± 0,1
C3-Pan02	315	128*10³	8540*10³	1,5	

Table 4-3: Results of the void fraction calculation using "Axio Vision"

Examples of the defects found in the specimens are specified in table 4-4 a) and b). Figures 4-2 a) - d) and figures 4-3 a) - c) present examples of the defects found.

Laminates	Figure
Resin rich areas (fiber free regions)	4-2 a): 1
Variation in fiber packing density	4-2 a): 2
Porosities	4-2 a): 3 4-2 b) 4-2 d)
Misaligned Fibers	4-2 c)

Table 4-4 a) Defects found in laminates

Tubes	Figure
Filler agglomerates (fiber free regions)	4-3 a) and c)
Porosities	4-3 a)
Variation in fiber packing density	4-3 b)
Fiber waviness	4-3 d)

Table 4-4 b) Defects found in pultruded tubes
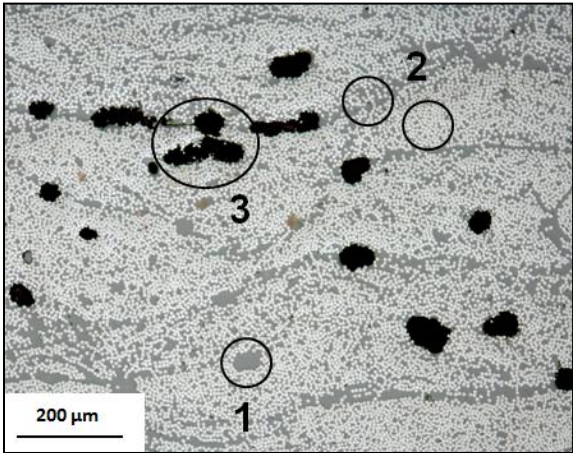
Fig. 4-2 a) Sample C0:
1: Resin rich areas
2: Variation in fiber packing density
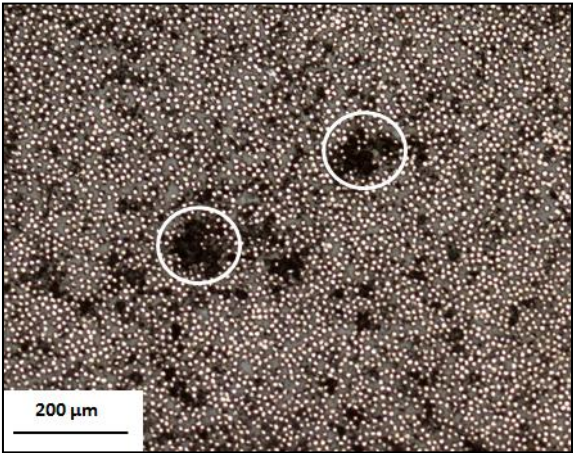*3: Macro porosities (> fiber diameter)*

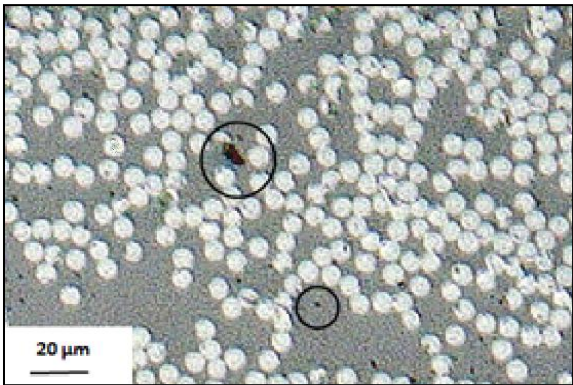*Fig. 4-3 a) Tube sample: Filler agglomerates combined with porosities*

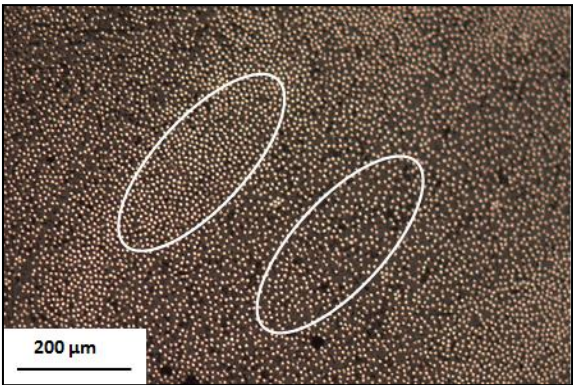Fig. 4-2 b) *Sample C0: Micro porosities (≤ fiber diameter)*

Fig. 4-3 b) Tube sample: Variation in fiber packing density
Upper left part: high fiber packing density
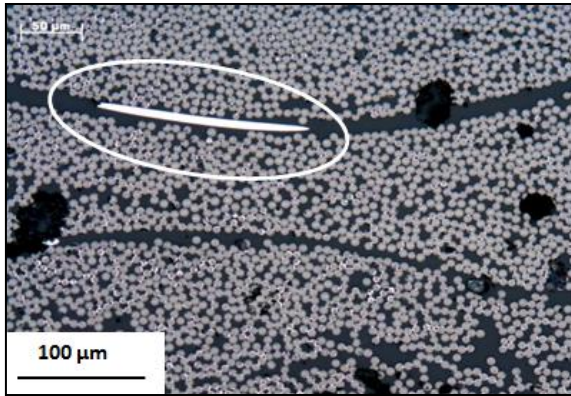*Lower right part: low fiber packing density*

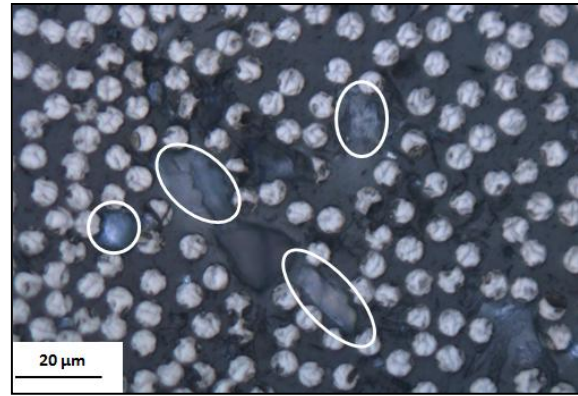Fig. 4-2 c) Sample C0: Misaligned fiber
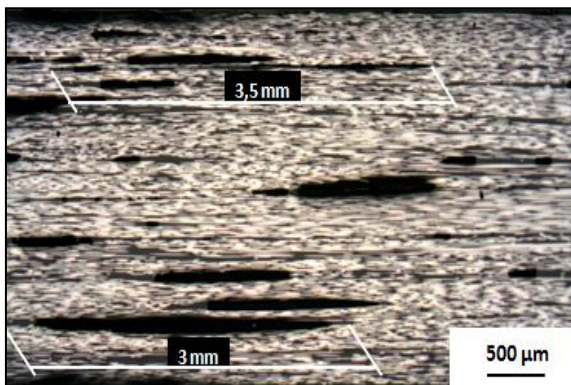

Fig. 4-3 c) Tube sample: Talc inclusion

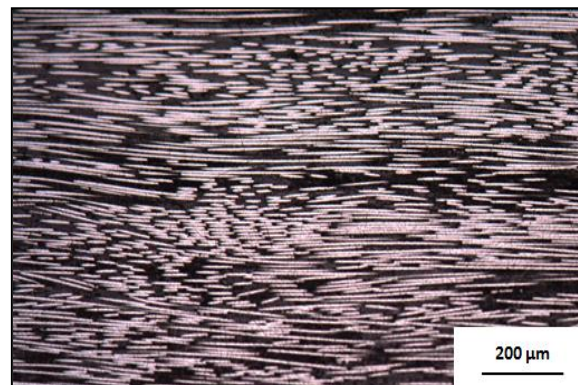Fig. 4-2 d) Sample C0: Elongation of voids parallel to the fiber orientation

Fig. 4-3 d) Tube sample: Fiber waviness

4.1.2 Scanning Electron Microscopy (SEM) – Fractography

<u>Laminates</u>

Fractography of the C0 and C3 0° bending samples perpendicular to the fiber direction revealed the different appearance of the tension and compression part within one sample. Specimen C3-4P-0-01 (fig. 4-4) illustrates these two areas separated by the neutral axis (fig. 4-5) which is located 50µm below the middle of the specimen. The fracture surface on the compression side appears rather flat showing some terraces due to kinkband formations. These steps are rather small being proof of the high modulus epoxy matrix. Furthermore cracks with different shape and size are observed due to ply splitting or matrix cracking as secondary failure.

Fig. 4-4: Sample C3-4P-0-01 after four point bending showing the fragment investigated with SEM

Sample C0-3P-0-05 revealed a huge area where fiber matrix debonding occurred between each fiber layer (fig. 4-6). The tension side of the test specimens always appears fibrous or brittle. Figure 4-7 shows sample C3-4P-0-01 at higher magnification highlighting the good bond between fibers and

matrix as there are no pulled out (broom like) fibers visible. Going more into detail (fig. 4-8) "Directly Attributable Fiber Failures" (DAFF's) are visible meaning that the local fracture sequence of the fibers can be identified. In this case fiber "1" broke first. The radial lines point to the bottom of the fiber, the initial spot where fracture of this fiber started. Fiber "2" began to fail at the point of smallest distance between fiber "1" and "2" and so on. This behavior can be found across the whole fracture surface exposed to tension.
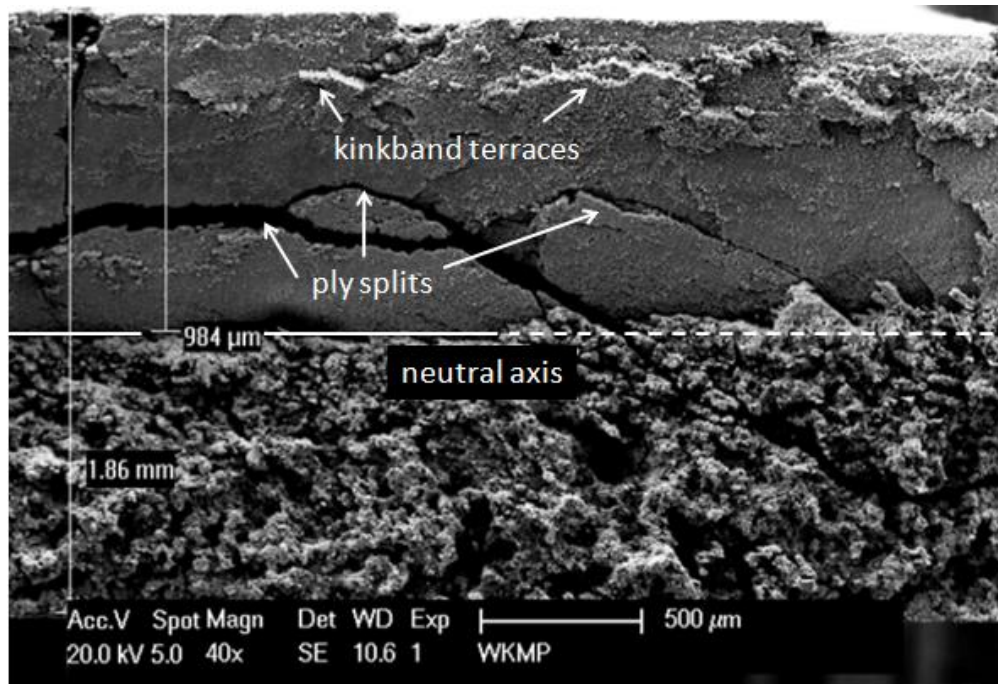

Fig 4-5: Fibrous tension (bottom) and flat compression (top) side of sample C3-4P-0-01 showing ply splitting and kinkband formations
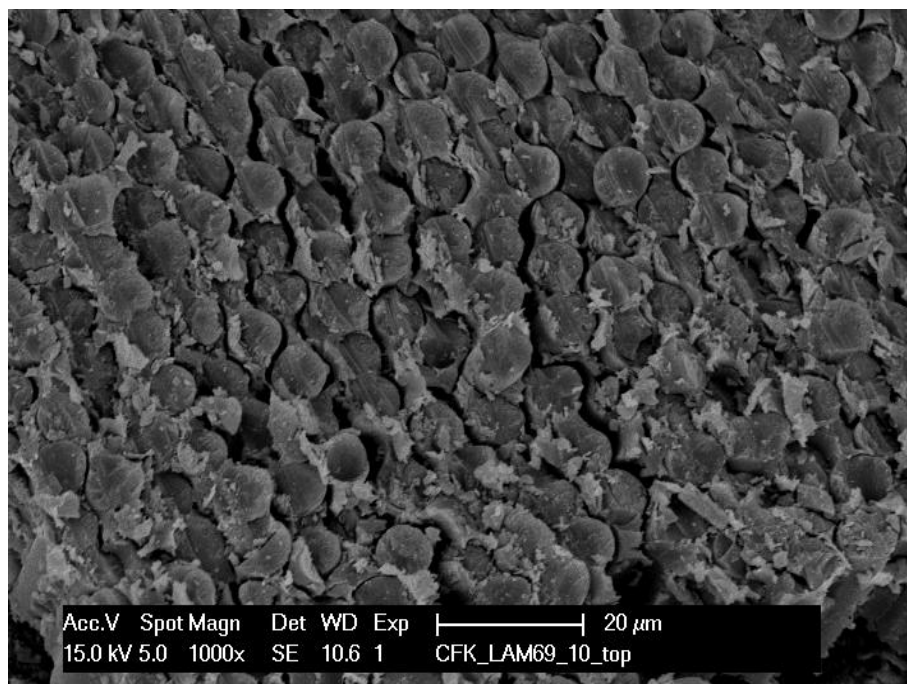

Fig. 4-6: Compression side of sample C0-3P-0-05 showing fiber-matrix debonding
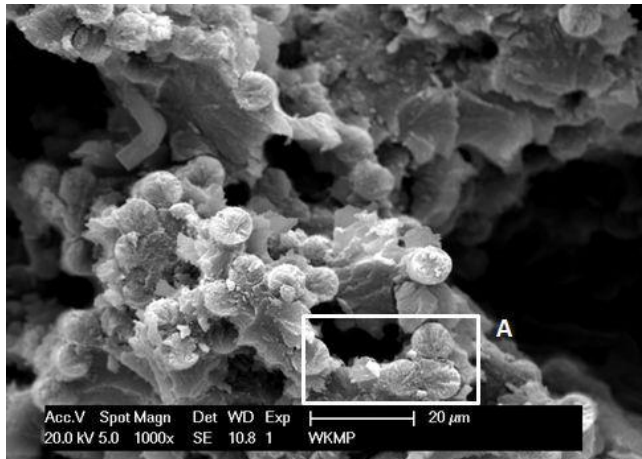
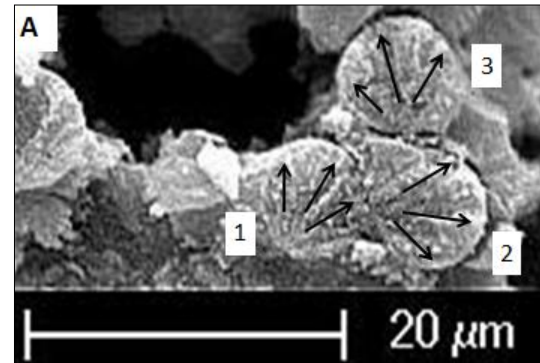Fig. 4-7: Sample C3-4P-0-01, detailed view of the
tension side

Fig. 4-8: Sample C3-4P-0-01 Detail A,
directly attributed fiber failures (DAFF's)
showing the fiber fracture sequence (1-2-3)

Bending also leads to shear deformation and thus to abrasion between the compression and tension side of a bending sample. Accordingly matrix debris can be found alongside the delaminated areas nearby the neutral axis (fig. 4-9).
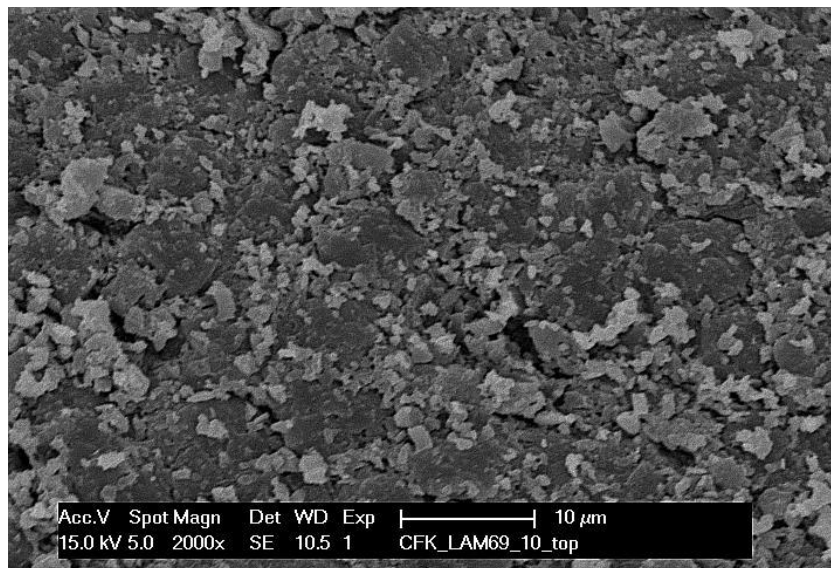

Fig. 4-9: Surface debris on sample C0-3P-0-05

Sample C0-4P-0-12 points out that this shear loading produced delamination leaving a fragment of approximately 30mm in length (fig. 4-10). Examination of the delaminated fracture surface showed cusps (or hackles) of different size and shape (fig. 4-11 a). These fractographic features indicate a relative movement of the fracture surfaces. Typical angle evaluated for this type of laminates was between 75° and 80°. The shape of the cusps can be related to the amount of resin between the fibers. In areas of high resin quantities fewer but larger cusps can be observed, whilst regions of lower resin show a higher amount but smaller cusps (fig. 4-11 a). When cusps are formed on one side of the delaminated fragment the counterpart contains scallops (fig. 4-11 b).
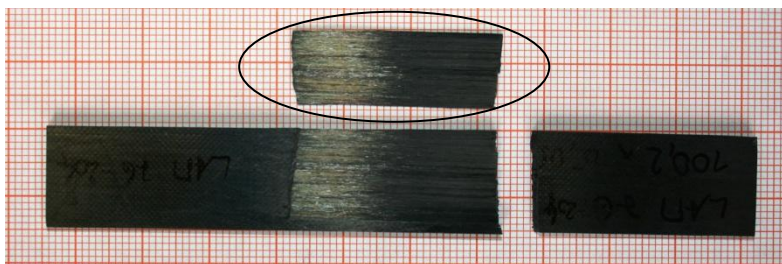
Fig. 4-10: Sample C0-4P-0-12

Highlighted: a 30mm fragment released during testing
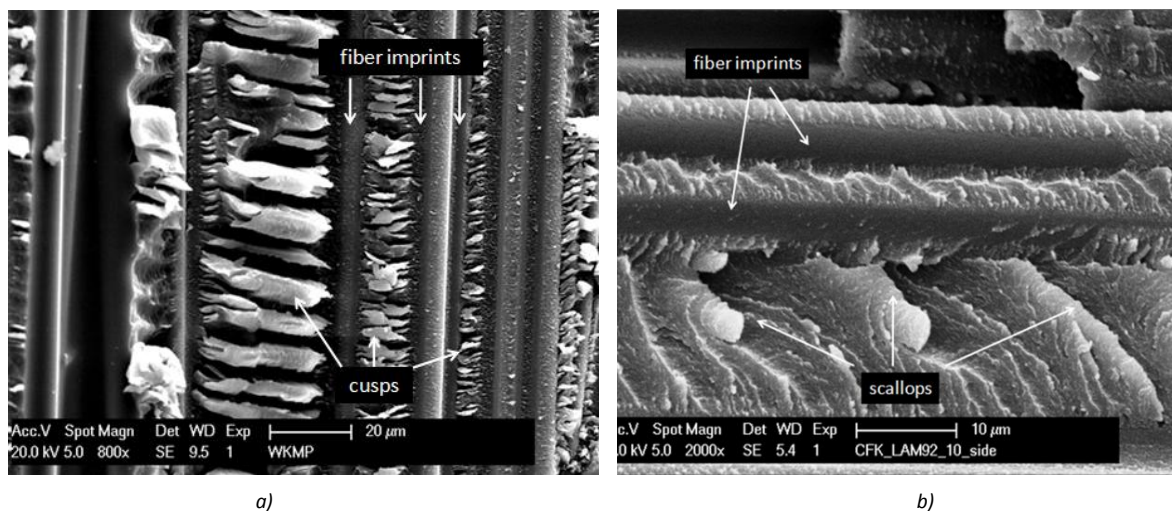
a)
b)

Fig. 4-11 a): Cusps of different size between fiber imprints of sample C0-4P-0-12

b) Counterpart showing scallops

Figures 4-12 a) and b) show voids appearing as smooth regions in the matrix within one specimen, showing that variation in number and size of the voids is not only found among samples of different curing cycles but also within samples manufactured with the same curing cycle.
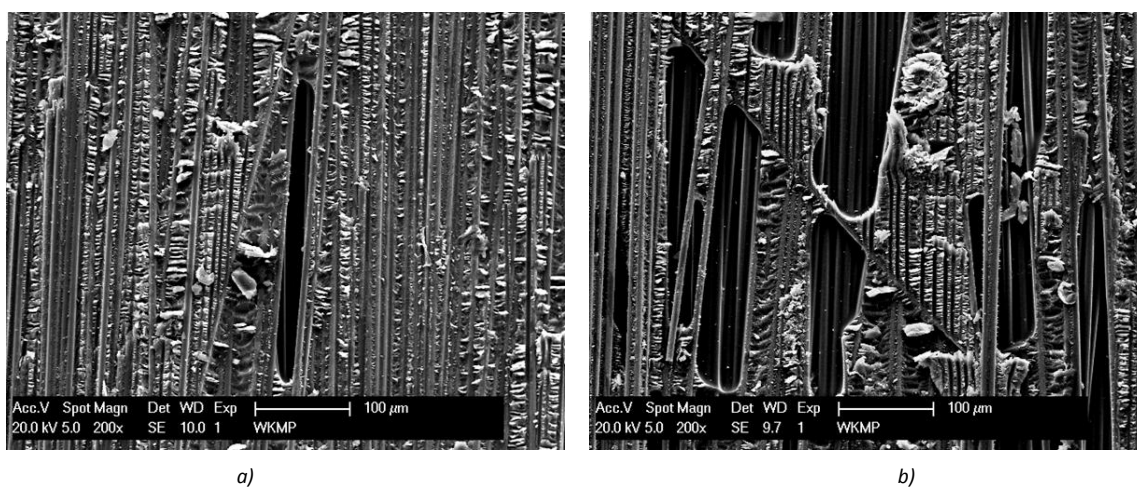
a)
b)

Fig. 4-12 a) Single void in sample C0-4P-0-12

b) Same sample showing conglomeration of voids crossed by a single fiber

Tubes

Due to the different way of manufacturing and type of loading, images of the tubes show different fractographic behavior compared to the laminates. First of all fiber bundles can still be recognized after failure (fig. 4-13 a). The smooth surface of the fibers with just a few matrix debris attached to them are evidence of the weaker bonding between the two parts (fig. 4-13 b). The pulled out fibers prove the same (fig. 4-13 c). Figure 4-13 d) as well shows a nearly bare fiber and furthermore ribbons and scallops can be identified. Huge resin fragments can be found due to the lower material parameters of the L20 resin compared to the HexPly® 8552 (fig. 4-13 e).
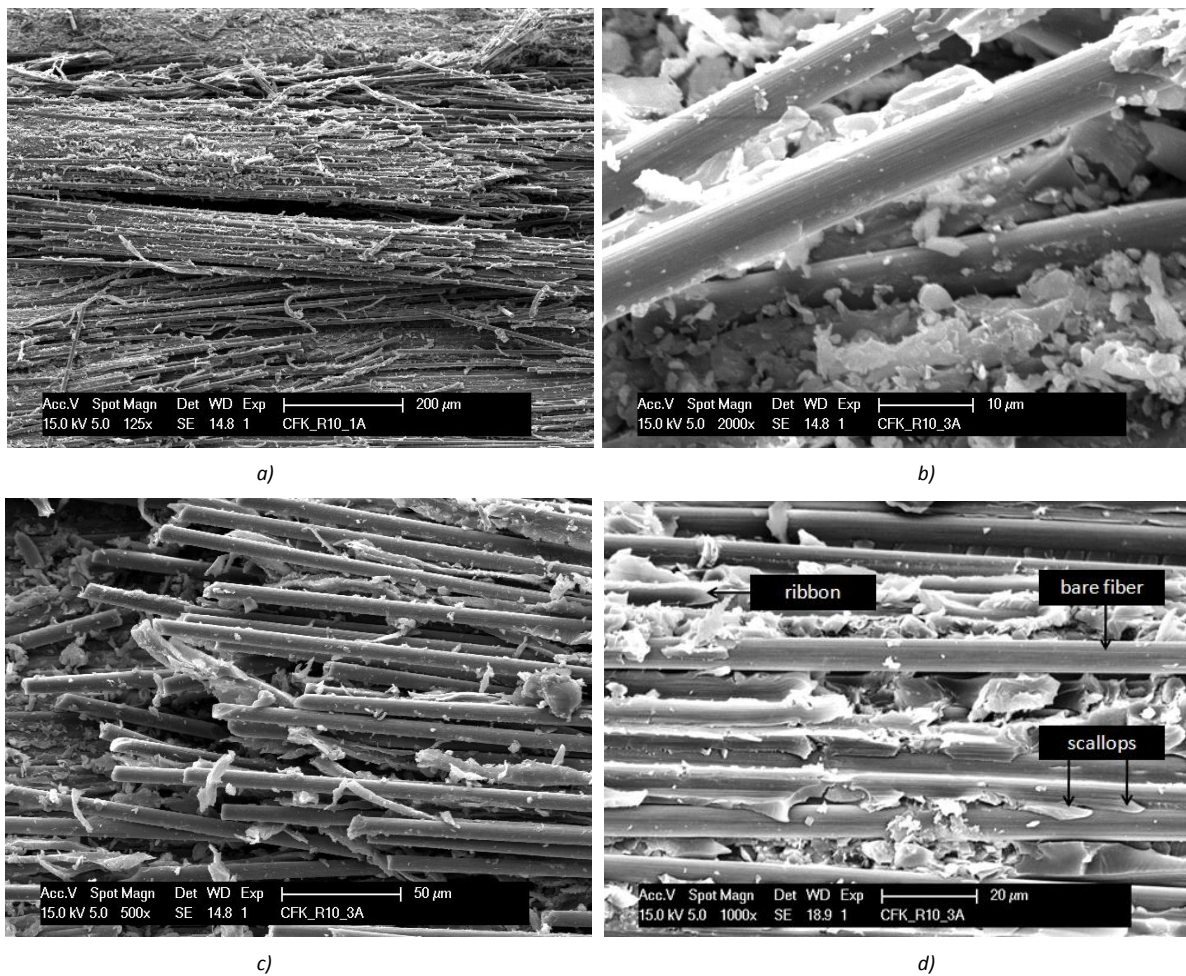

a)

b)

c)

d)

Fig. 4-13: Fractographic images of pultruded tubes showing:

a) Fiber bundles   b) Smooth fiber surface

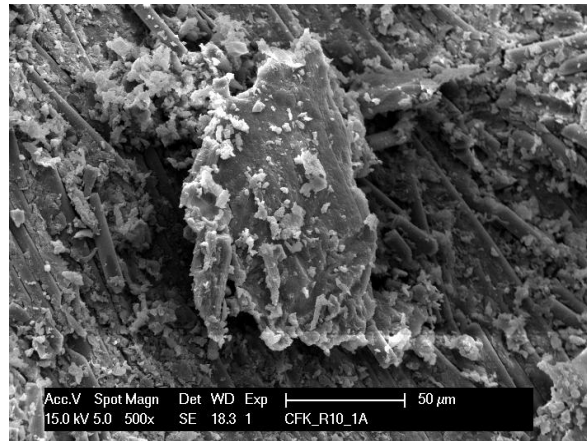c) Pulled out fibers   d) Scallops, a ribbon and a bare fiber

Fig. 4-13 e): Fractographic image of pultruded tubes showing a pulled out resin fragment

4.1.3 Computed Tomography (CT)

<u>Laminates</u>

The porosity volume fraction in the laminates is given in table 4-5, calculated from computed tomography. Figures 4-14 a) and 4-15 a) illustrate a 2D slice of the CT volume with recognized voids (blue areas). The 3D-segmentation of the porosities in figure 4-14 b) and 4-15 b) clearly illustrates the linear (channel-like) arrangement of the voids alongside the fibers. This fact was also illustrated in figures 4-2 d) and 4-12 a) and b). The large scatter of the values is explained by the voxel size of $(9,5\mu m)^3$ used for investigation whereby voids smaller than ~20µm in diameter are not recognized.

Laminate	Volumetric fraction of porosities [%]
C0	$2,7 \pm 1$
C3	$1,1 \pm 1$

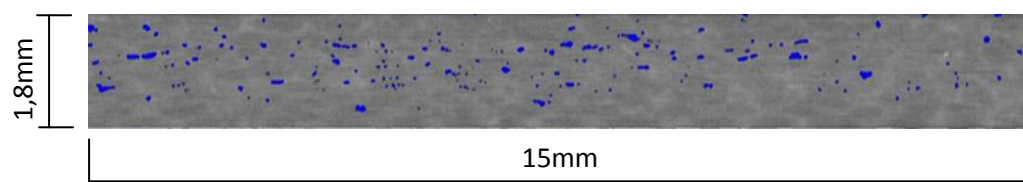*Table 4-5: Laminates and their volumetric fraction of porosities*

Fig. 4-14 a) 2D image of the CT analysis of laminate C0
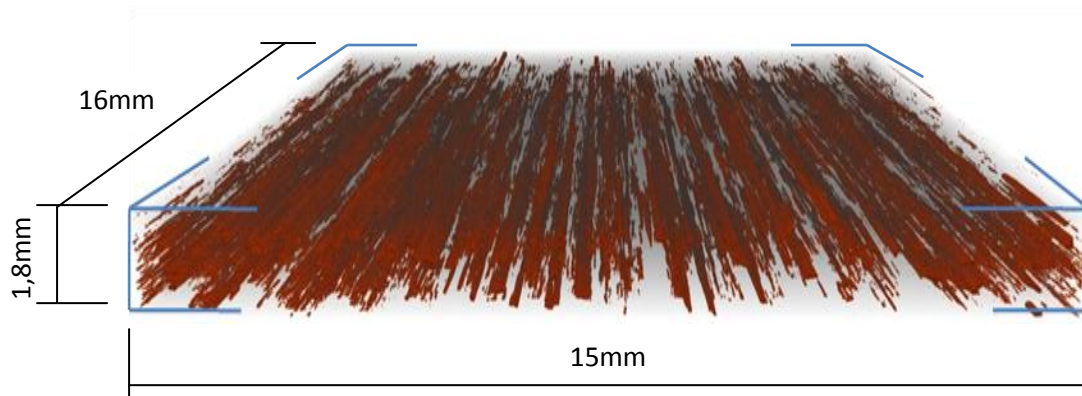
Fig. 4-14 b) 3D reconstruction of the CT analysis of laminate C0
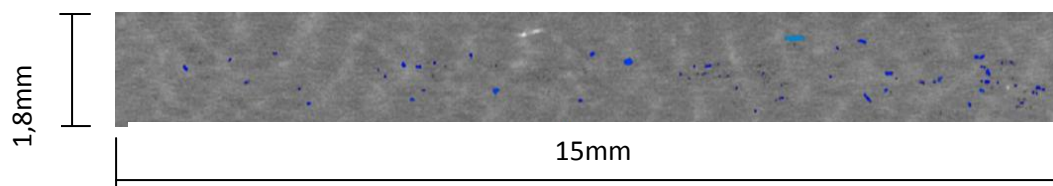
Fig. 4-15 a) 2D image of the CT analysis of laminate C3
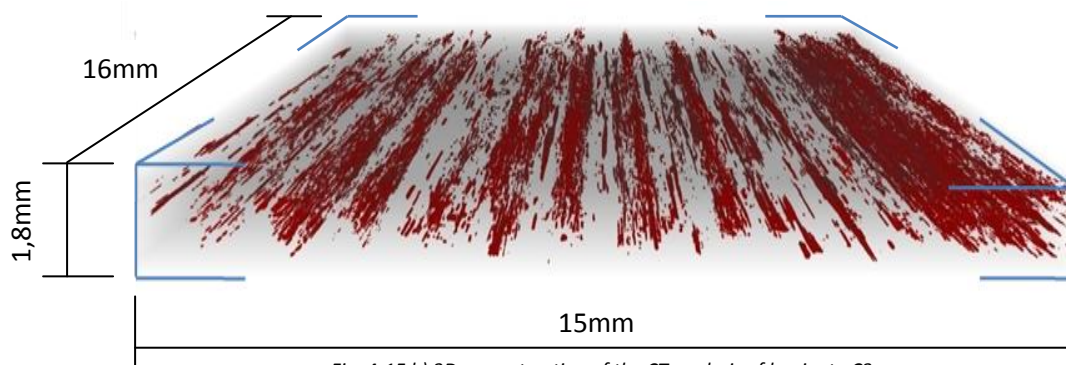
Fig. 4-15 b) 3D reconstruction of the CT analysis of laminate C3

Figure 4-16 a) shows top, side and bottom view of a four point bending sample (C3-4P-0-05) loaded until failure and figure 4-16 b) the CT scan of the sample. Main damage occurred on the tension side due to breaking of the fibers and delamination due to shear stresses. Furthermore two cracks parallel to the fiber orientation (A,B) are visible in the CT scan but only crack B can be clearly identified at macroscopic scale. A possible reason for crack A initiation is an approximately 2mm long void found within this crack. The void starts at 9,5mm (slice 1, fig. 4-16 a and c). At 10,3mm the crack switches from one side of the pore to the other (slice 2, fig. 4-16 a and c) and at 11,5mm it switches back again at the end of the pore (slice 3, fig. 4-16 a and c).
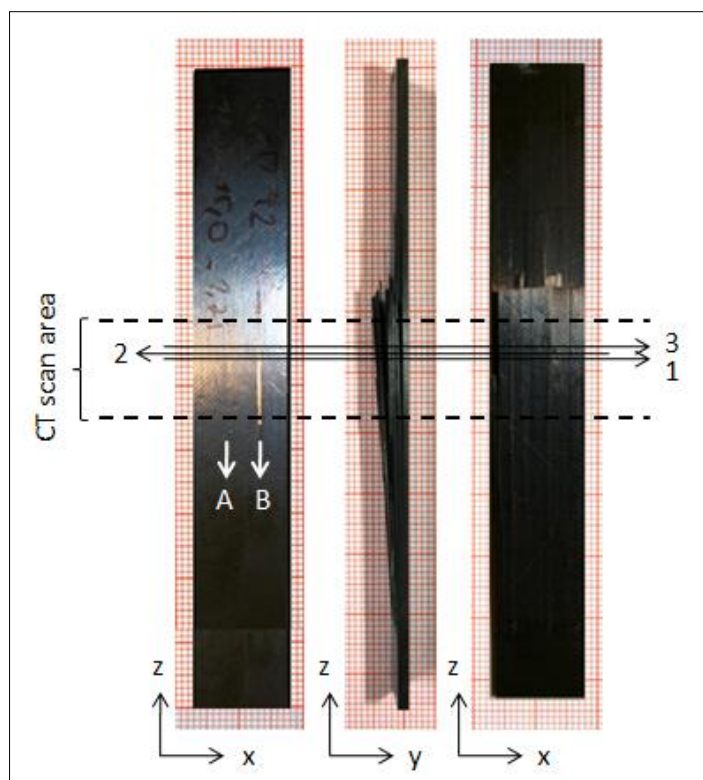
Fig. 4-16 a): Macroscopic view of four point bending sample C3-4P-0-05 showing the rupture of the fibers on the tension side and a small fracture on the compression side (crack B). Numbers "1", "2" and "3" mark the position of the CT scans of figure 5-15 c).
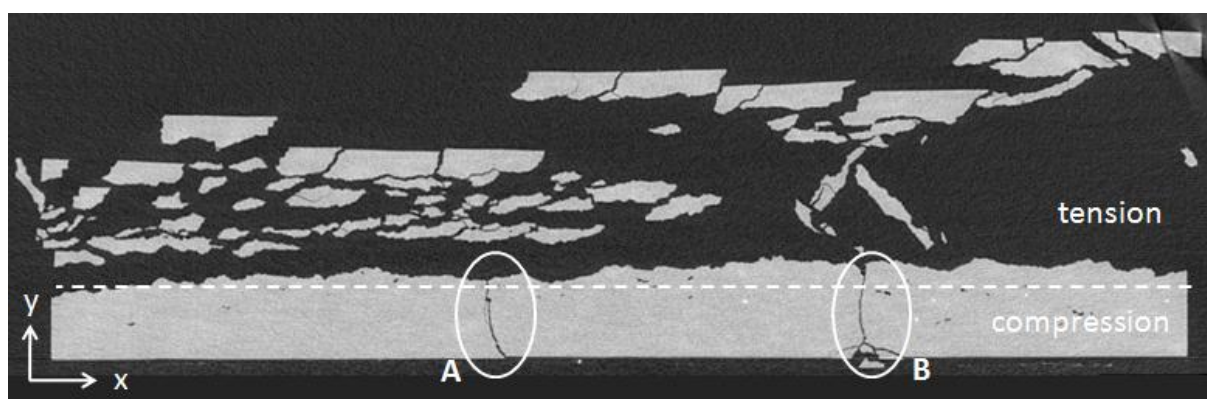
Fig. 4-16 b): CT scan of four point bending sample C3-4P-0-05 at position "2"

Highlighted: tension and compression side separated by the neutral axis (dashed line) and cracks "A" and "B"
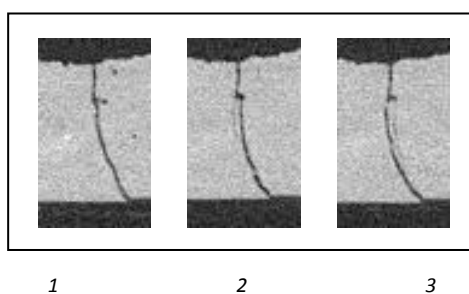
Fig. 4-16 c): Propagation of crack "A" alongside the z-axis of sample C3-4P-0-05.
Position 1: 9,5mm, position 2: 10,3mm, position 3: 11,5mm of the CT scan

Tubes

The torsion tests of samples P10-04 and 05 were interrupted but did not reveal any indication of failure. Samples P10-01, 02 and 06 failed at the fixing points. Therefore only CT scan of sample P10-03 can be taken into account. Figure 4-17 a) shows an image of this sample before the testing and figures 4-17 b) and c) the detailed view of the area where failure occurred. Black regions count for fibers and white regions for matrix. A variation of wall thickness can be seen having its minimum at the bottom. The crack is located where material thickness is the smallest. Furthermore it can be seen that the crack did not grow from one resin rich area to another but at the boarders between them. Further resin rich areas can be seen at the left side of the sample but only at the outer boundaries.


Fig. 4-17 b): Detail "A" before testing
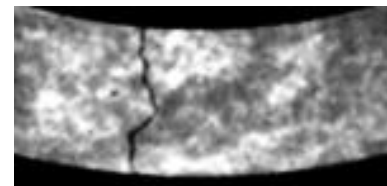
Fig. 4-17 c): Detail "A" after testing showing the crack

Fig. 4-17 a): CT scan of sample P10-03 before torsion test showing slight variations in material thickness. Highlighted: Detail "A" where failure occurred.

4.2 Mechanical Analysis

4.2.1 Three Point Bending

C0 Laminates

Figure 4-18 shows the stress over strain curves of samples C0-3P-0-01 to C0-3P-90-10 and table 4-6 the sample dimensions, Young's modulus, the failure stress, the failure strain and the average values including the standard deviation of the 0° samples of the curing cycle C0. Table 4-7 provides the same data of the 90° samples. Sample C0-3P-0-06 exhibited a Teflon foil as a kind of artificial delamination and therefore collapsed much earlier at 773MPa. For this sample the uncertainty of the Young's modulus, the failure stress and the failure strain is given by the systematic error explained in chapter 3.3.1. Figure 4-19 represents the graphic account of the uncertainty of the Young's modulus- and

figure 4-20 of the failure stress calculation. The red spots mark the calculated value and the vertical lines indicate the lower and the upper limit of the value (±7% regarding the Young' modulus and ±1,3% regarding the failure stress, as given in chapter 3.3.1) due to the systematic error of the calculation. Thus the exact value can be located anywhere between these limits. The solid horizontal line indicates the mean value ($\bar{x}$) and the two dashed lines the mean value plus/minus the standard deviation (s) of the Young's modulus and the failure stress respectively, according to the values given in table 4-6. As already mentioned the only outlier is sample C0-3P-0-06 which collapsed due to artificial delamination and is discussed in detail in chapter 5-3. All samples were tested until failure occurred.
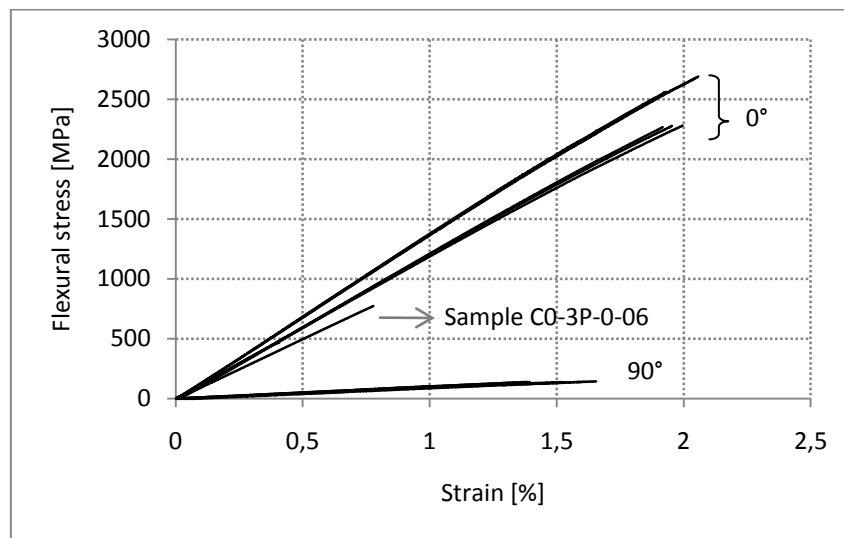
Fig. 4-18: Stress-strain diagram of samples C0-3P-0-01 to 06 tested in 0° fiber direction and samples C0-3P-90-07 to 10 tested in 90° fiber direction. Sample C0-3P-0-06 collapsed much earlier due to artificial delamination and is discussed in detail in chapter 5.3.

Sample code	Sample dimensions [mm]	Young's Modulus [GPa]	Mean Young's Modulus [GPa]	Failure Stress [MPa]	Mean Failure Stress [MPa]	Failure Strain [%]	Mean Failure Strain [%]
C0-3P-0-01	15,18x1,90	118		2281		2,00	
C0-3P-0-02	14,94x1,90	123		2267		1,92	
C0-3P-0-03	14,27x1,92	120	126 ± 8	2278	2438 ± 223	1,95	2,0 ± 0,1
C0-3P-0-04	15,48x1,66	134		2690		2,06	
C0-3P-0-05	15,40x1,65	136		2676		2,05	
C0-3P-0-06	14,15x1,93	99*	99 ± 7,1	773*	773 ± 10,1	0,78	0,78 ± 0,01

Table 4-6: Mechanical properties of samples cured with curing cycle C0 tested in 0° fiber direction. Sample C0-3P-0-06 collapsed much earlier due to artificial delamination and is discussed in detail in chapter 5.3. Uncertainty of the values for this sample is given by the systematic error of the measurement according to chapter 3.3.1.

Fig. 4-19: Mean value (solid line), standard deviation (dashed lines), measured Young's modulus (red dots), lower and upper limits due to the failure calculation of three point bending samples C0-3P-0-01 to 06 tested parallel to the fiber orientation. Sample C0-3P-0-06 shows a lower Young's modulus and is discussed in detail in chapter 5.3.

Fig. 4-20: Mean value (solid line), standard deviation (dashed lines), measured failure stress (red dots), lower and upper limits due to the failure calculation of three point bending samples C0-3P-0-01 to 06 tested parallel to the fiber orientation. Sample C0-3P-0-06 shows a lower failure stress and is discussed in detail in chapter 5.3.

Sample code	Sample dimensions [mm]	Young's Modulus [GPa]	Mean Young's Modulus [GPa]	Failure Stress [MPa]	Mean Failure Stress [MPa]	Failure Strain [%]	Mean Failure Strain [%]
C0-3P-90-07	15,37x1,70	9,4		144		1,66	
C0-3P-90-08	15,55x1,68	10,0	9,5 ± 1	140	140 ± 3	1,39	1,5 ± 0,1
C0-3P-90-09	15,35x1,70	8,8		138		1,52	
C0-3P-90-10	14,88x1,69	9,9		138		1,38	

Table 4-7: Mechanical properties of samples cured with curing cycle C0 tested in 90° fiber direction

C3 Laminates

Figure 4-21 presents the stress-strain diagrams of samples C3-3P-0-01 and 02 exemplarily and table 4-8 comprises the sample dimension, Young's modulus, the failure stress, the failure strain and the average values including the standard deviation of all three 0° samples of curing cycle C3. All samples were tested until failure.
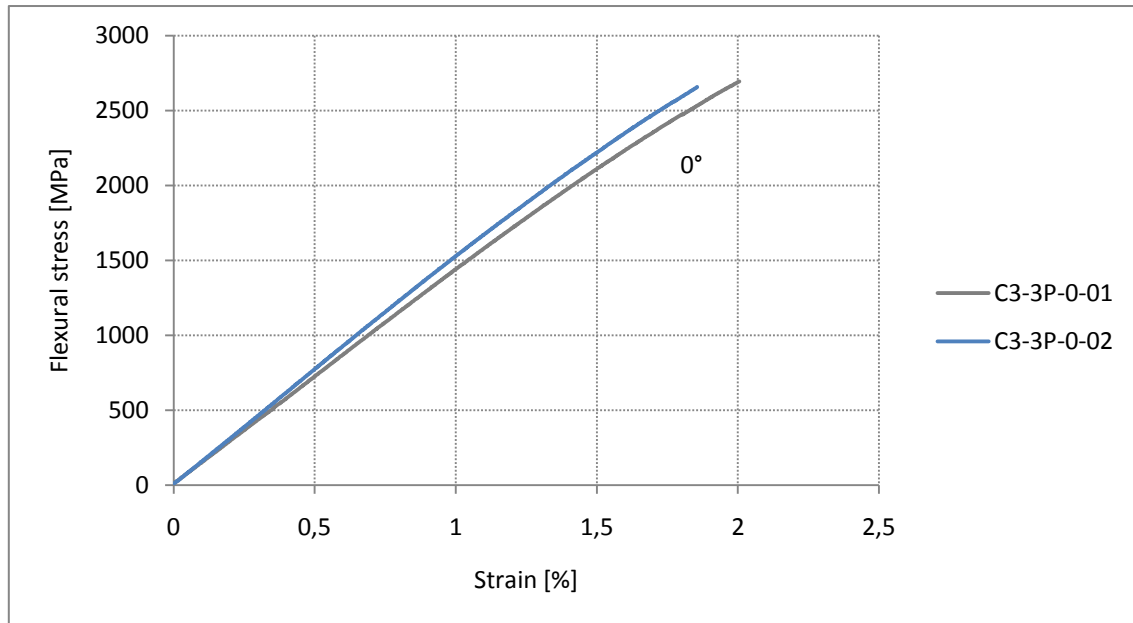
Fig. 4-21: Stress-strain diagram of samples C3-3P-0-01 and 02 tested in 0° fiber direction

Sample code	Sample dimensions [mm]	Young's Modulus [GPa]	Mean Young's Modulus [GPa]	Failure Stress [MPa]	Mean Failure Stress [MPa]	Failure Strain [%]	Mean Failure Strain [%]
C3-3P-0-01	15,40x1,88	142		2694		2,00	
C3-3P-0-02	15,29x1,78	152	149 ± 6	2551	2650 ± 86	1,86	1,9 ± 0,1
C3-3P-0-03	15,04x1,75	154		2706		1,85	

Table 4-8: Mechanical properties of samples cured with curing cycle C3 tested in 0° fiber direction

Figure 4-22 represents the graphic account of the uncertainty of the Young's modulus- and figure 4-23 of the failure stress calculation. The red spots mark the calculated value and the vertical lines indicate the lower and the upper limit of the value (±7% regarding the Young' modulus and ±1,3% regarding the failure stress, as given in chapter 3.3.1) due to the systematic error of the calculation. Thus the exact value can be located anywhere between these limits. The solid horizontal line indicates the mean value ($\bar{x}$) and the two dashed lines the mean value plus/minus the standard deviation (s) of the Young's modulus and the failure stress respectively, according to the values given

in table 4-8. Taking the systematic error into account, all values are located within the limits given by the mean value plus/minus the standard deviation.
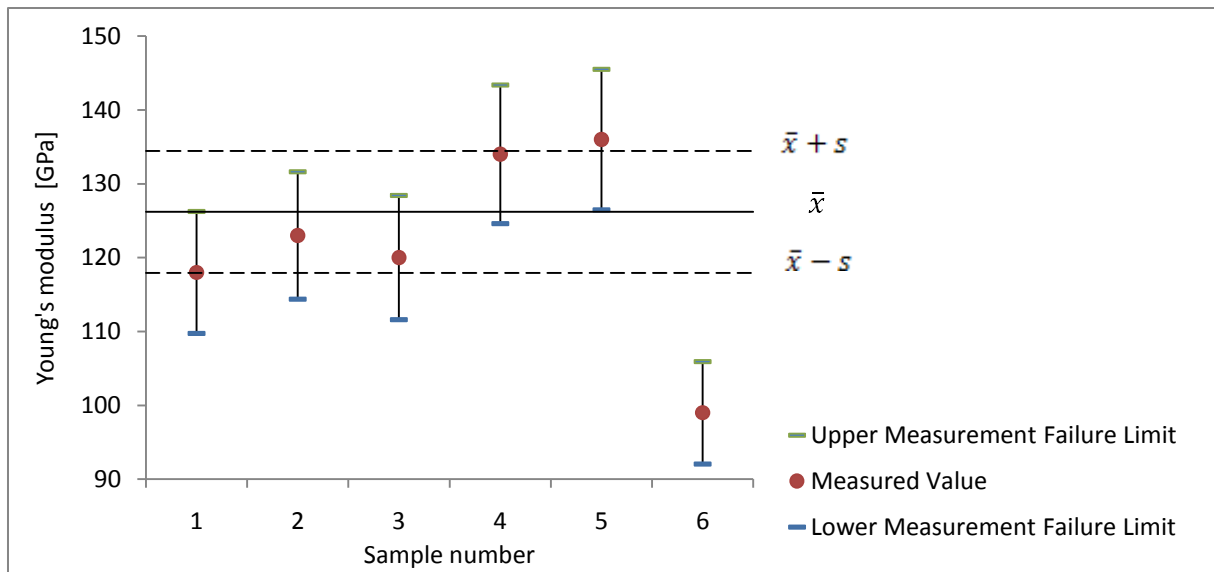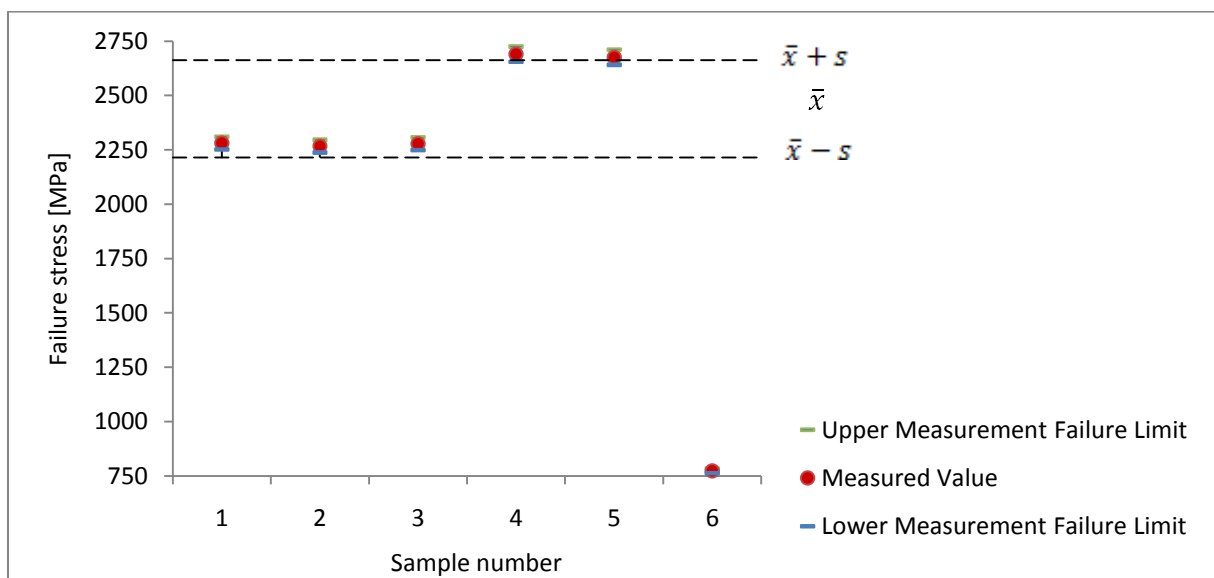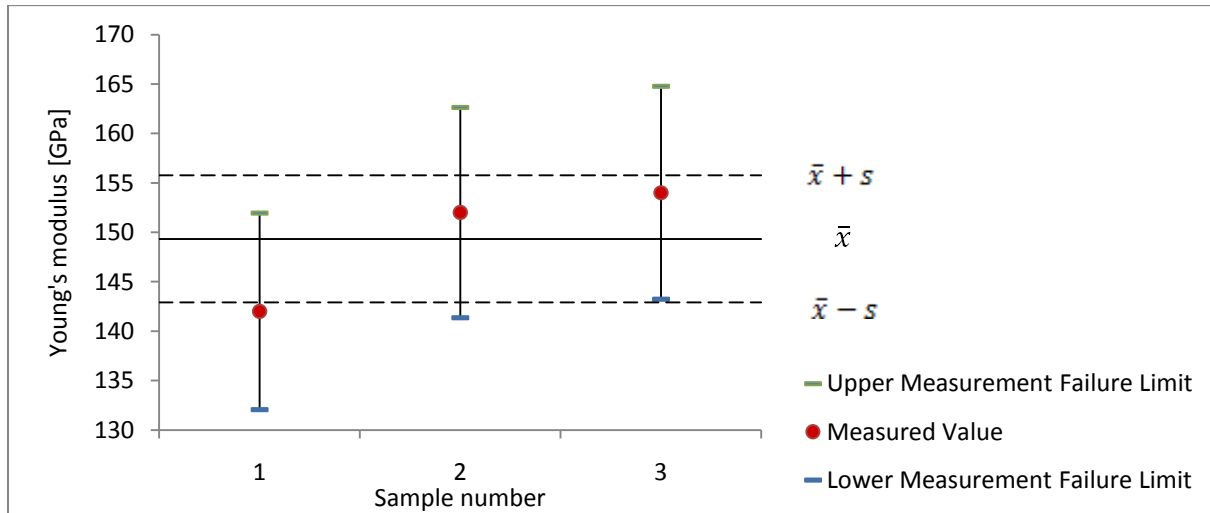

Fig. 4-22: Mean value (solid line), standard deviation (dashed lines), measured Young's modulus (red dots), lower and upper limits due to the failure calculation of four point bending samples C3-3P-0-01 to 03 tested parallel to the fiber orientation
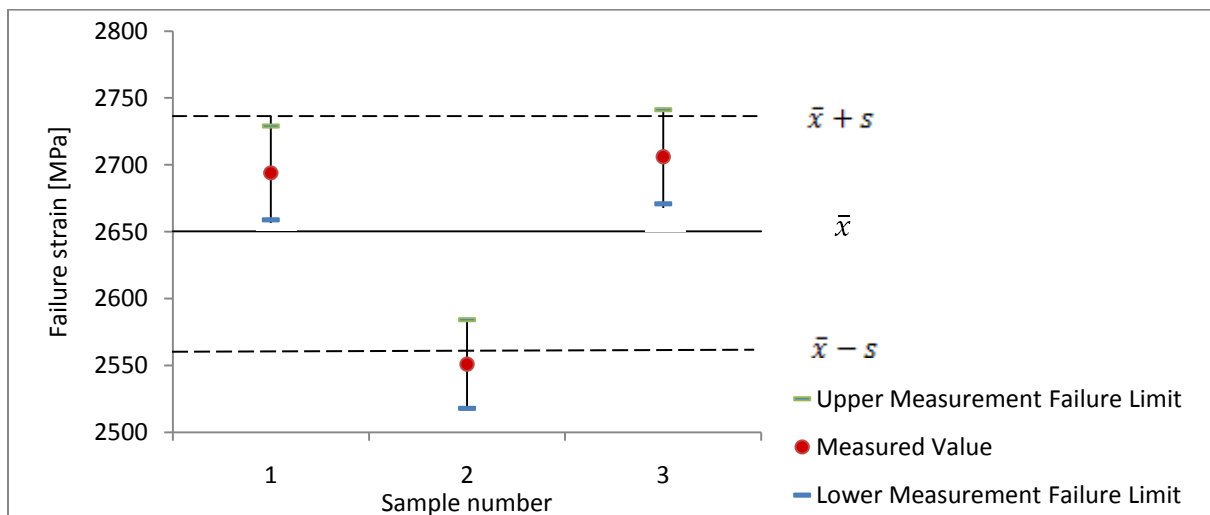
Fig. 4-23: Mean value (solid line), standard deviation (dashed lines), measured failure stress (red dots), lower and upper limits due to the failure calculation of four point bending samples C3-3P-0-01 to 03 tested parallel to the fiber orientation

4.2.2 Four Point Bending

C0 Laminates

Samples C0-4P-0-01 to C0-4P-0-08 were stressed with three hysteresis cycles (reversal points at 300, 600 and 850N). Samples C0-4P-0-15 and 16 were loaded with the same hysteresis cycles not once but 5 times. This was done to make sure that AE signals did not arise from friction between the support and the sample. Figure 4-24 shows exemplarily the stress-strain curves of samples C0-4P-0-05 and 08 and figure 4-25 the diagrams of samples C0-4P-0-15 and 16. First failure of specimen 04 and 06 occurred before reaching the third reversal point at 850N though testing was proceeded until

samples collapsed totally. Samples C0-4P-0-09 to C0-4P-0-14 were stressed with nine hysteresis cycles (reversal points at 300, 600, 700, 750, 800, 850, 900, 950 and 1000N). Figure 4-26 depicts the exemplarily the stress-strain diagram of specimen 09 and 12. Sample 11 was interrupted after the sixth hysteresis cycle and samples 10, 13 and 14 after the eighth hysteresis cycle. Specimen 09, 10 and 11 were used for CT investigation and samples 13 and 14 for DMA analysis. Table 4-9 contains the sample dimension, Young's modulus, the failure stress, the failure strain and the average values including the standard deviation of all C0 samples tested.

Fig. 4-24: Stress-strain diagrams of samples C0-4P-0-05 and C0-4P-0-08 tested in 0° fiber orientation.

Reversal points of hysteresis cycles at 300, 600 and 850N. Samples 04 and, 06 collapsed before reaching the third reversal point.

Fig. 4-25: Samples C0-4P-0-15 and 16 tested in 0° fiber direction in combination with acoustic emission measurements

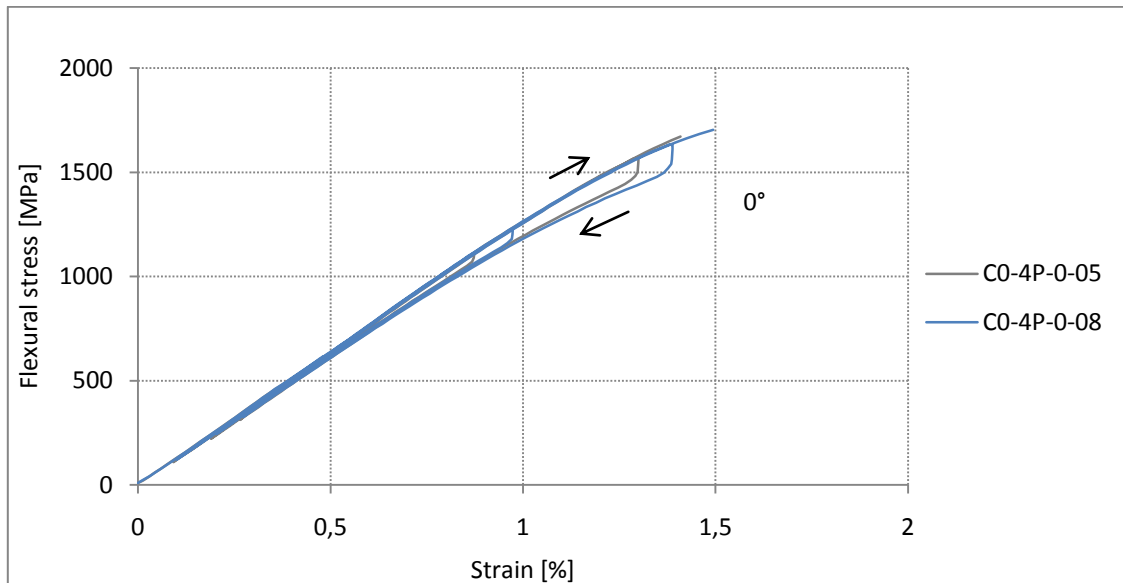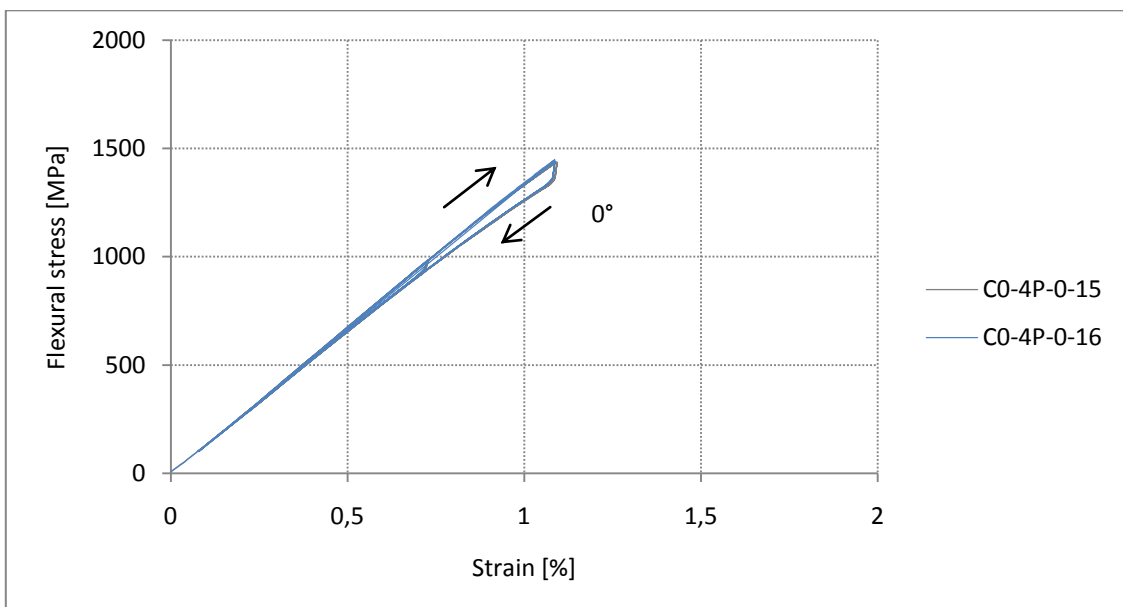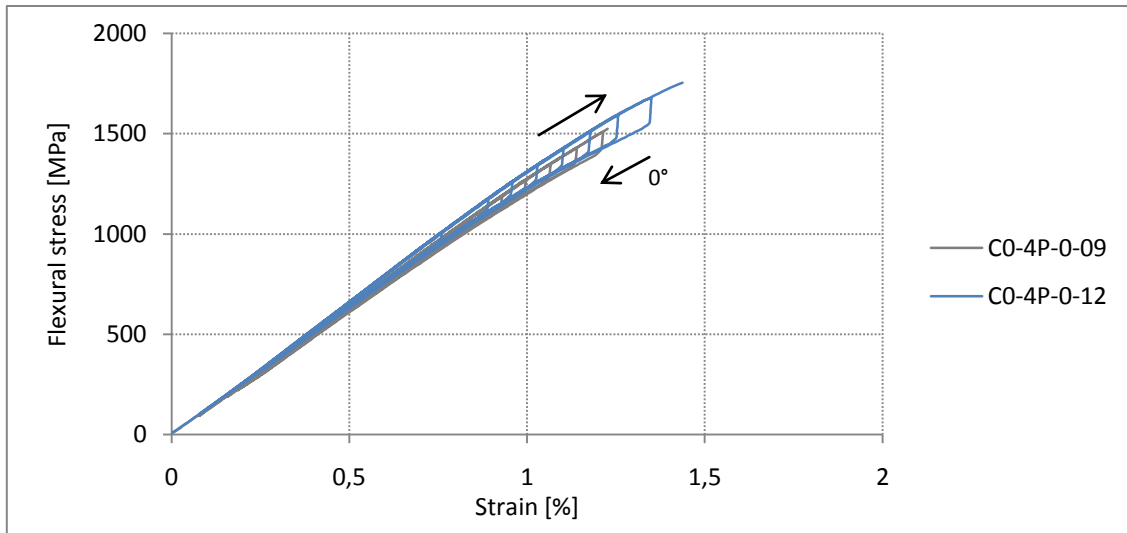*Reversal points of hysteresis cycles at 300, 600 and 850N*

Fig. 4-26: Stress-strain diagrams of samples C0-4P-0-09 and C0-4P-0-12 tested in 0° fiber orientation.

Reversal points of the hysteresis cycles at 300, 600, 700, 750, 800, 850, 900, 950 and 1000N.

Sample code	Sample dimensions [mm]	Young's Modulus [GPa]	Mean Young's Modulus [GPa]	Failure Stress [MPa]	Mean Failure Stress [MPa]	Failure Strain [%]	Mean Failure Strain [%]
C0-4P-0-01	15,51x1,74	119		1592		1,40	
C0-4P-0-02	15,23x1,72	128		1634		1,40	
C0-4P-0-03	15,16x1,74	126		(1496)		(0,70)	
C0-4P-0-04	15,11x1,66	117		1511*		1,58	
C0-4P-0-05	14,93x1,71	127		1671		1,44	
C0-4P-0-06	15,04x1,66	127		1643		1,45	
C0-4P-0-07	15,08x1,66	114*		(1392)		(1,41)	
C0-4P-0-08	15,07x1,62	127	126 ± 5	1704	1644 ± 79	1,49	1,5 ± 0,1
C0-4P-0-09	15,05x1,84	124		(1525)		(1,26)	
C0-4P-0-10	15,00x1,80	131		(1583)		(1,03)	
C0-4P-0-11	15,05x1,81	130		(1475)		(1,07)	
C0-4P-0-12	15,05x1,79	129		1755*		1,44	
C0-4P-0-13	15,05x1,80	128		(1645)		(1,37)	
C0-4P-0-14	15,05x1,80	127		(1655)		(1,24)	
C0-4P-0-15	15,05x1,77	132		(1437)		(1,09)	
C0-4P-0-16	14,85x1,76	132		(1447)		(1,09)	

Table 4-9: Mechanical properties of samples cured with curing cycle C0 tested in 0° fiber orientation. Numbers in brackets refer to interrupted tests due to further investigations. These values have not been considered for calculation of the mean values. Values marked with * are outliers according to fig. 4-27 and 4-28 and discussed in chapter 5.2.

Figure 4-27 represents the graphic account of the uncertainty of the Young's modulus- and figure 4-28 of the failure stress calculation. The red spots mark the calculated value and the vertical lines

indicate the lower and the upper limit of the value (±6% regarding the Young' modulus and ±1,2% regarding the failure stress, as given in chapter 3.3.2) due to the systematic error of the calculation. Thus the exact value can be located anywhere between these limits. The solid horizontal line indicates the mean value ($\bar{x}$) and the two dashed lines the mean value plus/minus the standard deviation (s) of the Young's modulus and the failure stress respectively, according to the values given in table 4-9. The only outlier in case of the Young's modulus is sample C0-4P-0-07 and in case of the failure stress samples C0-4P-0-04 and 12. All three samples are discussed in chapter 5-2.

Fig. 4-27: Mean value (solid line), standard deviation (dashed lines), measured Young's modulus (red dots), lower and upper limits due to the failure calculation of four point bending samples C0-4P-0-01 to 16 tested parallel to the fiber orientation. Sample C0-4P-0-07 does not fit the limits and is discussed in chapter 5.2.
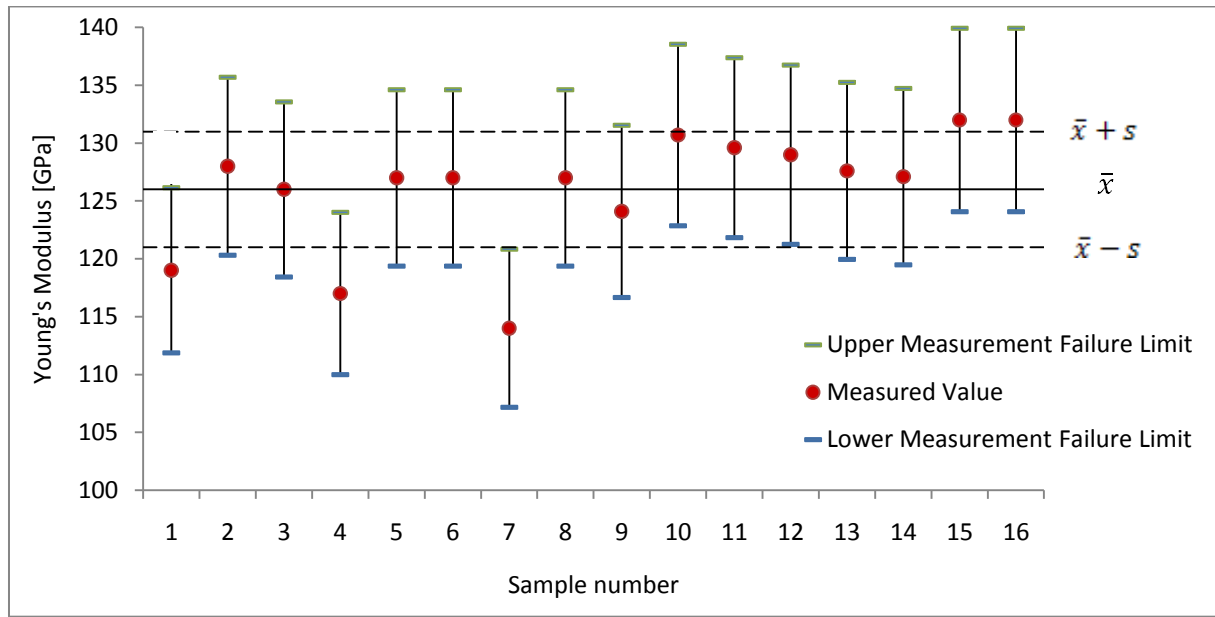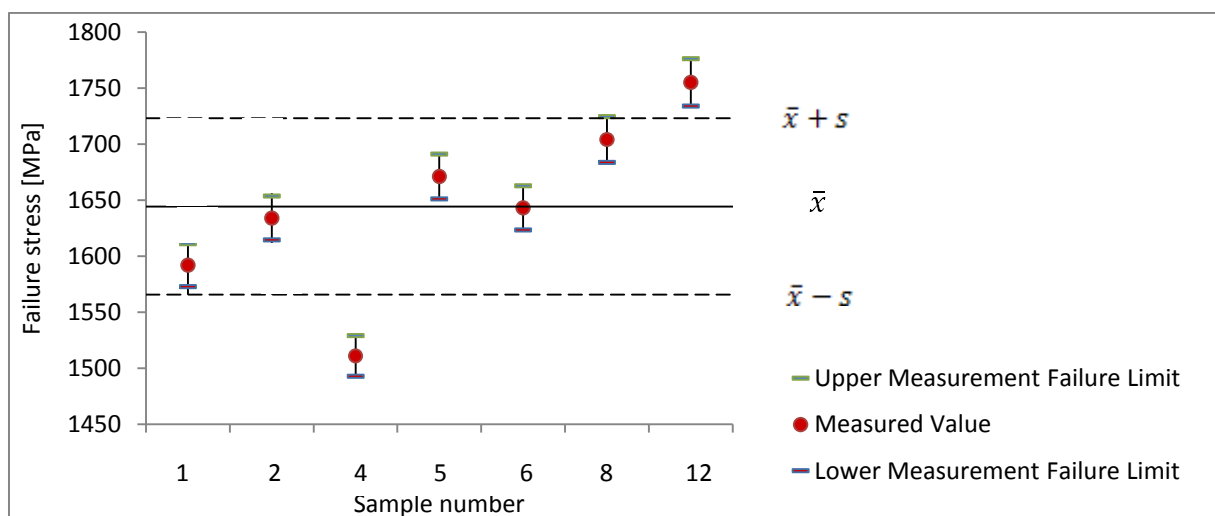

Fig. 4-28: Mean value (solid line), standard deviation (dashed lines), measured failure stress (red dots), lower and upper limits due to the failure calculation of four point bending samples C0-4P-0-01 to 12,.leaving out interrupted tests, loaded parallel to the fiber orientation. Samples C0-4P-0-04 and 12 do not fit the limits and are discussed in chapter 5.2.

C3 Laminates

Samples C3-4P-0-06, 07, 08 and 09 were loaded continuously but only sample 06 until failure. Testing of samples 07, 08 and 09 was interrupted for CT analysis. Samples C3-4P-0-10, 11 and 12 were stressed with three hysteresis cycles (reversal points at 300, 900 and 1200N). Figure 4-29 shows exemplarily the stress-strain curves of samples 11 and 12. Samples C3-4P-0-01 and 05 were stressed with nine hysteresis cycles (reversal points at 300, 600, 700, 750, 800, 850, 900, 950 and 1000N). Figure 4-30 depicts exemplarily the stress- strain diagram of samples C3-4P-0-01 and 05. Figure 4-31 represents the graphic account of the uncertainty of the Young's modulus- and figure 4-32 of the failure stress calculation. The red spots mark the calculated value and the vertical lines indicate the lower and the upper limit of the value ($\pm$6% regarding the Young' modulus and $\pm$1,2% regarding the failure stress, as given in chapter 3.3.2) due to the systematic error of the calculation. Thus the exact value can be located anywhere between these limits. The solid horizontal line indicates the mean value ($\bar{x}$) and the two dashed lines the mean value plus/minus the standard deviation (s) of the Young's modulus and the failure stress respectively, according to the values given in table 4-10. Taking the systematic error into account, all values are located within the limits given by the mean value plus/minus the standard deviation. Figure 4-33 presents the diagrams for samples C3-4P-90-01 and 02, having a fiber orientation of 90°. Table 4-10 contains the sample dimension, Young's modulus, the failure stress, the failure strain and the average values including the standard deviation of all 0° samples of curing cycle C3 and table 4-11 the same values for all 90° samples tested.
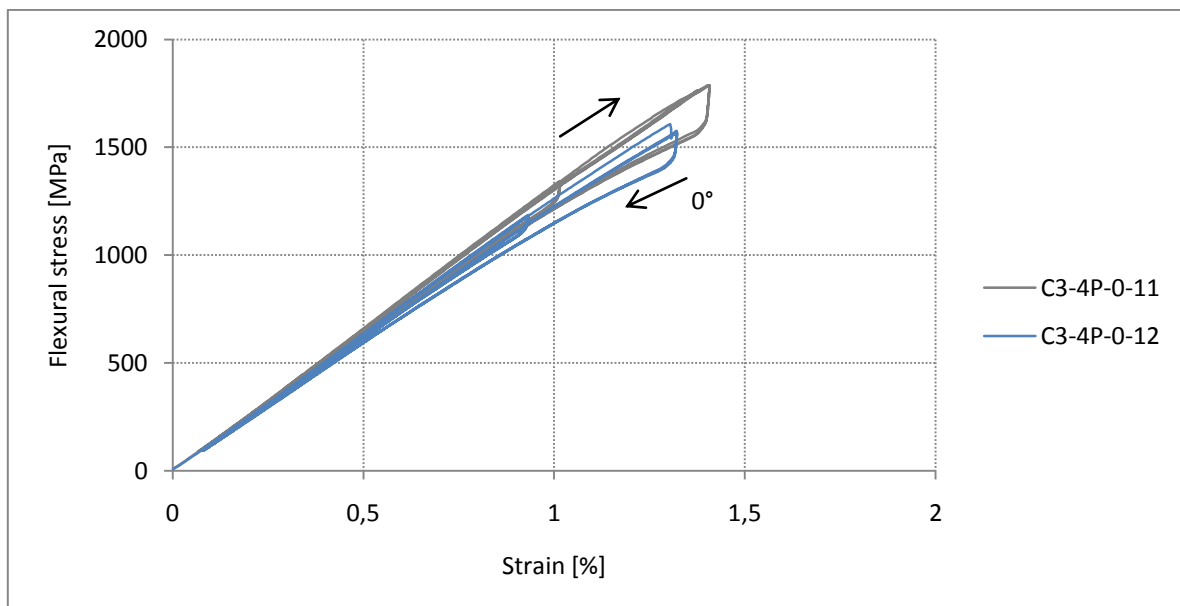

Fig. 4-29: Stress-strain diagrams of samples C3-4P-0-11 and 12 tested in 0° fiber orientation.

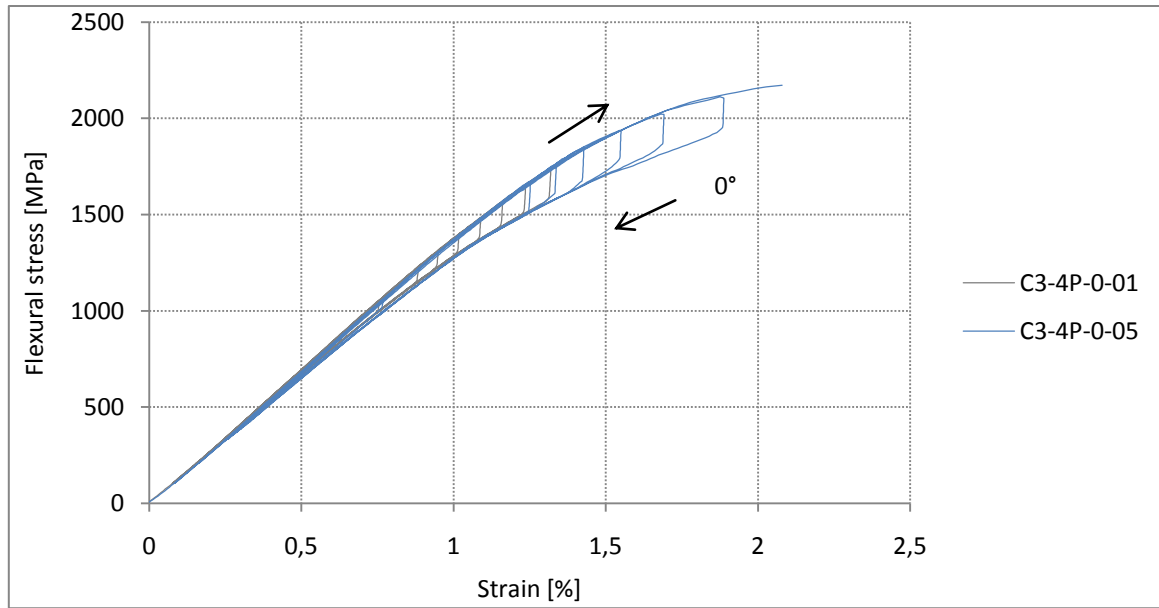*Reversal points of hysteresis cycles at 300, 900 and 1200N.*

Fig. 4-30: Stress-strain diagrams of samples C3-4P-0-01 and 05 tested in 0° fiber orientation. Reversal points of the hysteresis cycles at 300, 600, 700, 750, 800, 850, 900, 950 and 1000N. Nonlinearity of the curves at high strains is discussed in chapter 5-2.

Sample code	Sample dimensions [mm]	Young's Modulus [GPa]	Mean Young's Modulus [GPa]	Failure Stress [MPa]	Mean Failure Stress [MPa]	Failure Strain [%]	Mean Failure Strain [%]
C3-4P-0-01	15,05x1,76	134		1790		1,37	
C3-4P-0-02	15,07x1,75	137		(2039)		(1,65)	
C3-4P-0-03	14,99x1,75	138		(2049)		(1,64)	
C3-4P-0-04	15,05x1,75	136		(2028)		(1,67)	
C3-4P-0-05	15,00x1,75	133		2172		2,08	
C3-4P-0-06	15,03x1,75	135		2136		1,90	
C3-4P-0-07	15,28x1,74	136	133 ± 4	(1276)	1956 ± 186	(0,92)	1,7 ± 0,3
C3-4P-0-08	15,30x1,74	134		(1401)		(1,03)	
C3-4P-0-09	15,21x1,74	135		(1613)		(1,19)	
C3-4P-0-10	15,20x1,90	128		1894		1,50	
C3-4P-0-11	15,10x1,90	128		1788		1,40	
C3-4P-0-12	14,40x1,89	124		(1608)		(1,3)	

Table 4-10: Mechanical properties of samples cured with curing cycle C3 tested in 0° fiber orientation. Numbers in brackets refer to interrupted tests due to further investigations. These values have not been considered for calculating the mean values.

Fig. 4-31: Mean value (solid line), standard deviation (dashed lines), measured Young's modulus (red dots), lower and upper limits due to the failure calculation of four point bending samples C3-4P-0-01 to 12 tested parallel to the fiber orientation
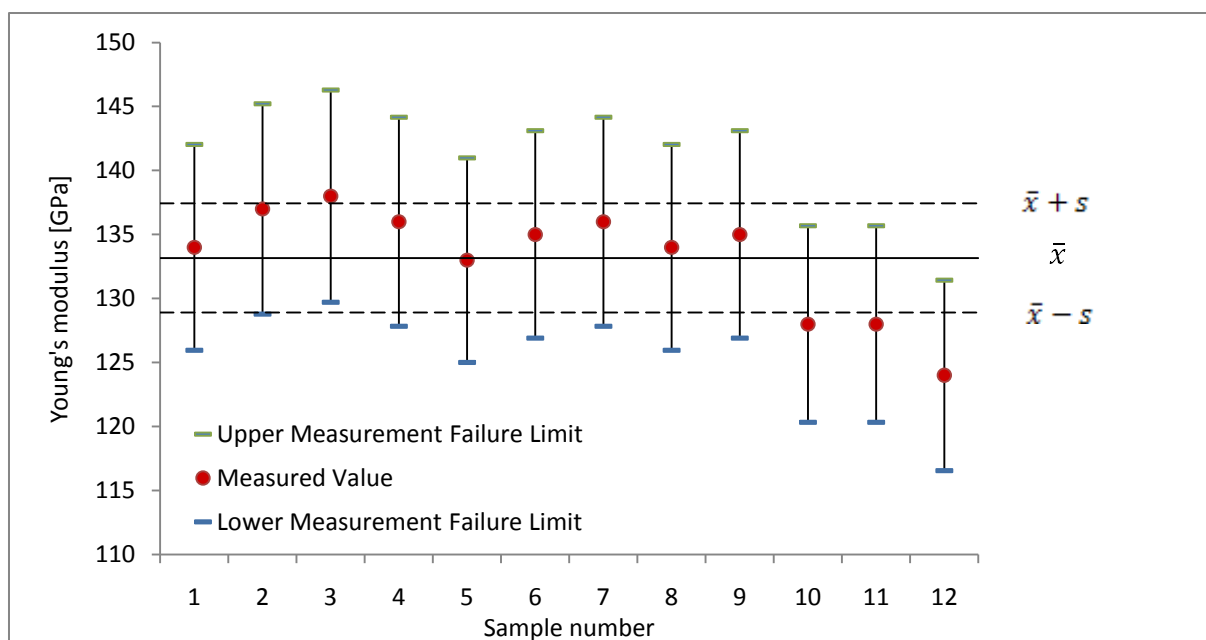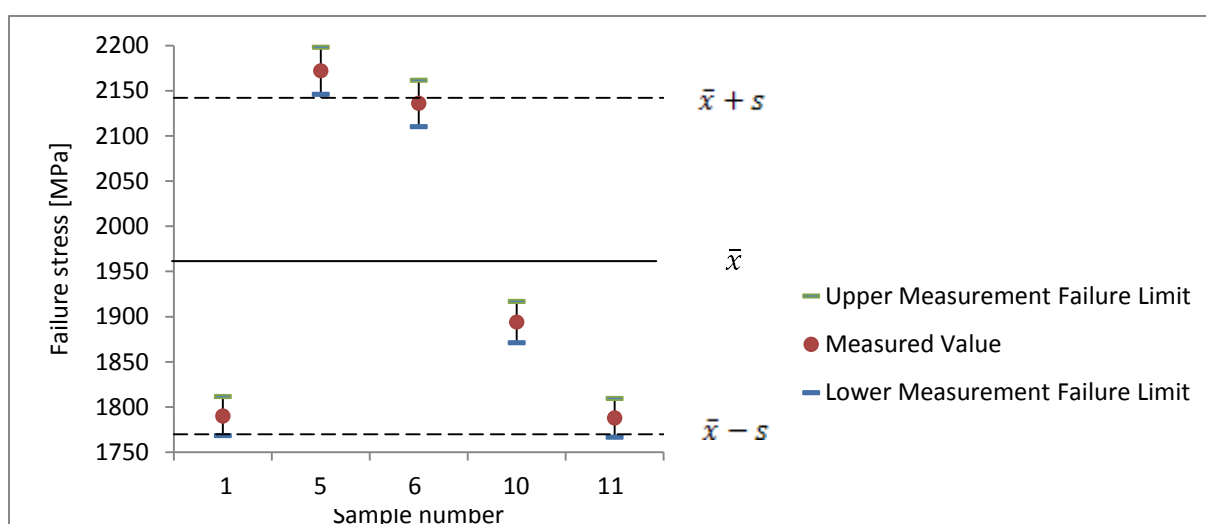

Fig. 4-32: Mean value (solid line), standard deviation (dashed lines), measured failure stress (red dots), lower and upper limits due to the failure calculation of four point bending samples C3-4P-0-01 to 11, leaving out interrupted tests, loaded parallel to the fiber orientation. Huge scatter of the values due to samples cut out of different plates.
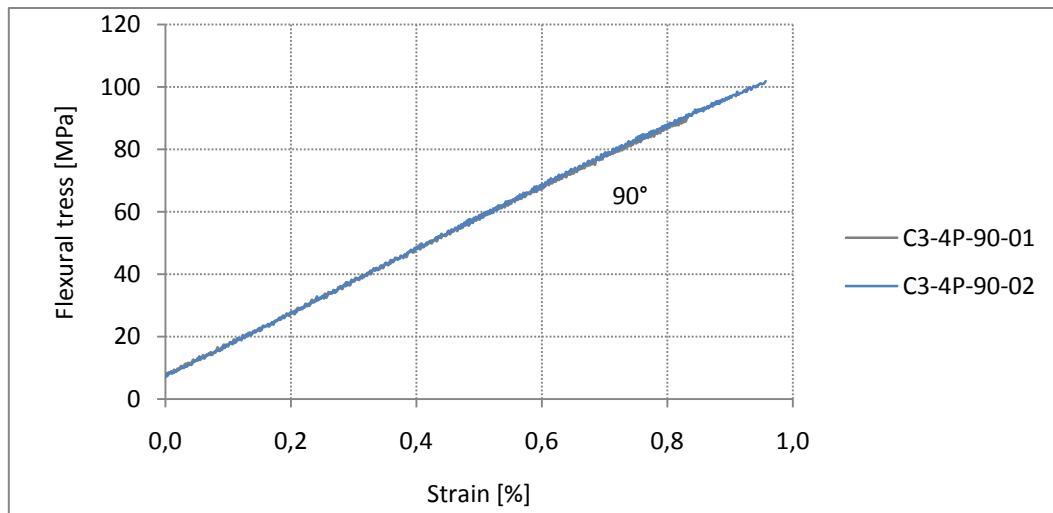
Fig. 4-33: Stress-strain diagrams of samples C3-4P-90-01 and 02 tested in 90° fiber orientation

Sample code	Sample dimensions [mm]	Young's Modulus [GPa]	Mean Young's Modulus [GPa]	Failure Stress [MPa]	Mean Failure Stress [MPa]	Failure Strain [%]	Mean Failure Strain [%]
C3-4P-90-01	14,66x1,80	10,0	10,1 ± 0,1	90	96 ± 9	0,83	0,9 ± 0,1
C3-4P-90-02	15,33x1,80	10,2		102		0,96	

Table 4-11: Mechanical properties of samples cured with curing cycle C3 tested in 90° fiber orientation

4.2.3 Torsion

Figure 4-34 shows the stress-strain diagram of samples P10-1 and 2 stressed until failure without hysteresis loops and figure 4-35 the stress-strain diagram of sample P10-3 loaded with three hysteresis loops at 10°, 20° and 30°. Table 4-12 contains the shear modulus, failure stress and failure strain including the average values of all samples tested. Testing of samples P10-04 and 05 was interrupted for CT investigation but did not show any indication of failure. Samples P10-01, 02 and 06 failed at the points of fixture and therefore could not be taken into account.
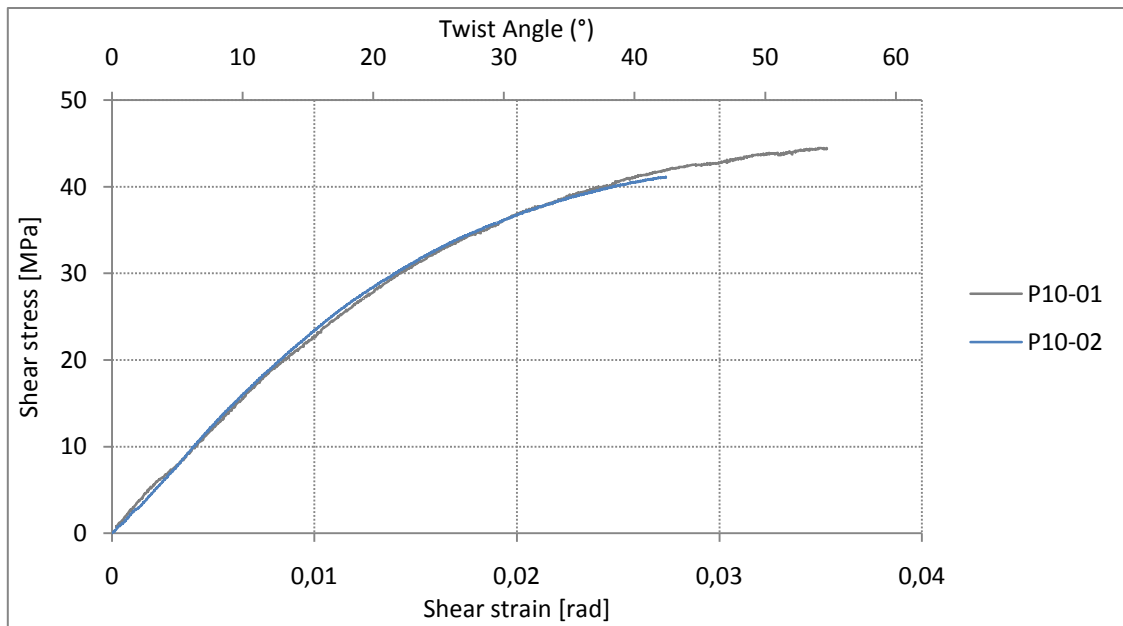
Fig. 4-34: Shear stress over twist angle/shear strain of samples P10-01 and 02
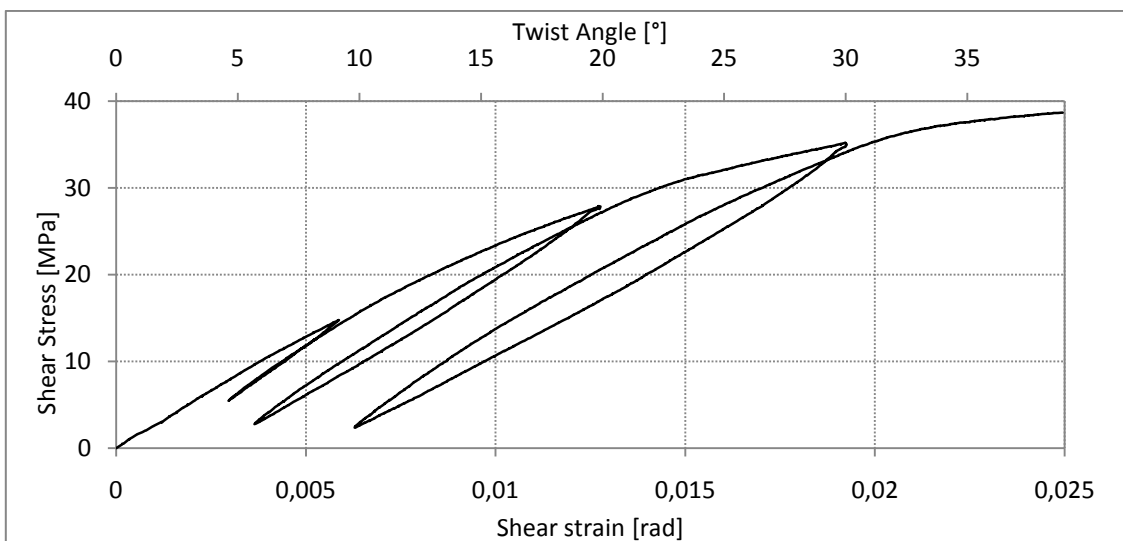
Fig. 4-35: Shear stress over twist angle/shear strain of sample P10-3

Sample code	Sample dimensions D_oxD_ixL [mm]	Shear Modulus [GPa]	Mean Shear Modulus [GPa]	Failure Stress [MPa]	Mean Failure Stress [MPa]	Failure Strain [rad]	Mean Failure Strain [rad]
P10-01	9,85x7,9x200	2,3	2,5 ± 0,2	44,4	42,8 ± 2,3	0,035	0,03 ± 0,01
P10-02	9,85x7,9x200	2,6		41,1		0,027	
P10-03	9,85x7,9x200	3,1	3,2 ± 0,3	38,6	39,3 ± 0,9	0,025	0,03 ± 0,01
P10-04	9,85x7,9x200	3,3		(33,5)		(0,018)	
P10-05	9,85x7,9x200	3,4		(39,2)		(0,025)	
P10-06	9,85x7,9x200	2,8		39,9		0,037	

Table 4-12: Mechanical Properties of samples P10-01 to 06.

Numbers in brackets refer to interrupted test due to further investigations (CT).

4.2.4 Acoustic Emission (AE) Measurements

4.2.4.1 Four Point Bending

Figures 4-36 a)-h) show the results of the AE measurements during four point bending. The blue graph presents the flexural stress over time curve and the black graph the AE count rate over time. For samples tested using hysteresis cycles, peaks in the count rate at a step in the loading curve indicates damage of the specimen. Figures 4-37 a) and b) contain the flexural stress and AE count rate over time curves of samples C0-4P-015 and 16. With this type of testing someone can exclude the possibility that recorded AE events originate from friction between the supports and the samples. Furthermore the "Kaiser effect" can be shown meaning that new AE events only occur if the stress limit of the last AE event is exceeded. Therefore samples were loaded once until 300N for calculation of the Young's modulus and then 5 times with a load limit of 600N and 850N respectively.

a)

b)

c)

d)

e)

f)

g)

h)
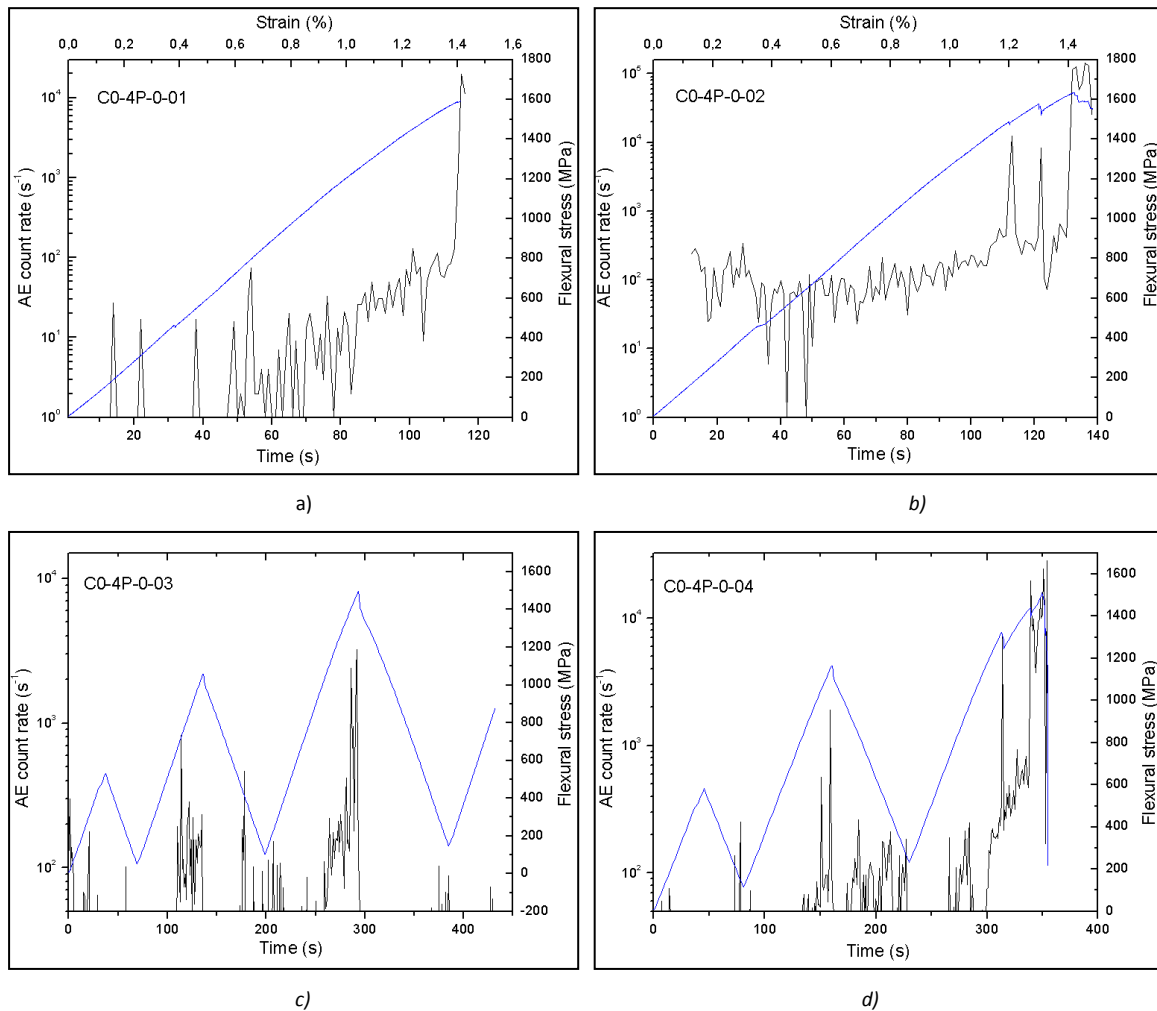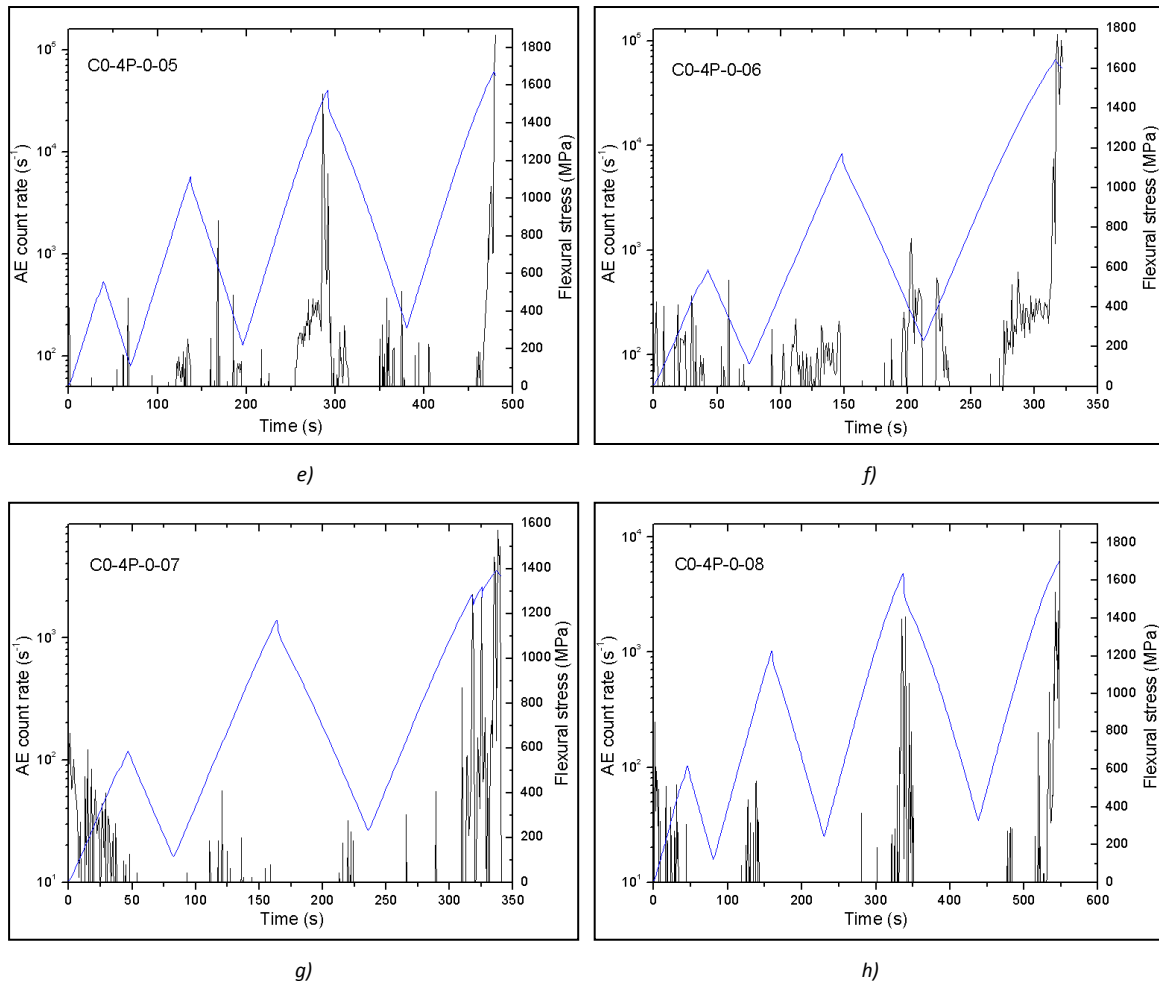
Fig. 4-36: AE count rate and flexural stress over time of samples C0-4P-0-01 to 08

a - b) Continuously tested samples until failure

c – h) Samples tested with hysteresis loops. Reversal points at 300N, 600N and 850N.

Testing of samples 03 and 07 was interrupted

a)

b)
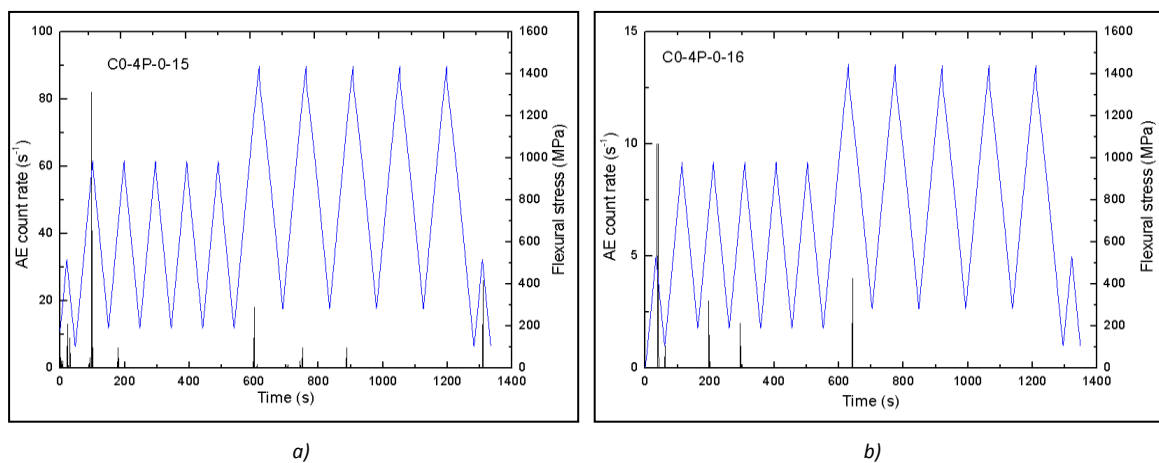
Fig. 4-37: AE count rate and flexural stress over time of samples C0-4P-0-15 and 16

Reversal points at 300N, 600N and 850N

4.2.4.2 Torsion

Figures 4-38 a)-f) present the results of the AE measurements during torsion tests. The blue graph presents the shear stress over time and the black graph the AE count rate over time. Samples P10-01 and 02 were stressed continuously and the twist angle is given in addition. Samples P10-03 to 06 were loaded using hysteresis loops with the reversal points at 10°, 20° and 30°. It can be seen that AE events are recorded from the beginning of the test. The last peak of the AE count rate of sample P10-01, 02, 03 and 06 labels the total failure of the sample.

a)   *b)*

c)   *d)*

e)   f)
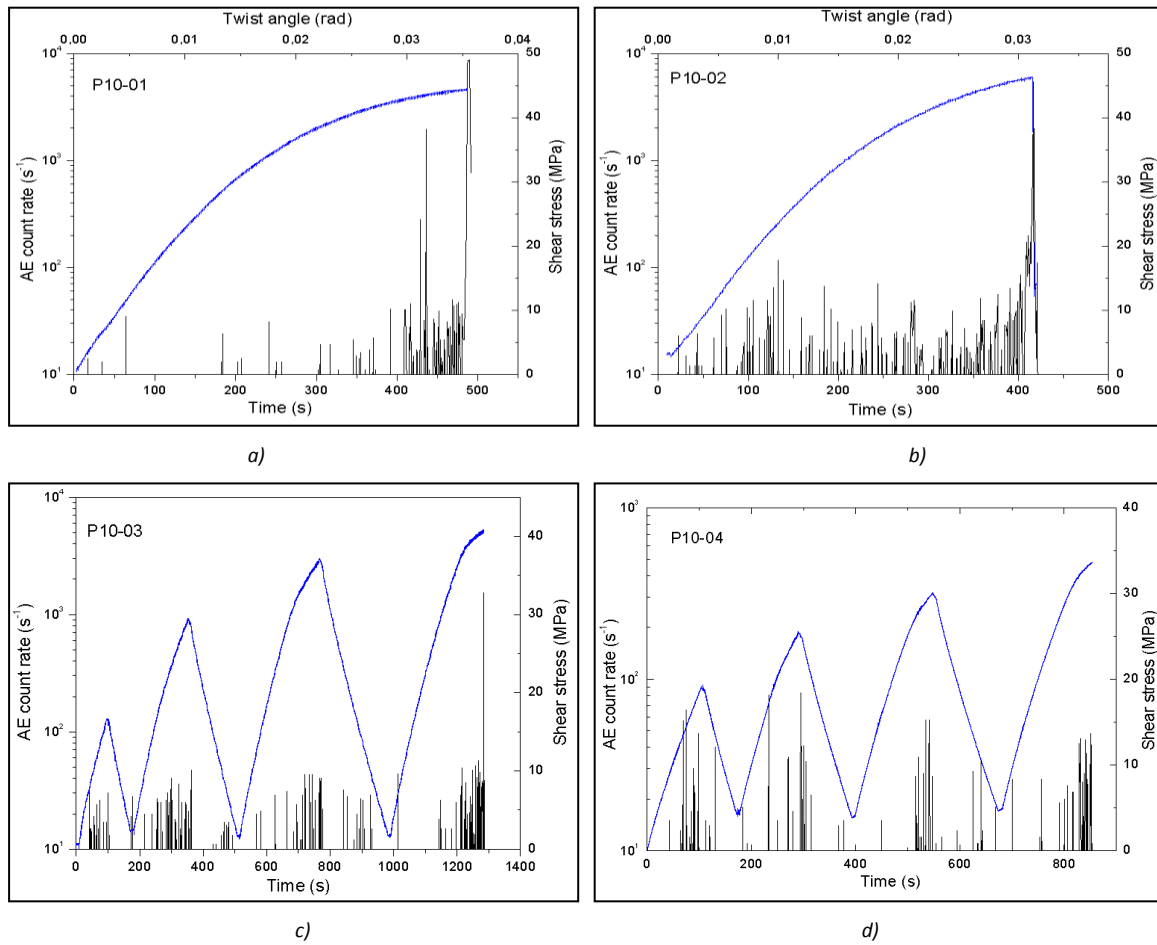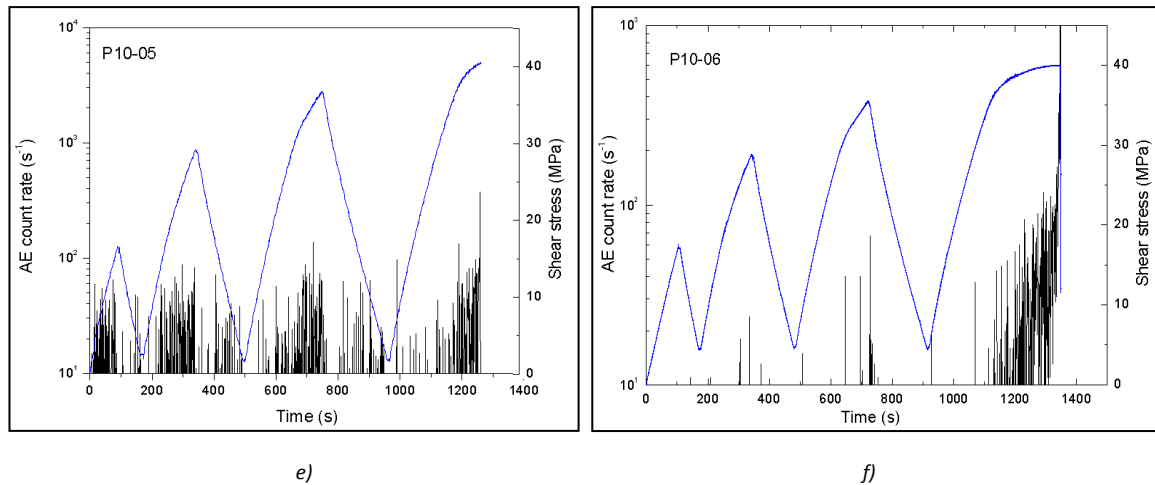
Figure 4-38: Shear stress over twist angle/time and AE count rate over time diagrams

a, b): Samples P10-01 and 02 stressed continuously

c – f): Samples P10-03 to 06 stressed with hysteresis loops. Reversal points at 10°, 20° and 30°.

Testing of samples P10-04 and 05 was interrupted

4.2.5 Interlaminar Fracture Toughness

4.2.5.1 Mode I

The force versus displacement curves of samples C0-I-01 to 04 are displayed in figure 4-39 a)-d) and figure 4-41 a)-d) shows the same curves of samples C3-I-01 to 04. Figure 4-40 and 4-42 illustrate the interlaminar fracture toughness for every loading-unloading cycle of each sample and tables 4-13 and 4-14 contain the values in table form. Thus the average value for curing cycle C0 and C3 can be calculated. The interlaminar fracture toughness of samples C0 is lower than the one for samples C3 meaning that more energy is needed to propagate the crack as expected. The scatter of the critical energy release rate of both sample types is in the same range and can be explained generally by the rather poor magnification of the magnifying glass and the subsequent failure of crack length determination.

a)   b)
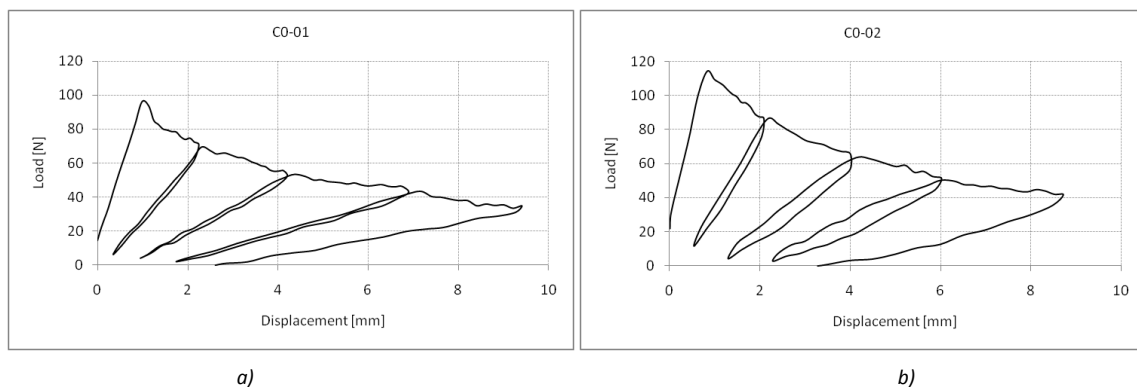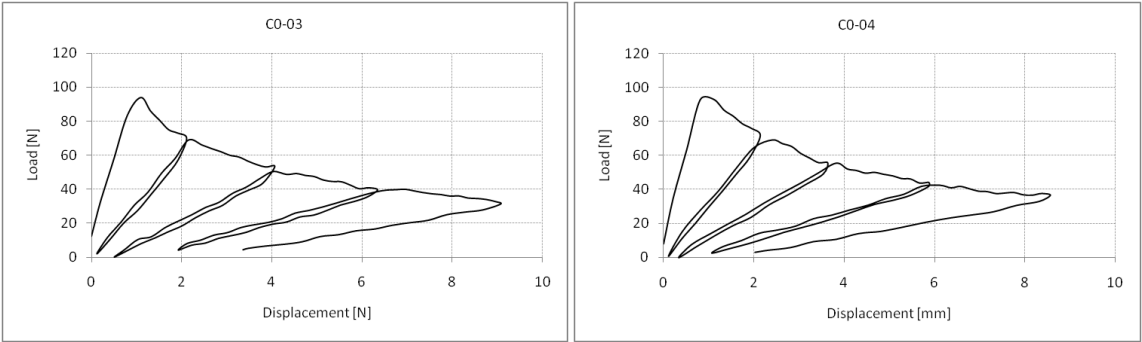
c)   d)

Fig. 4-39: Load versus displacement curves of samples C0-I-01 to 04

Fig. 4-40: Interlaminar fracture toughness of samples C0-I-01 to 04 including the mean value (dashed line)

Sample code	Interlaminar fracture toughness G_{Ic} [J/mm²]	Mean interlaminar fracture toughness G_{Ic} [J/mm²]
C0-I-01	0,312	
C0-I-02	0,349	0,31 ± 0,03
C0-I-03	0,284	
C0-I-04	0,296	

Table 4-13: Interlaminar fracture toughness G_{Ic} of samples C0-I-01 to 04

a)   b)

c)   *d)*
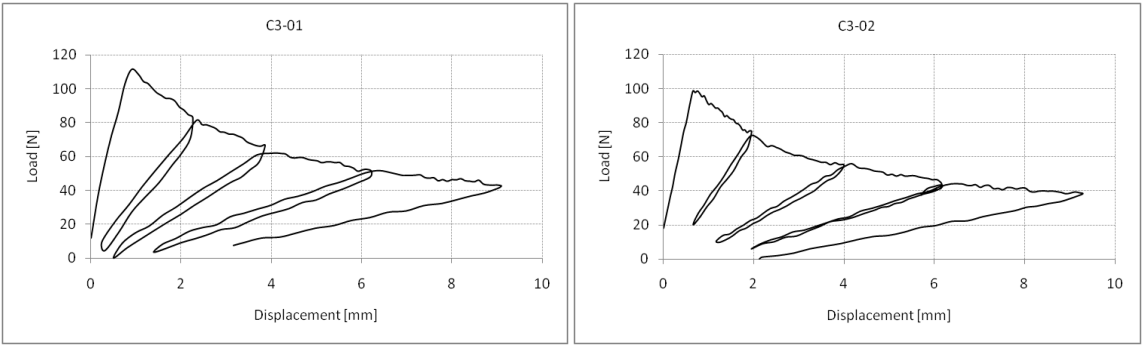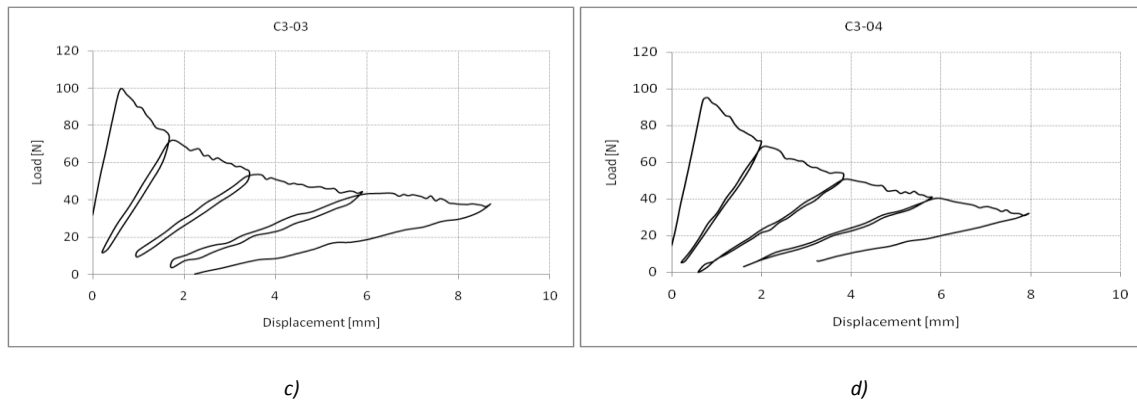
Fig. 4-41: Load versus displacement curves of samples C3-I-01 to 04

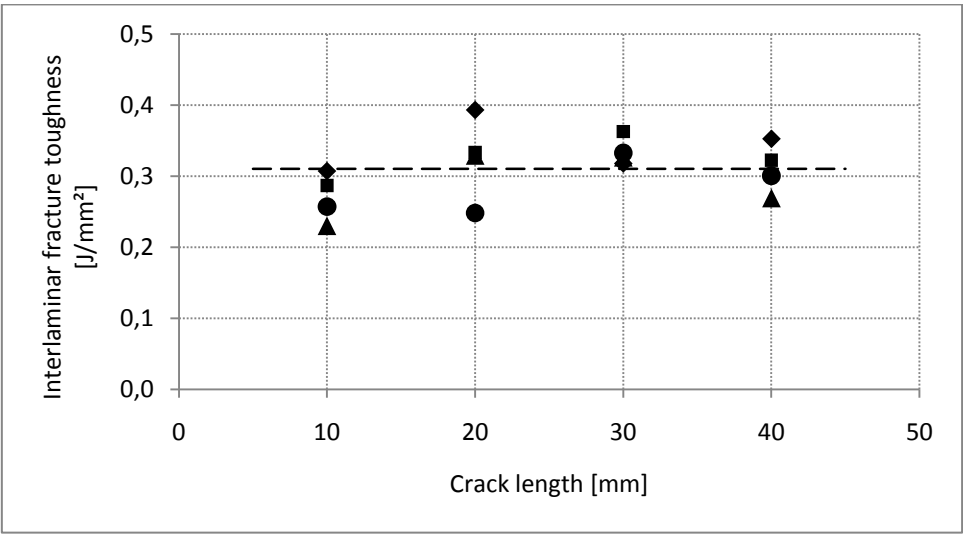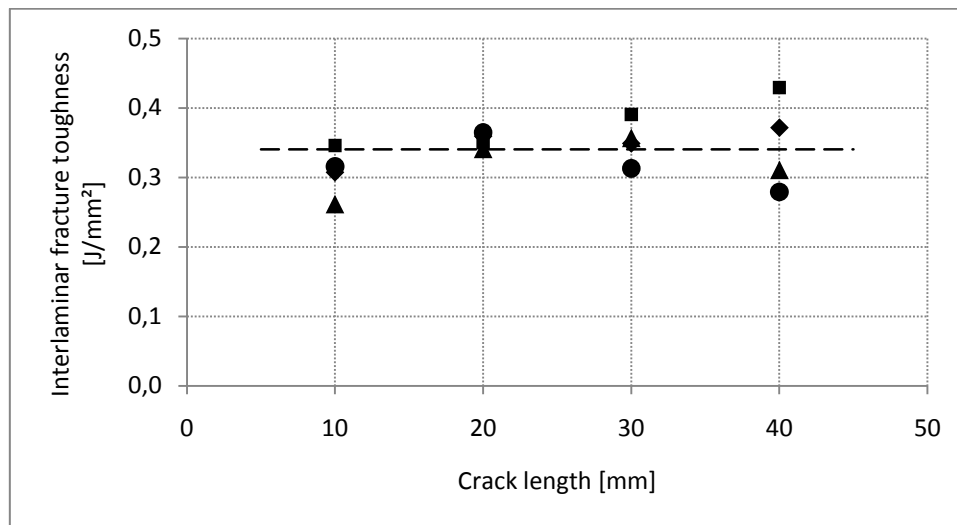Fig. 4-42: Interlaminar fracture toughness of samples C3-I-01 to 04 and mean value (dashed line)

Sample code	Interlaminar fracture toughness G_{Ic} [J/mm²]	Mean Interlaminar fracture toughness G_{Ic} [J/mm²]
C0-I-01	0,379	
C0-I-02	0,347	0,34 ± 0,03
C0-I-03	0,318	
C0-I-04	0,318	

Table 4-14: Interlaminar fracture toughness G_{Ic} of samples C3-I-01 to 04

4.2.5.2 Mode II

The load versus displacement curves of Mode II measurements of sample C0-II-01 to 04 are displayed in figure 4-43. Figure 4-44 shows the same curves of samples C3-II-01 to 04. The diagrams depict a linear load increase until the crack propagates leading to a sudden drop in the load curve. The interlaminar fracture toughness G_{IIc} was about 30% higher in case of the C3 samples compared to the C0 samples (Table 4-15 and 4-16). One of the C3 samples showed a decrease of the load at about 70N and a consequently minor gradient leading to a greater scatter of the values.

Fig. 4-43: Load versus displacement curve of samples C0-II-01 to 04

Sample code	Interlaminar fracture toughness G_{IIc} [J/mm²]	Mean interlaminar fracture toughness G_{IIc} [J/mm²]
C0-II-01	0,662	
C0-II-02	0,667	0,67 ± 0,01
C0-II-03	0,688	
C0-II-04	0,655	

Table 4-15: Interlaminar fracture toughness G_{IIc} of samples C3-II-01 to 04

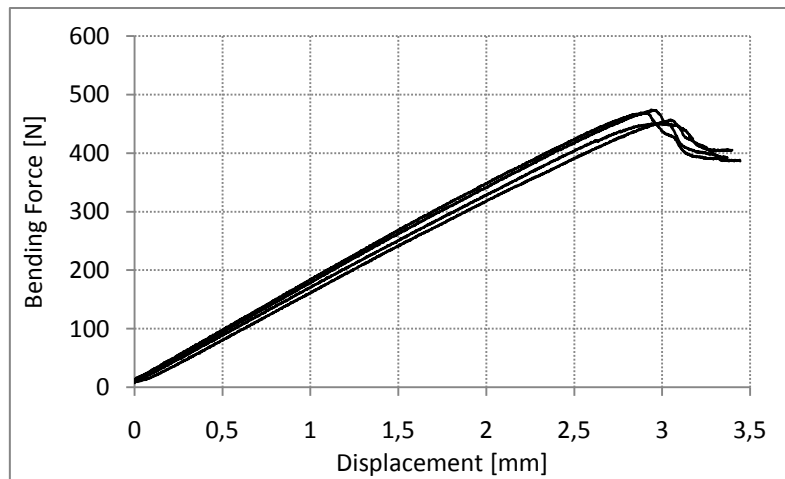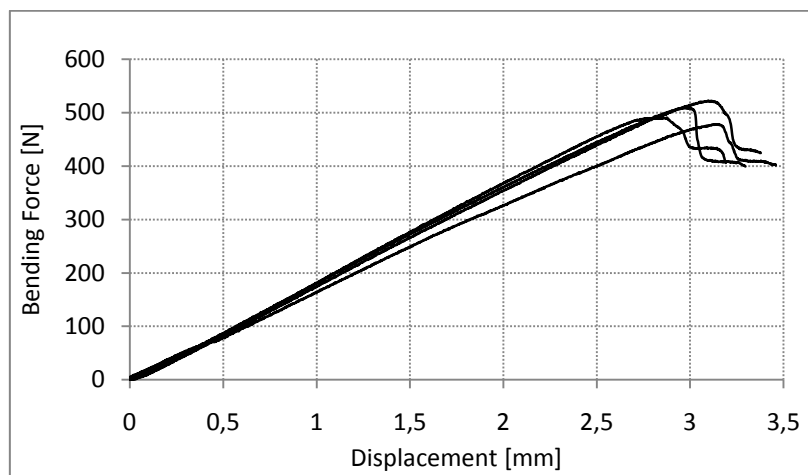*Fig. 4-44: Load versus displacement curve of samples C3-II-01 to 04*

Sample code	Interlaminar fracture toughness G_{IIc} [J/mm²]	Mean interlaminar fracture toughness G_{IIc} [J/mm²]
C3-II-01	0,876	
C3-II-02	0,810	0,88 ± 0,06
C3-II-03	0,888	
C3-II-04	0,943	

Table 4-16: Interlaminar fracture toughness G_{IIc} of samples C3-II-01 to 04

4.3 Thermo-Mechanical Analysis

4.3.1 DMA

<u>C0 Laminates</u>

Figure 4-45 shows the general information of samples C0 obtained by DMA. The solid line refers to the storage modulus, the dash-dotted line to the loss modulus and the dashed line to the loss factor tan δ. Figure 4-46 comprises only the storage modulus and the loss factor curves of samples C0-DMA-01 to 03 as the glass transition temperature was only obtained from these two curves. At room temperature the loss modulus is two orders of magnitude lower than the storage modulus. Therefore the young's modulus is represented by the storage modulus only. Table 4-17 contains the storage modulus at room temperature, the glass transition temperature determined from the storage modulus and the loss factor curves and the average values. The systematic error of the measurement was estimated to be ± 5% in case of the stiffness and ± 2% in case of the temperature measurement. If the standard deviation of the values is minor than the limits obtained by the systematic error, the latter limits are given in the table.

Fig. 4-45: Storage modulus (solid line), loss modulus (dash-dotted line) and loss factor (dashed line) for sample C0-DMA-01 without prior mechanical loading

Fig. 4-46: Overlay of storage modulus (solid line) and loss factor (dashed line) of samples C0-DMA-01 to 03 without prior mechanical loading

Sample code	Storage modulus [GPa]	Mean storage modulus [GPa]	T_g (Storage modulus) [°C]	Mean T_g (Storage modulus) [°C]	T_g (loss factor) [°C]	Mean T_g (loss factor) [°C]
C0-DMA-01	110		226		226	
C0-DMA-02	122	117 ± 6	221	222 ± 4	224	225 ± 5
C0-DMA-03	119		220		225	

Table 4-17: Storage modulus at room temperature, glass transition temperature and average values

of samples C0-DMA-01 to 03 without prior mechanical loading

<u>C3 Laminates</u>

Figure 4-47 shows the general information of samples C3 obtained by DMA. The solid line refers to the storage modulus, the dash-dotted line to the loss modulus and the dashed line to the loss factor tan δ. Figure 4-48 comprises only the storage modulus and the loss factor curves of samples C3-DMA-01 to 03 as the glass transition temperature was only obtained from these two curves. At room temperature the loss modulus is two orders of magnitude lower than the storage modulus. Therefore the Young's modulus is represented by the storage modulus only (cf. fig. 3-19). Table 4-18 contains the Young's modulus (=storage modulus at room temperature), the glass transition temperature determined from the storage modulus and the loss factor curves and the average values. The systematic error of the measurement was estimated to be ± 5% in case of the stiffness and ± 2% in case of the temperature measurement. If the standard deviation of the values is minor than the limits obtained by the systematic error, the latter limits are given in the table.
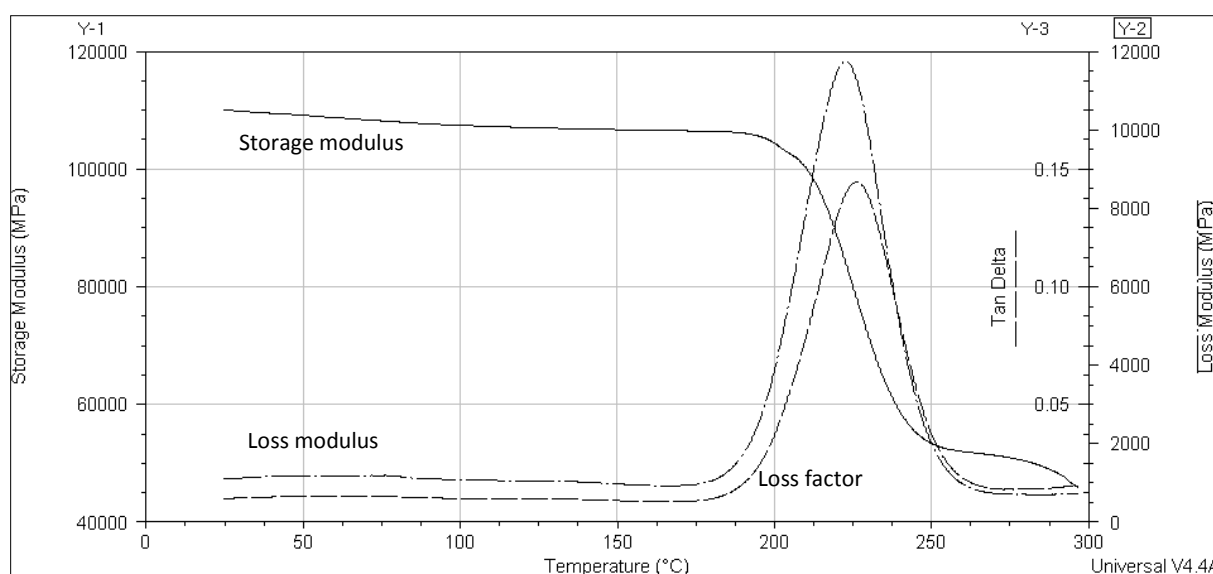
Fig. 4-47: Storage modulus (solid line), loss modulus (dash-dotted line) and loss factor (dashed line) for sample C3-DMA-02
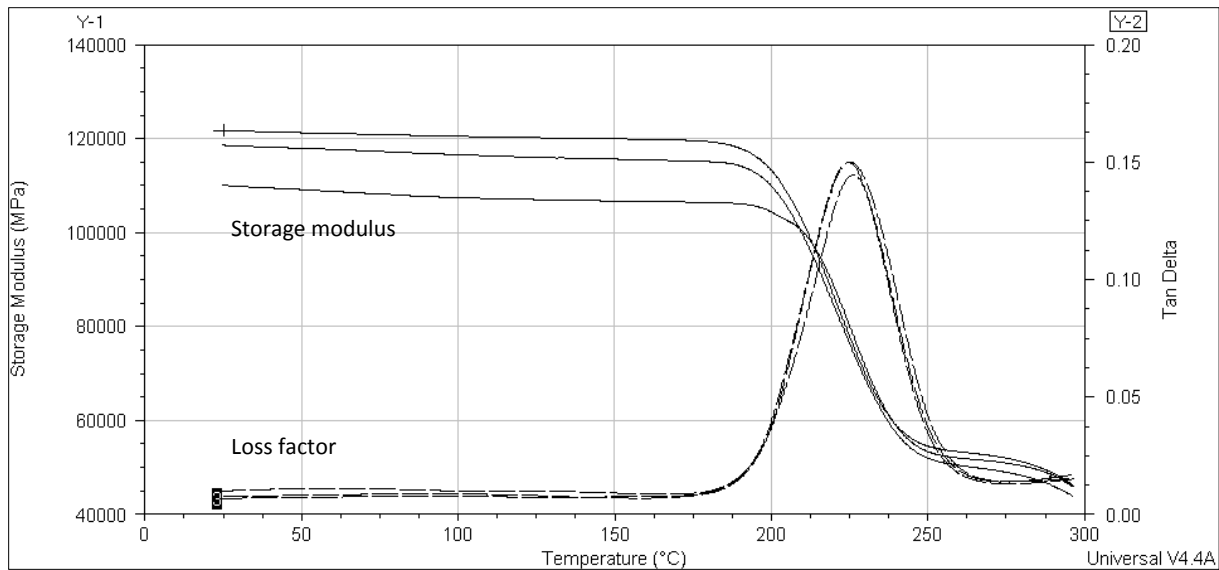
without prior mechanical loading

Fig. 4-48: Overlay of storage modulus (solid line) and loss factor (dashed line) of samples C3-DMA-01 to 03 without prior mechanical loading

Sample code	Storage modulus [GPa]	Mean Storage modulus [GPa]	T_g (Storage modulus) [°C]	Mean T_g (Storage modulus) [°C]	T_g (loss factor) [°C]	Mean T_g (loss factor) [°C]
C3-DMA-01	111		220		227	
C3-DMA-02	120	119 ± 7	216	217 ± 4	222	223 ± 5
C3-DMA-03	125		215		220	

Table 4-18: Storage modulus at room temperature, glass transition temperature and average values

of samples C3-DMA-01 to 03 without prior mechanical loading

C0 and C3 after mechanical loading

Figure 4-49 and 4-50 illustrate the storage modulus and the loss factor of samples C0 and C3-DMA-04 and 05. These four samples were loaded using hysteresis loops up to 95% of the average maximum failure stress prior to DMA analysis. Table 4-19 and 4-20 contain the young's modulus (=storage modulus at room temperature), the glass transition temperature determined from the storage modulus and the loss factor curves and the average values. The systematic error of the measurement was estimated to be ± 5% in case of the stiffness and ± 2% in case of the temperature measurement. If the standard deviation of the values is minor than the limits obtained by the systematic error, the latter limits are given in the table.
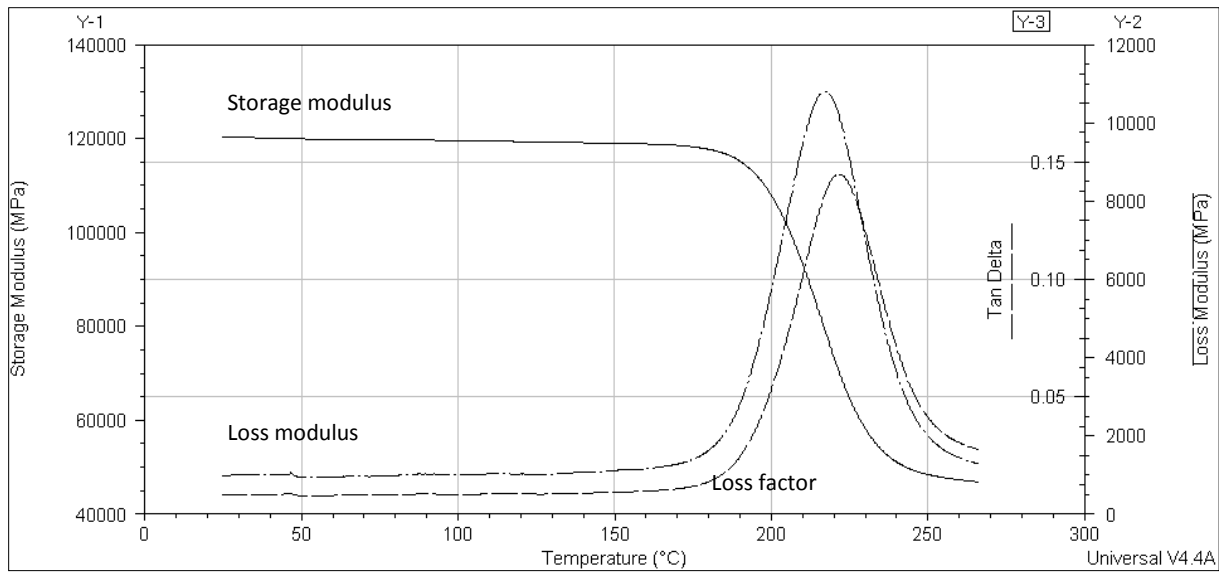

Fig. 4-49: Overlay of storage modulus (solid line) and loss factor (dashed line) of samples C0-DMA-04 and 05 after mechanical loading (four point bending)

Sample code	Storage modulus [GPa]	Mean storage modulus [GPa]	T_g (Storage modulus) [°C]	Mean T_g (Storage modulus) [°C]	T_g (loss factor) [°C]	Mean T_g (loss factor) [°C]
C0-DMA-04	110	113 ± 6	211	212 ± 4	220	221 ± 4
C0-DMA-05	115		212		221	

Table 4-19: Storage modulus at room temperature, glass transition temperature and average values of samples C0-DMA-04 and 05 after mechanical loading

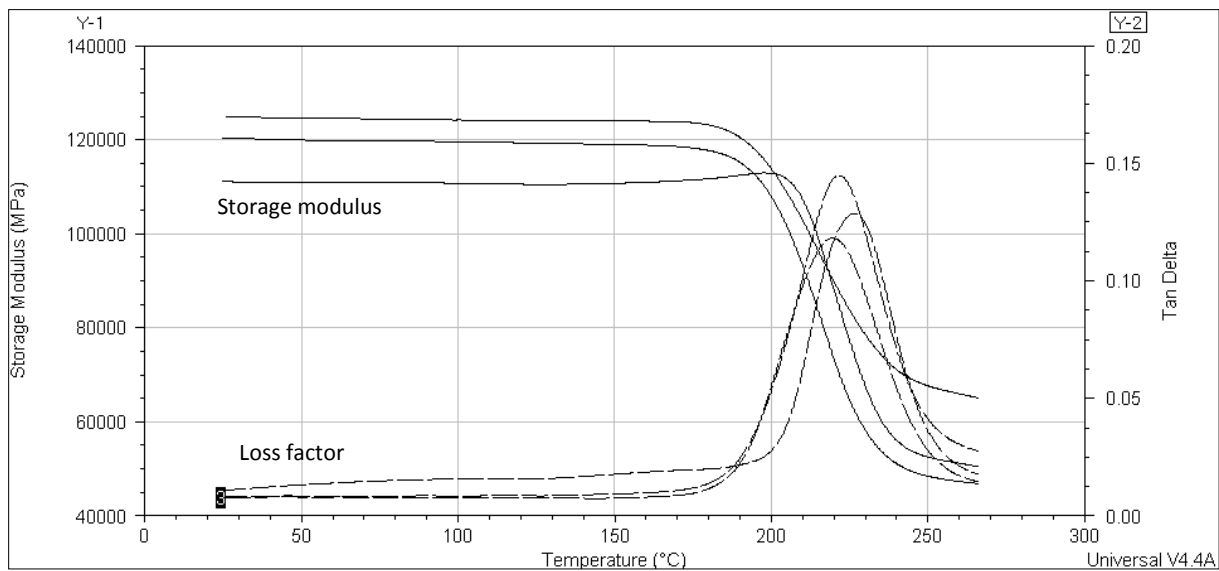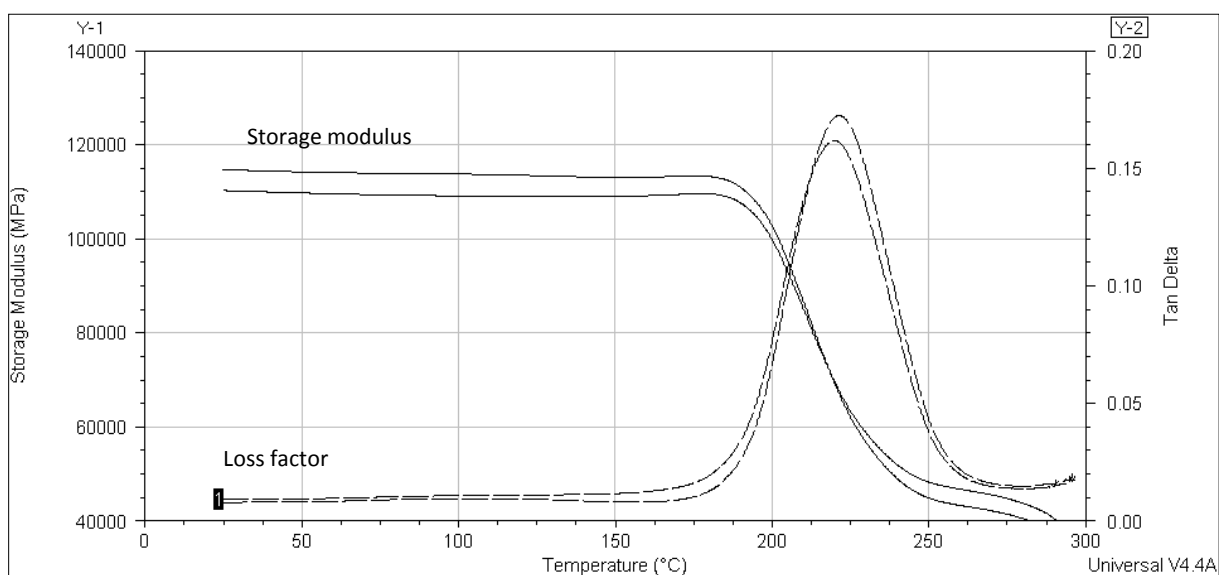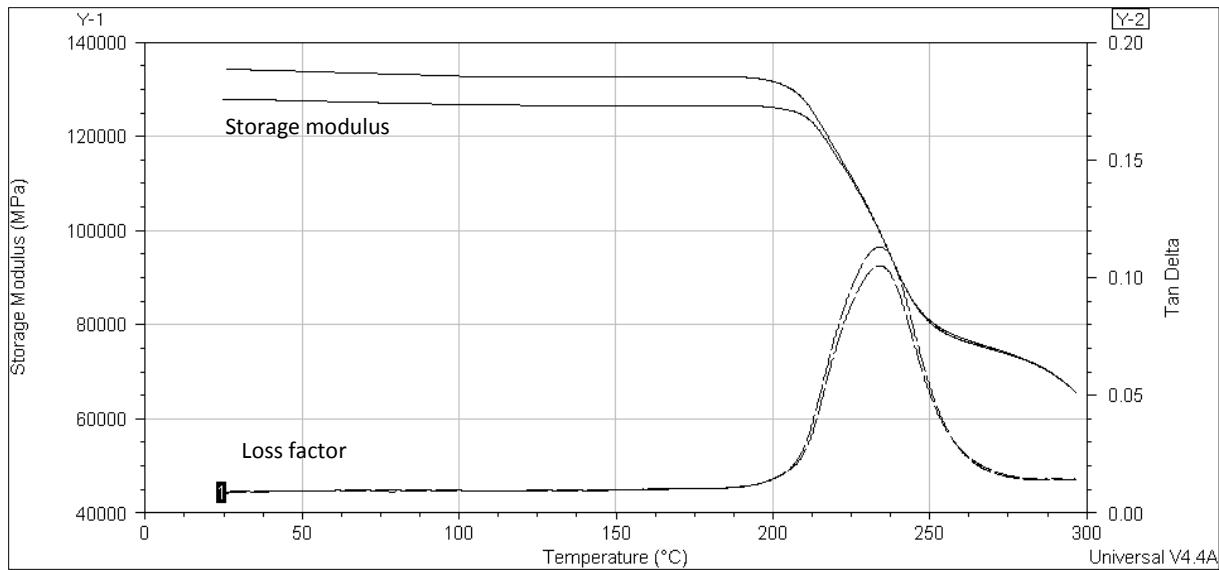*Fig. 4-50: Overlay of storage modulus (solid line) and loss factor (dashed line) of samples C3-DMA-04 and 05 after*

mechanical loading (four point bending)

Sample code	Storage modulus [GPa]	Mean Storage modulus [GPa]	T_g (Storage modulus) [°C]	Mean T_g (Storage modulus) [°C]	T_g (loss factor) [°C]	Mean T_g (loss factor) [°C]
C3-DMA-04	134	131 ± 7	237	237 ± 5	234	234 ± 5
C3-DMA-05	128		237		234	

Table 4-20: Storage modulus at room temperature, glass transition temperature and average values

of samples C3-DMA-04 and 05 after mechanical loading

4.3.2 DSC

<u>C0 Laminates</u>

Figure 4-51 presents the reversible-, the non reversible-, and the overall heat flow of sample C0-DSC-01 and the glass transition temperature at the only significant step of the reversible heat flow curve. The reversible heat flow curves of all C0 samples are given in figure 4-52 showing that the higher the heating rate the more distinctive is the step in the curve. Table 4-21 contains the glass transition temperatures and the heating rate in accordance.

Fig. 4-51: Reversible-, non reversible-, overall heat flow of sample C0-DSC-01 (3°C/min) and evaluation of the glass transition temperature using the reversible heat flow. First temperature T_A, second T_g and third T_E (according to fig. 4-20 b)

Fig.4-52: Overlay of the reversible heat flow curves of sample C0-DSC-01 to 07 and determination of the glass transition temperatures T_g. First temperature: T_A, second: T_g and third: T_E (according to fig. 4-20 b)

Sample code	Heating rate [°C/min]	Glass transition temperature [°C]	Mean glass transition temperature [°C]
C0-DSC-01	3	217	
C0-DSC-02	3	214	
C0-DSC-03	5	217	
C0-DSC-04	5	215	211 ± 6
C0-DSC-05	10	211	
C0-DSC-06	10	205	
C0-DSC-07	10	200	

Table 4-21: Heating rate, glass transition temperatures T_g and average value of samples C0-DSC-01 to 07

C3 Laminates

Figure 4-53 shows the reversible-, the non reversible-, and the overall heat flow of sample C3-DSC-01 and the glass transition temperature at the only significant step of the reversible heat flow curve. The reversible heat flow curves of all C3 samples are given in figure 4-54 showing that the higher the heating rate the more distinctive is the step in the curve. Table 4-22 contains the glass transition temperatures and the heating rate in accordance.
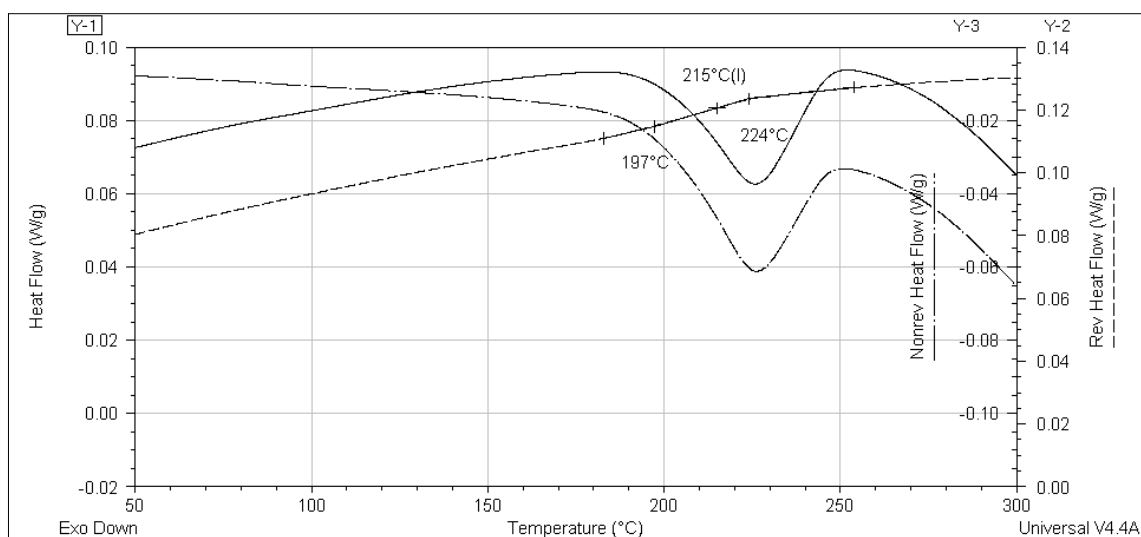

Fig. 4-53: Reversible-, non reversible-, overall heat flow of sample C3-DSC-01 (3°C/min) and evaluation of the glass transition temperature using the reversible heat flow. First temperature T_A, second T_g and third T_E (according to fig. 4-20 b)

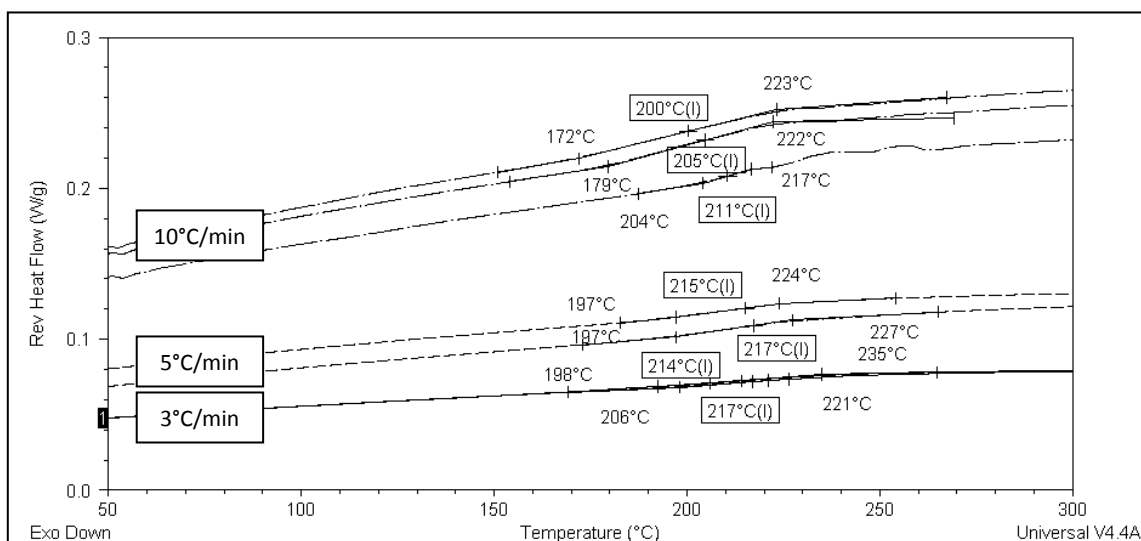
Fig. 4-54: Overlay of the reversible heat flow curves of sample C3-DSC-01 to 07 and determination of the glass transition temperatures. First temperature T_A, second T_g and third T_E (according to fig. 4-20 b)

Sample code	Heating rate [°C/min]	Glass transition temperature [°C]	Mean glass transition temperature [°C]
C3-DSC-01	3	210	
C3-DSC-02	3	213	
C3-DSC-03	5	200	
C3-DSC-04	5	210	208 ± 5
C3-DSC-05	10	214	
C3-DSC-06	10	202	
C3-DSC-07	10	207	

Table 4-22: Heating rate, glass transition temperatures T_g and average value of samples C3-DSC-01 to 07

Tubes

Figure 4-55 shows again the reversible-, non reversible-, and overall heat flow of sample P10-DSC-01 and figure 4-56 only the reversible heat flow of all pultruded samples tested. As already mentioned the step in the curve to determine the glass transition temperature is more significant the higher the heating rate. Table 4-23 comprises the glass transition temperatures and the heating rate.
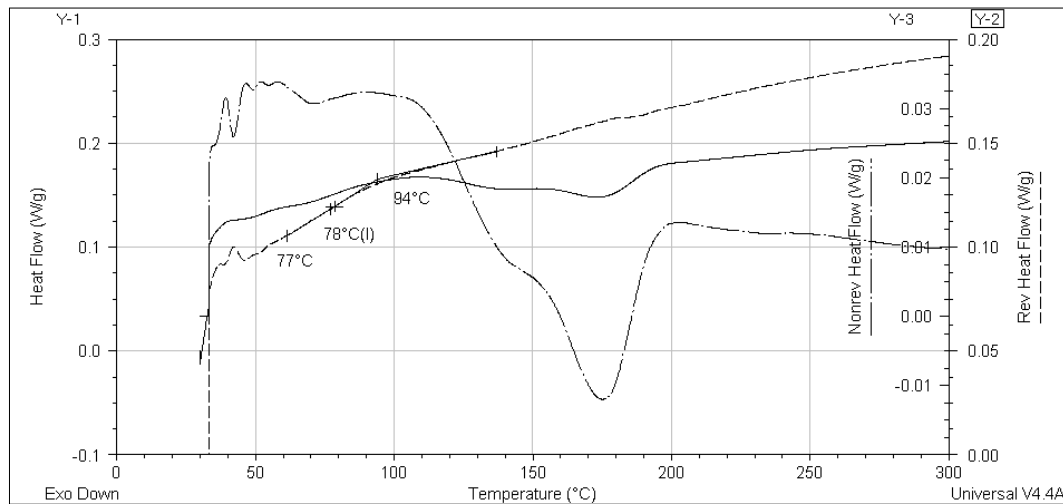
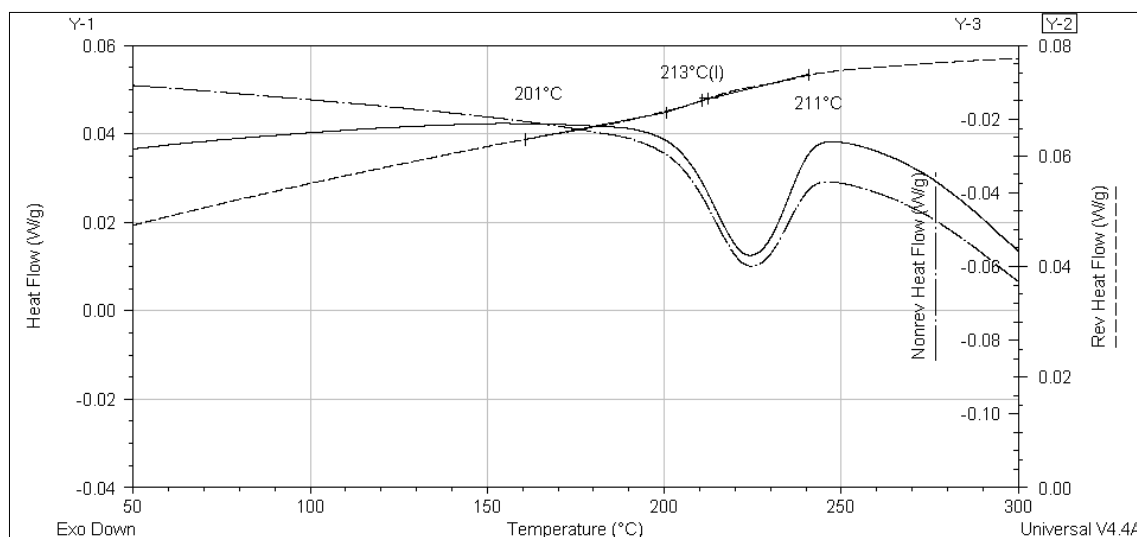*Fig. 4-55: Reversible-, non reversible-, overall heat flow of sample P10-DSC-01 and evaluation of the glass transition temperature using the reversible heat flow. First temperature T_A, second T_g and third T_E (according to fig. 4-20 b)*
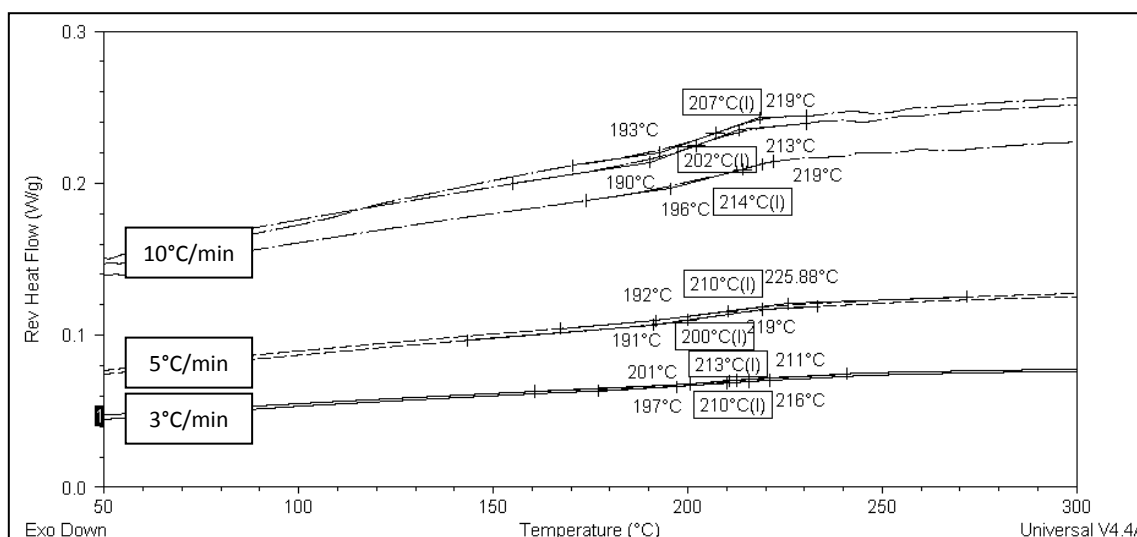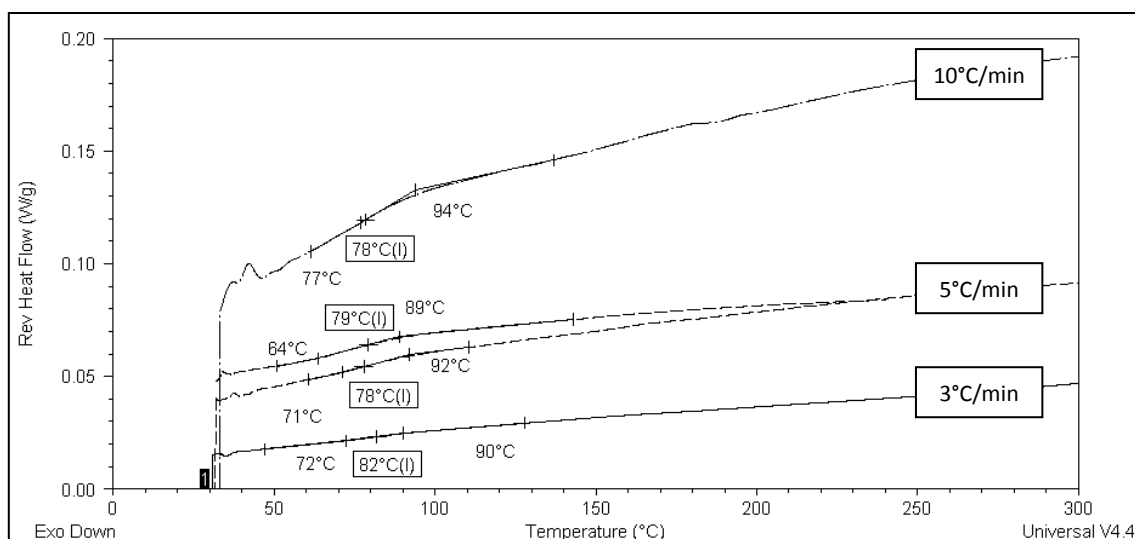
Fig. 4-56: Overlay of the reversible heat flow curves of sample P10-DSC-01 to 04 and determination of the glass transition temperatures.

First temperature T_A, second T_g and third T_E (according to fig. 4-20 b)

Sample code	Heating rate [°C/min]	Glass transition temperature [°C]	Mean glass transition temperature [°C]
P10-DSC-01	3	82	79 ± 2
P10-DSC-02	5	78	
P10-DSC-03	5	79	
P10-DSC-04	10	78	

Table 4-23: Heating rate, glass transition temperatures T_g and average value of samples P10-DSC-01 to 04

4.3.3 Dilatometry

<u>C0 Laminates</u>

The changes of sample length over temperature (dashed line) of samples C0-0° and C0-90° are given in figures 4-57 a) and b), respectively. Tables 4-24 and 4-25 provide the coefficient of thermal expansion for each specimen at room temperature (25°C) and below glass transition temperature as well as the glass transition temperature itself. The glass transition temperature can only be measured using the 90° samples as the intersection point of the two tangents above and below glass transition. Figure 4-57 a) only presents the second heating cycle whilst figure 4-57 b) illustrates the first and the second heating cycle showing also some irreversible processes.

Fig. 4-57 a): Thermal expansion curves (dashed lines) parallel to the fiber direction of samples C0-TMA-0-01 to 03 (top to bottom)

Fig. 4-57 b): Thermal expansion curves (dashed lines) perpendicular to the fiber direction of samples C0-TMA-90-01 to 03

Sample code	$\alpha_{0-180°C} *10^{-6}$ [°C^{-1}]	Mean $\alpha_{0-180°C} *10^{-6}$ [°C^{-1}]	$\alpha_{25°C} *10^{-6}$ [°C^{-1}]	Mean $\alpha_{25°C} *10^{-6}$ [°C^{-1}]
C0-TMA-0-01	0,4		0,3	
C0-TMA-0-02	0,1	0,2 ± 0,2	-0,2	0,0 ± 0,3
C0-TMA-0-03	0,0		0,0	

Table 4-24: Coefficient of thermal expansion α parallel to the fiber direction of samples C0-TMA-0-01 to 03

Sample code	$\alpha_{0\text{-}180°C} *10^{-6}$ [°C^{-1}]	Mean $\alpha_{0\text{-}180°C} *10^{-6}$ [°C^{-1}]	$\alpha_{25°C} *10^{-6}$ [°C^{-1}]	Mean $\alpha_{25°C} *10^{-6}$ [°C^{-1}]	Glass transition temperature [°C]	Mean glass transition temperature [°C]
C0-TMA-90-01	27		23		189	
C0-TMA-90-02	28	28 ± 1	24	24 ± 2	194	191 ± 3
C0-TMA-90-03	29		26		190	

Table 4-25: Coefficient of thermal expansion α and glass transition temperature measured perpendicular to the fiber direction

of samples C0-TMA-90-01 to 03

C3 Laminates

The changes of sample length over temperature of samples C3-0° and C3-90° are given in figures 4-58 a) and b), respectively. Tables 4-26 and 4-27 provide the coefficient of thermal expansion for each specimen at room temperature (25°C) and below glass transition temperature as well as the glass transition temperature itself. The glass transition temperature can only be measured using the 90° samples as the intersection point of the two tangents above and below glass transition. Figure 4-58 a) only presents the second heating cycle whilst figure 4-58 b) illustrates the first and the second heating cycle showing also some irreversible processes.
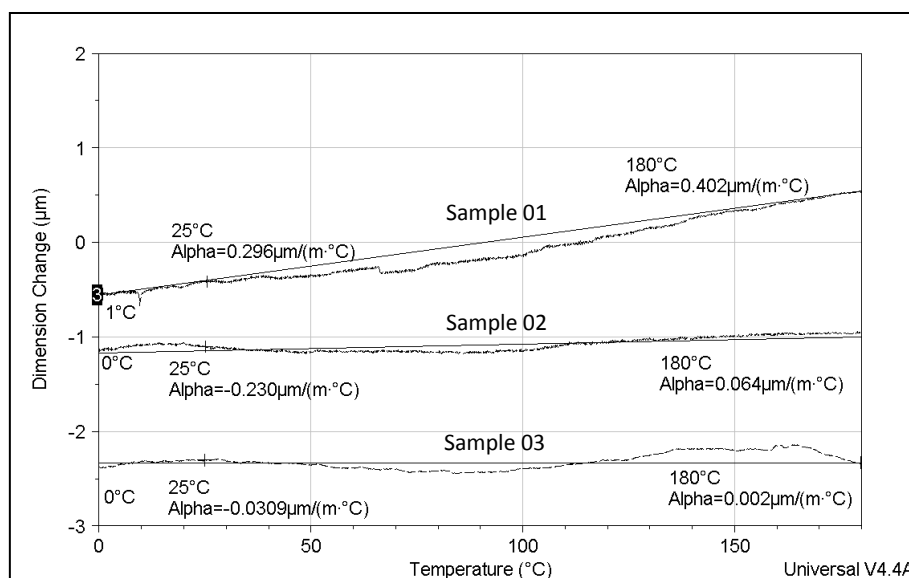

Fig. 4-58 a): Thermal expansion curves (dashed lines) parallel to the fiber direction of samples C3-TMA-0-01 to 03
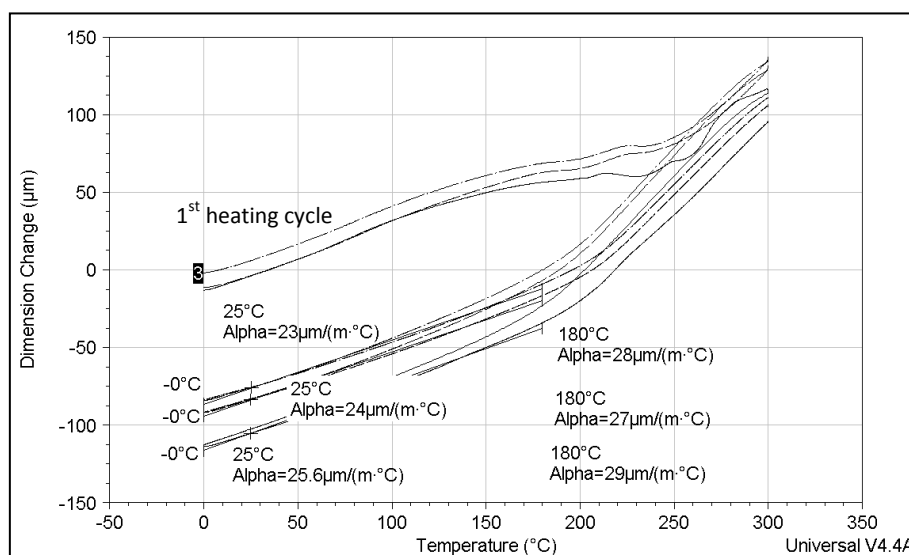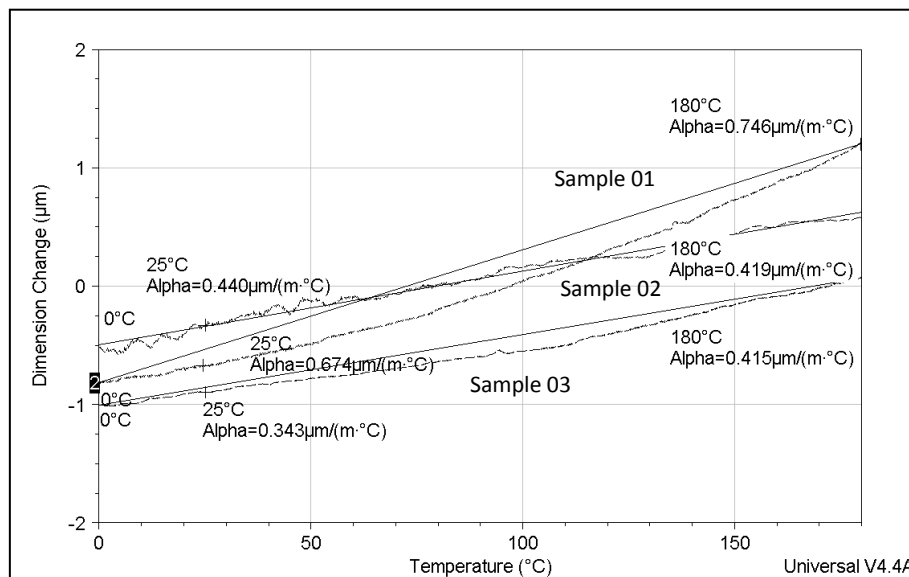
Fig. 4-58 b): Thermal expansion curves (dashed lines) perpendicular to the fiber direction of samples C3-TMA-90-01 to 03

Sample code	$\alpha_{0\text{-}180°C} *10^{-6}$ [°C^{-1}]	Mean $\alpha_{0\text{-}180°C} *10^{-6}$ [°C^{-1}]	$\alpha_{25°C} *10^{-6}$ [°C^{-1}]	Mean $\alpha_{25°C} *10^{-6}$ [°C^{-1}]
C3-TMA-0-01	0,7		0,7	
C3-TMA-0-02	0,4	0,5 ± 0,2	0,4	0,5 ± 0,2
C3-TMA-0-03	0,4		0,3	

Table 4-26: Coefficient of thermal expansion α parallel to the fiber direction of samples C3-TMA-0-01 to 03

Sample code	$\alpha_{0\text{-}180°C} *10^{-6}$ [°C^{-1}]	Mean $\alpha_{0\text{-}180°C} *10^{-6}$ [°C^{-1}]	$\alpha_{25°C} *10^{-6}$ [°C^{-1}]	Mean $\alpha_{25°C} *10^{-6}$ [°C^{-1}]	Glass transition temperature [°C]	Mean glass transition temperature [°C]
C3-TMA-90-01	30		28		191	
C3-TMA-90-02	28	28 ± 2	24	25 ± 3	189	191 ± 3
C3-TMA-90-03	27		23		194	

Table 4-27: Coefficient of thermal expansion α and glass transition temperature measured perpendicular to the fiber direction of samples

C3-TMA-90-01 to 03

Tubes

The changes of sample length over temperature of samples P10-0° and P10-90° are given in figures 4-49 a) and b), respectively. Tables 4-28 and 4-29 provide the coefficient of thermal expansion for each specimen at room temperature (25°C) and below glass transition temperature as well as the glass transition temperature itself. The glass transition temperature can only be measured using the 90° samples as the intersection point of the two tangents above and below glass transition. Both figures present the first and the second heating cycle of the samples to exclude irreversible processes.
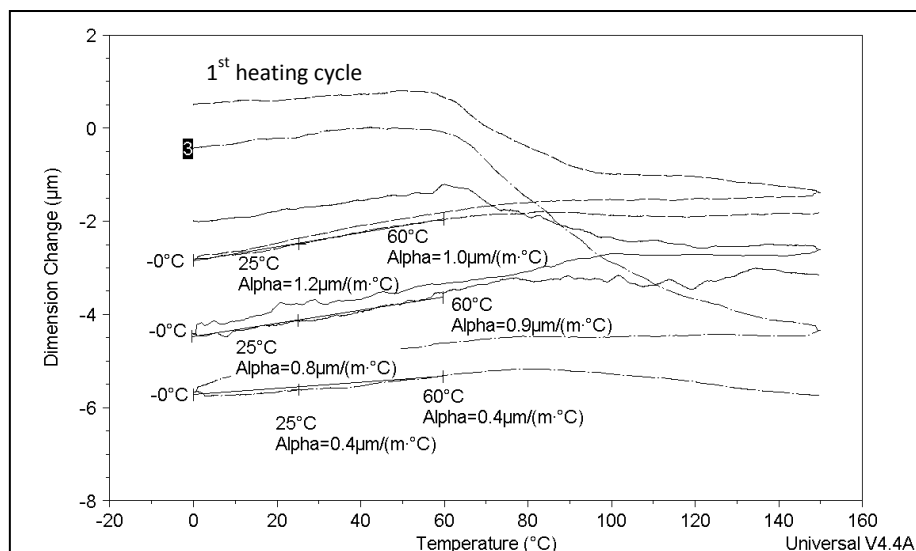
Fig. 4-59 a): Thermal expansion curves (dashed lines) parallel to the fiber direction of samples P10-TMA-0-01 to 03
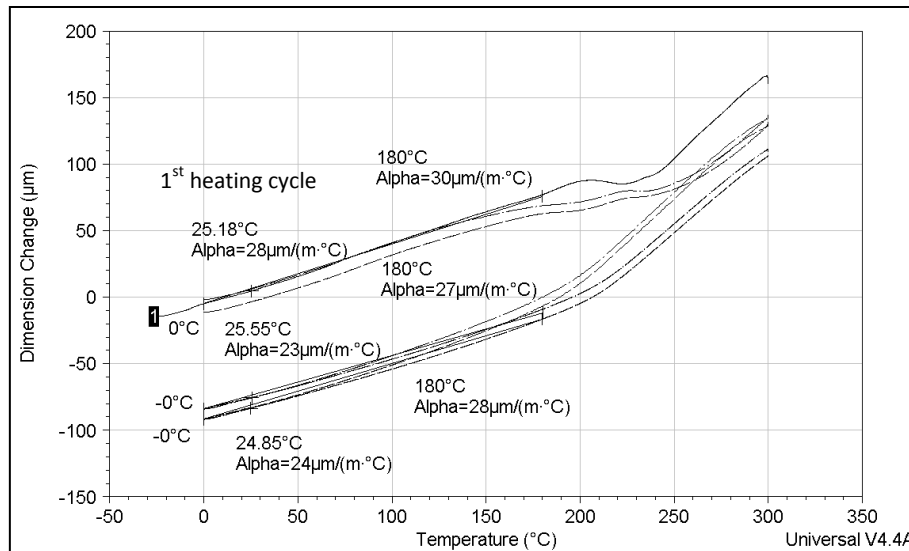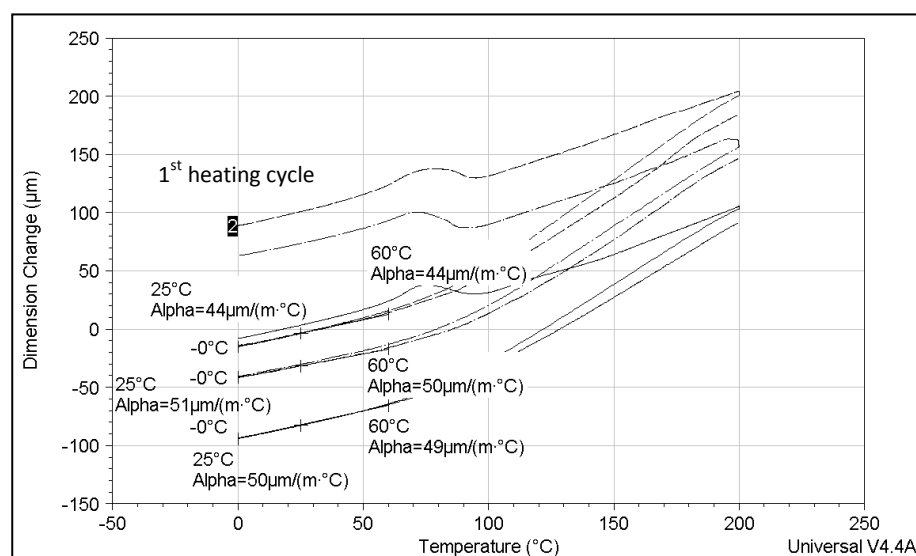

Fig. 4-59 b): Thermal expansion curves (dashed lines) perpendicular to the fiber direction of samples P10-TMA-90-01 to 03

Sample code	$\alpha_{0\text{-}60°C} *10^{-6}$ [°C^{-1}]	Mean $\alpha_{0\text{-}60°C} *10^{-6}$ [°C^{-1}]	$\alpha_{25°C} *10^{-6}$ [°C^{-1}]	Mean $\alpha_{25°C} *10^{-6}$ [°C^{-1}]
P10-TMA-0-01	1,0		1,2	
P10-TMA-0-02	0,9	0,8 ± 0,3	0,8	0,8 ± 0,4
P10-TMA-0-03	0,4		0,4	

Table 4-28: Coefficient of thermal expansion α parallel to the fiber direction of samples P10-TMA-0-01 to 03

Sample code	$\alpha_{0\text{-}60°C} *10^{-6}$ [°C^{-1}]	Mean $\alpha_{0\text{-}60°C} *10^{-6}$ [°C^{-1}]	$\alpha_{25°C} *10^{-6}$ [°C^{-1}]	Mean $\alpha_{25°C} *10^{-6}$ [°C^{-1}]	Glass transition temperature [°C]	Mean glass transition temperature [°C]
P10-TMA-90-01	50		51		77	
P10-TMA-90-02	44	48 ± 3	44	48 ± 4	79	78 ± 1
P10-TMA-90-03	49		50		78	

Table 4-29: Coefficient of thermal expansion α and glass transition temperature measured perpendicular to the fiber direction of samples

P10-TMA-90-01 to 03

5 Discussion

5.1 Architecture of CFRP specimen

The manual measurement of the fiber diameter led to better results than the automated measurement. This can be related mainly to the data loss due to picture processing. Therefore the program also detects "fibers" of 0,6µm in diameter which represent only fragments of a fiber or pixel failures. The huge "fibers" found with a diameter up to 27µm arise from fibers embedded very close to each other and hence cannot be separated by the program. The same counts for the automated calculation of the fiber fraction. The low value reflects the lower average fiber diameter of the automated analysis. Fiber fraction determined with a nominal fiber diameter of 7,1µm led to more reliable results (tab. 5-1). The examination of the void fractions using LOM and CT showed similar results for the C3 laminate but quite a deviation for the C0 laminate (tab. 5-2). A Problem using LOM is that only a single cross section is investigated at one time, whilst CT analysis offers the opportunity to examine a volumetric segment of the specimen and therefore contains much more information. Therefore LOM analysis can be very time consuming until the same information is collected. The low fraction of porosities of the CT measurement can be explained by the rather huge voxel size of $(9,5µm)^3$. Thus porosities smaller than 20µm in diameter are not recognized and hence CT investigation underestimates the fraction of voids.

Laminate	Nominal fiber fraction [%]	Mean fiber fraction Image J [%]	Mean fiber fraction $\emptyset_f = 7,1$ µm [%]
C0	58	$50,7 \pm 0,6$	$57,6 \pm 3,5$
C3	58	$48,4 \pm 0,1$	$56,6 \pm 0,4$

Tab. 5-1: Comparison of the fiber fraction

Laminate	Void fraction CT [%]	Void fraction "Axio Vision" [%]
C0	$\geq 2,7$	$4,0 \pm 0,3$
C3	$\geq 1,1$	$1,5 \pm 0,1$

Tab. 5-2: Comparison of the void fraction

5.2 Mechanical Properties

<u>Laminates</u>

The Young's modulus and the failure stress of the bending samples showed a significant scatter between specimens cut out of different plates especially for three point bending samples C0. The Young's modulus ranged between 118 and 136GPa and the failure stress between 2267 and 2690MPa but also four point bending samples C0 and C3 exhibited a wide scatter. This can be assumed to result from a variation of adhesive strength between the prepregs which is affected by the volumetric fraction of porosity and therefore dependent on the manufacturing process. Therefore slight variations in temperature and pressure during hot pressing of the laminates can lead

to a significant change of the material properties. Furthermore cutting of the samples plays an important role. Fiber direction of samples C0-4P-0-04 and 07 was about 4° referred to the longitudinal axis of the specimen. Hence the Young's modulus of sample 07 and the failure stress of sample 04 are out of range even considering the systematic error of the measurement (fig. 4-27 and fig. 4-28). Further outliers are sample C0-4P-0-12 which exceeded the mean value and sample C0-3P-0-06 which is discussed in the following chapter. In contrast to this wide spread, the average values of the Young's moduli between three-, and four point bending match as listed in table 5-4 and figure 5-1. The Young's modulus perpendicular to the fiber orientation is about 10GPa in both cases. This low value only represents the stiffness of the matrix, as the stiffening effect of the fibers is not exploited (fig. 5-1). The failure stress of the three point bending samples tested parallel to the fiber direction is about 50% higher in case of the C0 samples and 35% in case of the C3 samples (fig. 5-2). Stressing the sample with the same load leads to a higher bending moment in case of four point bending according to the equations given in the standard [5] and therefore to lower values of the failure stress and failure strain. Moreover the tested volume in case of four point bending is much bigger as failure can occur in between the two pressure rams which is another reason for the lower values of the failure stress. The stiffness examined with mechanical testing do correlate with the values determined by the rule of mixture given below [22]. Due to the porosities the strength of the material observed is lower than the strength evaluated with the rule of mixture. For testing in 0° the Voigt-model is used which assumes equal strains for resin and fibers ($\varepsilon_M = \varepsilon_F = \varepsilon$). The stiffness in 90° direction can be predicted with the Reuss-model assuming equal stresses for resin and fibers ($\sigma_M = \sigma_F = \sigma$). Both systems do not consider the different Poisson's ratio of resin and fiber material.

$$E_{0°} = f_F E_F + (1 - f_F) E_M$$

$$\sigma_{0°} = f_F \sigma_F + (1 - f_F) \sigma_M$$

$$\frac{1}{E_{90°}} = \frac{f_F}{E_F} + \frac{(1 - f_F)}{E_M}$$

$E_{0°}$ ... Tensile Young's modulus in 0° fiber direction [GPa] E_F ... Tensile Young's modulus of the fibers [GPa]

$E_{90°}$ ... Tensile Young's modulus in 90° fiber direction [GPa] E_M ... Tensile modulus of the matrix [GPa]

$\sigma_{0°}$ ... Tensile strength in 0° fiber direction [MPa] σ_F ... Tensile strength of the fibers [MPa]

f_F ... Nominal fiber volume fraction [1] σ_M ... Tensile modulus of the matrix [MPa]

Table 5-3 contains all data necessary to calculate these properties and table 5-4 provides the results of the material properties obtained by mechanical testing and using the rule of mixture.

f_F [1]	E_F [GPa]	E_M [GPa]	σ_F [MPa]	σ_M [MPa]
0,58[1]	231[2]	4,67[1]	4433[2]	121[1]

Table 5-3: Properties of the resin and the fibers for calculation of the material properties using the rule of mixture [22]

[1]According to Hexcel HexPly AS4/8552 RC34 AW194 data sheet [24]

[2]According to Hexcel HexTow AS4 carbon fiber data sheet [25]

	Rule of mixture		C0			C3		
			Three point bending		Four point bending	Three point bending	Four point bending	
	0°	90°	0°	90°	0°	0°	0°	90°
Young's modulus [GPa]	136	11	126 ± 8	9,5 ± 1	126 ± 5	149 ± 6	133 ± 4	10,1 ± 0,1
Failure stress [MPa]	2622	-	2438 ± 223	140 ± 3	1644 ± 79	2650 ± 86	1956 ± 186	96 ± 9

Table 5-4: Comparison of the average values of the young's modulus and the failure stress obtained by three-, and four point bending
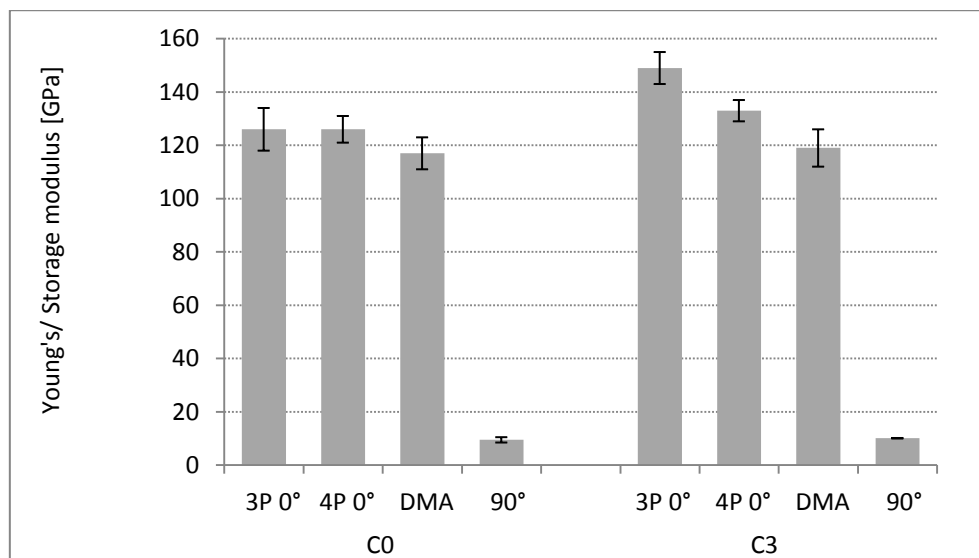

Fig. 5-1: Comparison of the Young's modulus (mean value and standard deviation) of samples C0 and C3 measured alongside fiber direction with three point bending, four point bending and DMA and perpendicular to the fiber direction (three and four point bending)
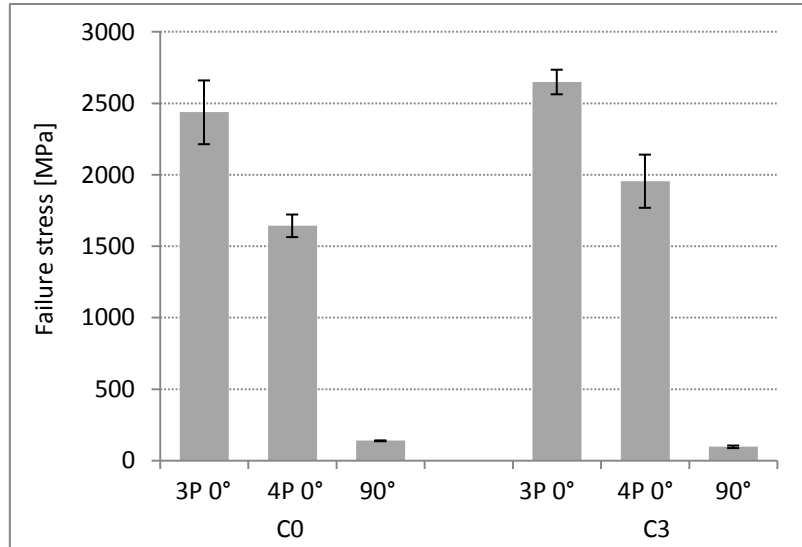
Fig. 5-2 Comparison of the failure stress (mean value and standard deviation) of samples C0 and C3 measured alongside fiber direction with three point bending and four point bending and perpendicular to the fiber direction (three and four point bending)

All samples tested with four point bending show a strong non linear characteristic in areas of higher strain. The standard includes formulas, given below, to eliminate the non linearity and has to be used when the strain exceeds 0,1 times the support span and therefore 8,1mm which was the case for all specimen. Though using this equation leads to unrealistic results as the material appears stiffer as the deflection increases (fig. 5-3 a) and b)) and was therefore only applied for three point bending. The Young's modulus does not change significantly between both equations as it is calculated at very low strains where the curves are nearly identical.

$$\sigma_f = \frac{FL}{bh^2} \left[1 + 8{,}78 \left(\frac{s}{L} \right)^2 - 7{,}04 \left(\frac{sh}{L^2} \right) \right]$$

$$\varepsilon = \frac{h}{L} \left[4{,}7 \frac{s}{L} - 14{,}39 \left(\frac{s}{L} \right)^3 + 27{,}7 \left(\frac{s}{L} \right)^5 \right]$$
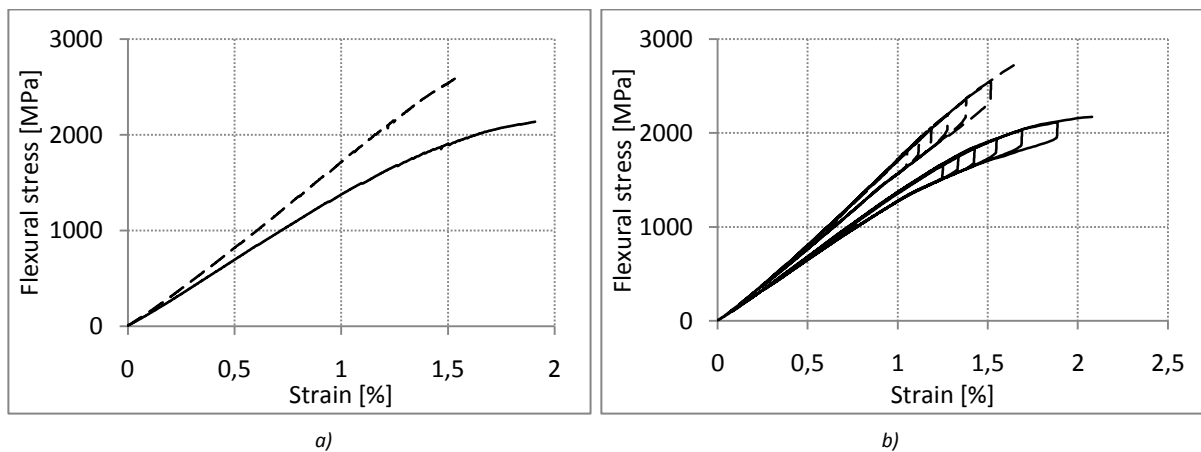

a)

b)

Fig. 5-3 a): Sample C3-4P-0-06; original (solid line) and adjusted curve (dashed line) for high strains

Fig. 5-3 b): Sample C3-4P-0-05; original (solid line) and adjusted curve (dashed line) for high strains

Comparing the Young's modulus of the three point bending test with the DMA results, the latter reveals slightly lower values (table 5-5 and fig. 5-1). This can be explained by the different deformation speed. During bending the sample is loaded quasi-static (1mm/min = 16,7µm/sec) whereas within DMA, the sample is loaded about eight times faster (140µm/sec) resulting in lower values due to the viscoelastic behavior of the matrix material. However samples stressed cyclically before DMA do not show a significant reduction of the elastic properties (113MPa compared to 117MPa without prior mechanical loading). The high Young's modulus of samples C3 tested after being stressed is again a consequence of samples cut out of a different plate.

| Laminate	Young's/Storage modulus [GPa]		
	Three point bending	DMA as received	DMA after mechanical loading
C0	127 ± 8	117 ± 6	113 ± 4
C3	149 ± 6	119 ± 7	131 ± 4

Table 5-5: Comparison of the young's modulus obtained by three point bending test and DMA

Four point bending tests using loading-unloading cycles were performed to verify damage of the laminates by a decrease of the young's modulus between different hysteresis loops. As shown in figure 5-3 the young's modulus depends on the formula used (with or without correction of high strain). Thus attenuation of the material stiffness cannot be deduced and ideally elastic behavior until failure must be assumed.

Three point bending samples collapsed either totally, meaning one crack perpendicular to the fibers underneath the pressure ram and some more cracks parallel to the fibers (fig. 5-4 a), or only some fibers failed on the tension side of the specimen (fig. 5-4 b).

Four point bending samples failed the same way either leaving three fragments with a crack underneath each pressure ram (fig. 5-5 a), or only two fragments with a crack underneath one of the load application lines (fig. 5-5 b). The latter occurred when pressure rams did not touch the sample simultaneously and therefore shear forces and different deflections underneath the pressure rams develop and the flexural moment is not symmetrically any longer. The case of fibers failing without a crack developing throughout the whole thickness of the specimen also arose (fig. 5-5 c).

Generally can be said that there is no difference in type of failure between C0 and C3 samples. Both laminates showed all kinds of failure behavior explained above.
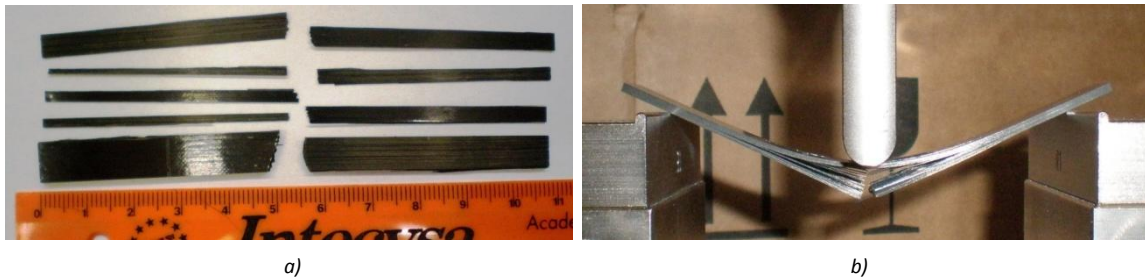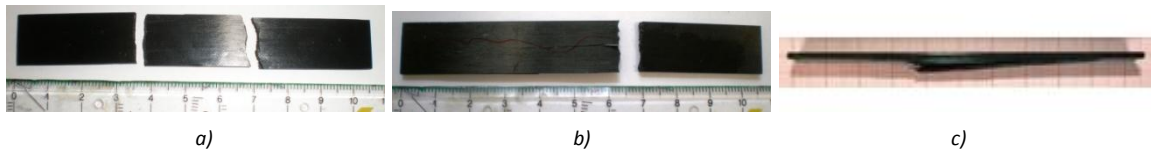
a)   *b)*

Fig. 5-4 a): Sample C0-3P-0-05 after three point bending

Fig. 5-4 b): Sample C0-3P-0-04 still fixed after failure occurred

a)   *b)*   *c)*

Fig. 5-5 a): Sample C0-4P-0-01 after four point bending leaving three fragments

Fig. 5-5 b): Sample C0-4P-0-06 after four point bending leaving two fragments

Fig. 5-5 c): Sample C3-4P-0-05 after four point bending. Failure occurred due to rupture of fibers on the tension side

The absolute values obtained by interlaminar fracture toughness mode I and II are not very representative but correlation of the data between laminates clearly states the higher fracture toughness of composite C3 in both modes. No bridging fibers were observed during mode I testing and therefore fracture toughness is independent of the crack length as depicted in figure 4-29 and 4-31 [28].

Tubes

Considering the torsion test a decrease of the shear modulus can be observed between hysteresis cycles for all four samples tested (table 5-6). Figure 5-6 depicts the shear stress over shear strain curve of sample P10-3 showing that plastic deformation occurs. The decrease of the shear modulus can be seen due to the reduced gradient of the secants from one loop to the other. Figure 5-7 clarifies the attenuation of the shear modulus using a point diagram also showing the failure stress of samples P10-03 and 06. Though it must be considered that reduction of the elastic properties could also originate from continuous slip between sample and grips. Some kind of slip also occurs at the load reversion points as given in figure 5-6.
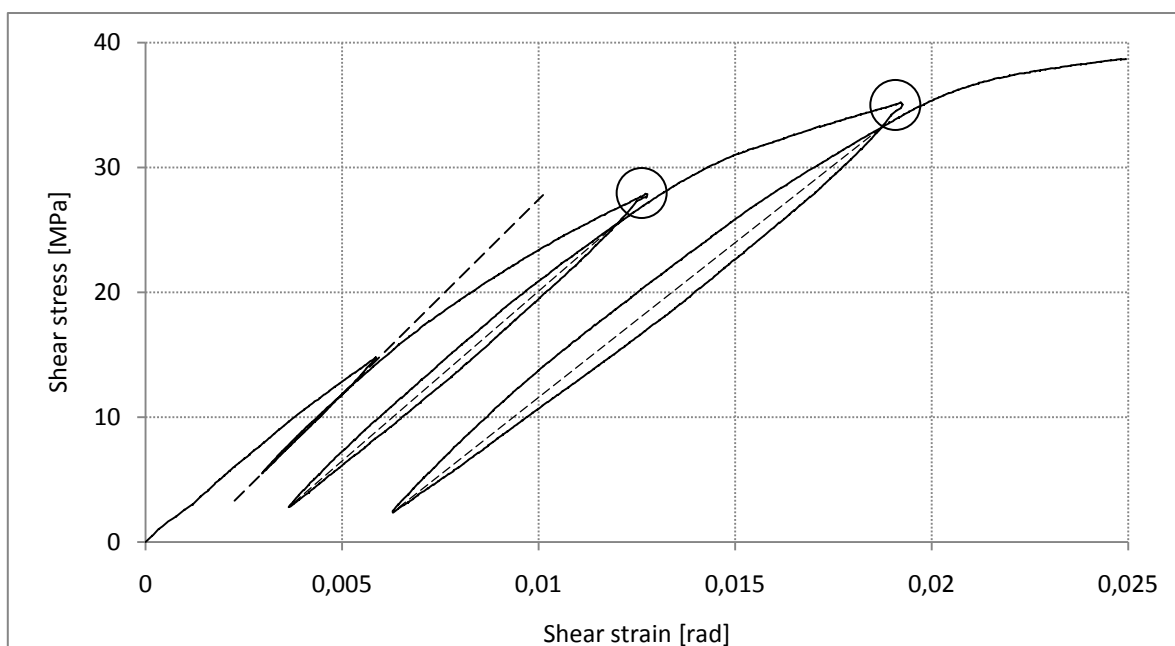
Fig. 5-6: Shear stress versus shear strain of sample P10-03 and secant moduli of hysteresis loops 1-3 (dashed lines). Slip can be identified due to an abrupt drop of the shear strain during load reversion (highlighted areas).
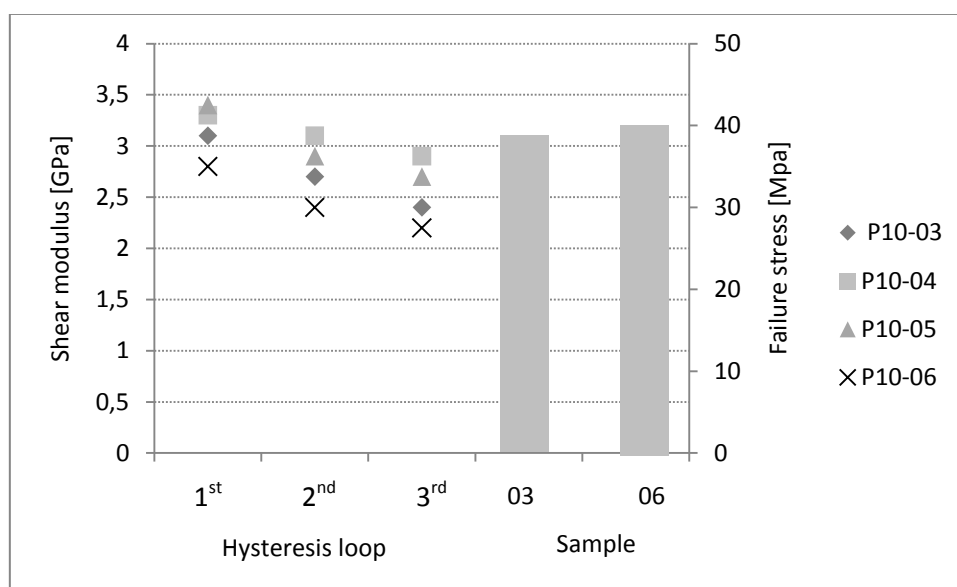
Fig. 5-7: Shear modulus of samples P10-03 to 06 over hysteresis cycles clearly showing attenuation of the material stiffness and failure stress of sample P10-03 and 06

Sample	1st secant modulus [GPa]	2nd secant modulus [GPa]	3rd secant modulus [GPa]	Failure stress [MPa]
P10-03	3,1	2,7	2,4	38,6
P10-04	3,3	3,1	2,9	(33,5)
P10-05	3,4	2,9	2,7	(39,2)
P10-06	2,8	2,4	2,2	39,9

Tab. 5-6: Attenuation of the shear moduli between hysteresis loops and failure stress of torsion samples P10-03 to 06

Numbers in brackets refer to interrupted test

5.3 Artificial delamination (specimen C0-3P-0-06)

As given in figure 4-18, 4-19, 4-20 and table 4-6 sample C0-3P-0-06 failed much earlier, with a maximum failure stress of 773MPa, and also the Young's modulus was significantly lower. The following CT scan revealed two cracks. One parallel to the x-axis and the other parallel to the y-axis (fig. 5-8 b and c). A schematic view is given in figure 5-8 a). Accordingly the crack seems to originate from two different voids "A" and "B" in figure 5-5 b) and c) which are present along 15mm (Position 1 and 2 in figure 5-8 a and 5-9 a). After cutting of the sample for further fractographic investigations a 0,002mm thick and about 50mm long Teflon foil was found in the middle of the sample (fig. 5-9 a). Thus the crack parallel to the x-axis did not propagate through void "A" but the void developed at the Teflon foil during production. Due to stress peaks at the end of the foil a second crack was formed passing through void "B". The sample did not fail due to delamination, but damage occurred as the part limited by the two cracks brake off. Figure 5-9 b) depicts a SEM image at the boarder of the foil showing a smooth and flat area where the foil was located and a fibrous part where the crack propagated. Figure 5-10 shows a 2,5mm long CT segmentation of the sample. Red marks the crack perpendicular to the fiber direction, the blue area the Teflon foil and the brown regions represent voids.
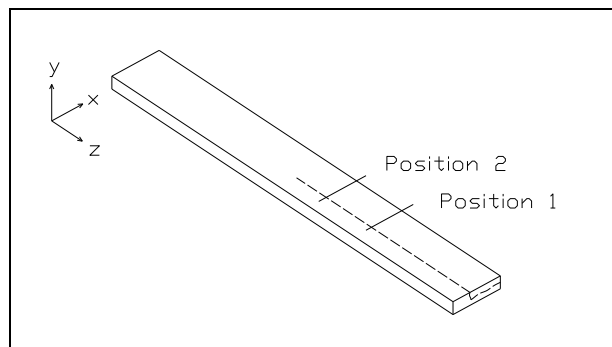

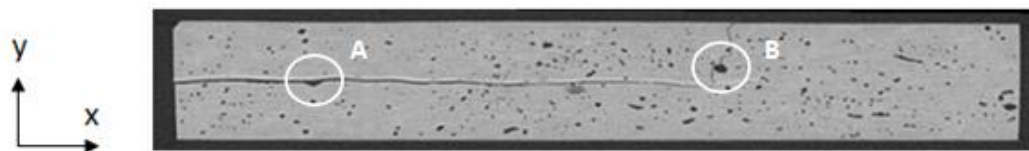*Fig. 5-8 a): Schematic view of sample C0-3P-0-06 showing the crack and CT scan positions 1 and 2*

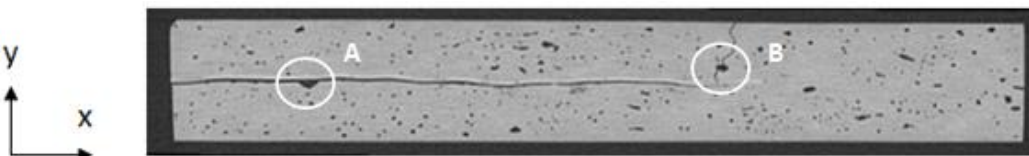*Fig. 5-8 b): CT scan position 1 showing each crack passing through a huge void "A" and "B"*

Fig. 5-8 c): CT scan position 2 showing each crack passing through a huge void "A" and "B"

a)   *b)*
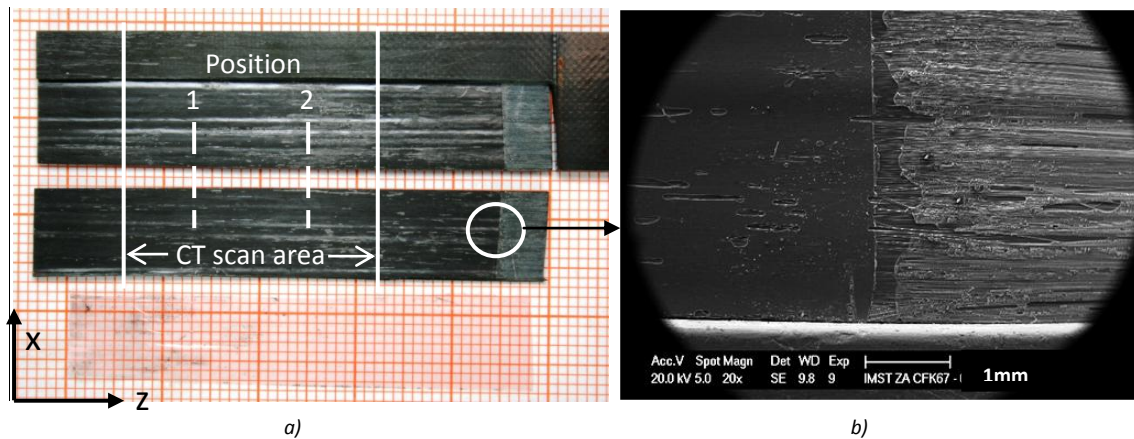
Fig. 5-9 a): Sample C0-3P-0-06 with Teflon foil found in between the layers and CT scan positions 1 and 2

Fig. 5-9 b): SEM image of sample C0-3P-0-06 at the boarder of the Teflon foil. The foil was located at the left part showing a smooth fracture surface whilst the right part shows a fibrous surface.
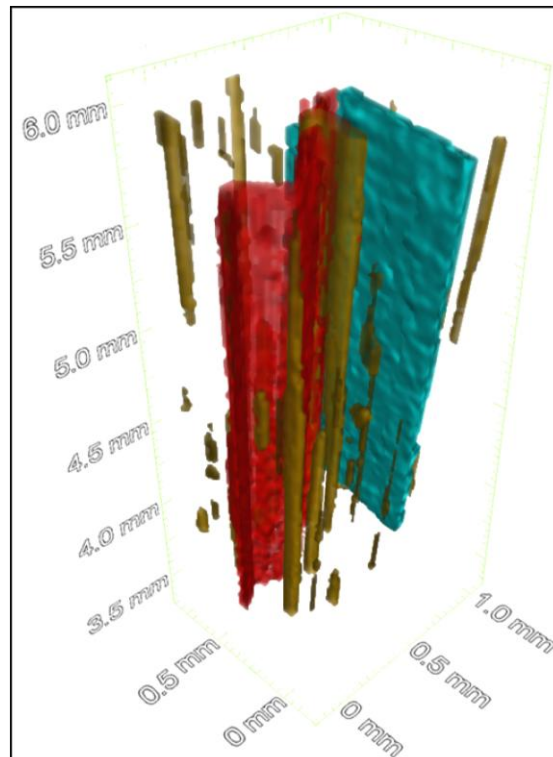
Fig. 5-10: 2,5mm long CT segmentation of sample C0-3P-0-06 showing the Teflon foil (blue), the crack perpendicular to the fiber direction (red) and some longitudinal voids (brown)

5.4 Acoustic Emission

Mechanical testing in combination with AE measurement clearly pointed out that signals are present when cracks start to develop or grow through a sample. However signals were also recorded without being able to relate them to any failure mechanism. For instance peaks at the reversal points during loading-unloading cycles can have their seeds in friction between the sample and the bearings or pressure rams regarding the bending test. But also internal friction between delaminated plies could be the source of these signals which would moreover explain the peaks during unloading of the

sample. To locate the origin of failure a second sensor could be used [10, 12, 20] but this technique is pointless in combination with bending test as failure occurs underneath the pressure rams and therefore distinction whether friction or failure causes the AE signal is not possible. AE measurement during torsion tests were even more difficult to analyze as the noise level was higher. Figure 4-38 e) for example shows much more signals than all the other samples. Nevertheless, the AE count rate increases significantly when the sample is stressed near its failure load as given in figure 4-38 f).

5.5 Thermal Analysis

DMA curves presented above showed a typical progression as found in literature [13, 15]. Glass transition temperature can be identified by determination of the maximum value of the loss modulus or the loss factor or by the middle temperature of the step in the storage modulus curve. The third option can be challenging if the graph does not show a linear behavior before and after the step where the glass transition temperature occurs. Therefore three different glass transition temperatures can be evaluated using only one method of measurement. Glass transition determined from the maximum of the loss factor always shows the highest values according to [13] which is consistent with the present measurements whereas glass transition temperature evaluated from storage modulus is the most matchable with DSC measurements [13] (tab. 5-6). Due to the viscoelastic behavior of the material glass transition temperature measured with dynamic methods always exceeds the ones determined with static techniques [15]. Anyhow glass transition temperature covers a temperature range rather than an exact temperature.

DSC curves showed that the glass transition temperature stays stable for the C0 laminates and decreases slightly for C3 and P10 samples as heating rate increases. According to [29] which considers plastics only (polystyrene) the glass transition temperature increases with the heating rate. This is mainly caused by two reasons. Firstly because temperature in the sample lags behind temperature in the sensor and secondly because glass transition goes along with movement of the molecules which takes time. Therefore the maximum heating rate is limited for plastics. As carbon fiber is a good heat conductor, heating of the material throughout the whole thickness can also be realized at higher rates. Furthermore DSC measurements are very sensitive to size and shape of the sample depending on the parameters that should be evaluated. Sample shapes with a contact surface as big as possible enable fast heat transmission. Specimen weight should be small for melting and crystallization and high for glass transition events. Even sample preparation can influence the results [13].

The glass transition temperature of the tubes was given in the datasheet of the matrix [26] otherwise determination would have been impossible as the step in the curve is hardly evident.

As the coefficient of thermal expansion (CTE) of carbon fiber is negative and the CTE of EP-matrix positive, TMA results along fibers longitudinal axes were close to zero. These samples were very sensitive to environmental disturbance and were therefore only conducted until 180°C for laminates and 150°C for tubes. Thus determination of the glass transition temperature was only done for 90° samples. During the first heating cycle some irreversible effects like cross linking are visible. After heating the sample a second time these effects cannot be observed anymore and the glass transition temperature of the already heated specimen is more distinct.

The comparison of the glass transition temperature depending on the test method (tab. 5-7) revealed a significantly lower value for TMA measurements. This might be due to the rather high loading of the samples with 0,1N which was necessary to fix the sample appropriately. Furthermore slight variations in parallelism of the top and bottom face can induce aberration of the result.

Laminate	Mean glass transition temperature [°C]		
	DMA (Storage modulus)	DSC (3°C/min)	TMA (90°)
C0	222	216	191
C3	217	212	191
P10	-	82	78

Tab. 5-7: Comparison of the glass transition temperatures determined with different methods

6 Conclusions

- The fraction of porosities was proofed by LOM and CT investigation to be about 2% higher in case of C0 samples. However results of the CT and LOM investigation diverged due to the low resolution of the CT measurement.

- CT investigation clearly illustrates that the main portion of pores extends along the fibers and can be found between the prepreg layers (interply) as well as within the layers (intraply). The converted average pore diameter is about 20µm but values range between 1 µm and 75 µm. The longest pores measured had a length of about 4mm.

- Longitudinal splitting follows interlaminar pores, though some samples broke at the loading points indicating that voids need not to be fatal.

- Increased pore volume fraction of the C0 samples causes a decrease of the longitudinal Young's modulus by 5-15% and of the longitudinal strength by 8-16% depending on the test method. Though material properties of laminates of the same curing cycle as well showed a significant scatter.

- The transverse modulus is not affected by the volume fraction of the porosities. The transverse failure stress of the C3 laminates is 36% lower compared to the C0 laminates which represents the difference of three point testing compared to four point testing.

- Damage of the bending samples occurs instantaneously. Hence acoustic emission measurements do not provide significant information about the state of damage. Though a progress of damage was detected for tube-like specimen during torsion tests.

- Torsion tests of tube-like specimen are very accurate when safe clamping of the samples can be assured.

- The scatter of the glass transition temperature reflects the difference in the sensibility of the type of measurement with respect to the transition of the polymer structure.

References

[1] G. W. Ehrenstein: Faserverbundkunststoffe, Carl Hanser Verlag München-Wien, 2006

[2] AVK – Industrievereinigung verstärkte Kunststoffe: Handbuch Faserverbundkunststoffe, Vieweg und Teubner Wiesbaden, 2010

[3] E. S. Greenhalgh: Failure analysis and fractography of polymer composites, Woodhead Publishing Limited, Cambridge, 2009, (ISBN: 978-1-84569-217-9)

[4] J. M. Hodgkinson: Mechanical testing of advanced fiber composites, Woodhead Publishing Limited, Cambridge, England, 2000

[5] DIN EN ISO 14125: Faserverstärkte Kunststoffe – Bestimmung der Biegeeigenschaften, 1998

[6] DIN EN ISO 11357-1: Kunststoffe: Dynamische Differenz Tehrmoanalyse (DSC), Teil1: Allgemeine Grundlagen, 2010

[7] DIN EN ISO 53752: Prüfung von Kunststoffen – Bestimmung des thermischen Längenausdehnungskoeffizienten, 1980

[8] M. Bonnet: Kunststoffe in der Ingenieuranwendung, Vieweg +Teubner Wiesbaden, 2009

[9] ASTM D5528-01(2007)e3: Standard Test Method for Mode I Interlaminar Fracture Toughness of Unidirectional Fiber-Reinforced Polymer Matrix Composites

[10] M. Bourchak et al., Acoustic emission energy as a fatigue damage parameter for CFRP composites, International Journal of Fatigue 29 (2007) p. 457–470

[12] M. Surgeon, M. Wevers: Modal analysis of acoustic emission signals from CFRP laminates, NDT&E International 32 (1999) 311–322,

[13] G. W. Ehrenstein: Praxis der thermischen Analyse von Kunststoffen, Carl Hanser Verlag München-Wien, 2003

[14] L.A. Carlsson, R.B. Pipes: Hochleistungsfaserverbundwerkstoffe, Teubner Verlag Stuttgart, 1989

[15] W. Grellmann, S. Seidler: Kunststoffprüfung, Carl Hanser Verlag München-Wien, 2005

[16] B.S. Hayes, L.M. Gammon: Optical Microscopy of fiber reinforced composites, ASM International, 2010

[17] S. Takeda et al.: Delamination monitoring of laminated composites subjected to low-velocity impact using small-diameter FBG sensors, Composites: Part A 36 (2005) page 903–908

[18] P.L. Sullivan, D. Dykeman: Guidelines for performing storage modulus measurements using the TA Instruments DMA 2980 three-point bend mode: I. Amplitude effects, Polymer Testing 19 (2000) page 155-164

[19] G.E. Dieter: Mechanical Metallurgy 3rd revised edition, Mcgraw-Hill New York- Toronto-London, 2007

[20] Non Destructive Testing-Resource Center, Equipment for acoustic emission testing, http://www.ndt-ed.org/EducationResources/CommunityCollege/Other%20Methods/AE/AE_ Equipment.htm, 18th January 2011

[21] Kitmondo, http://www.kitmondo.com/ViewListing.aspx?lid=242821&prodName=Philips_XL-30, 18th January 2011

[22] I. Skrna-Jakl: Leichtbau mit faserverstärkten Werkstoffen, Vorlesungsskriptum, 2010

[23] H. Hansong, T. Ramesh: Effects of void geometry on elastic properties of unidirectional fiber reinforced composites, Composites Science and Technology 65 (2005) p. 1964–1981

[24] Hexcel, HexPly® AS4/8552 RC34 AW194 data sheet, www.hexcel.com, 14th February 2011

[25] Hexel, HexTow® AS4 carbon fiber data sheet, www.hexcel.com, 14th February 2011

[26] Suter Kunststoffe, L20 epoxy resin data sheet, http://www.swiss-composite.ch, 2nd March 2011

[27] Toho Tenax GmbH, STS40 F13 carbon fiber data sheet, www.tohotenax-eu.com, 14th February 2011

[28] M. Iwamoto, et al: Intralaminar fracture mechanism in unidirectional CFRP composites PartI: Intralaminar toughness and AE characteristics, Engineering Fracture Mechanics 64 (1999) page 721-745

[29] R. Riesen, J. Schawe: Die Glasübergangstemperatur gemessen mit verschiedenen TA-Techniken, Teil 2: Ermittlung der Glasübergangstemperaturen, UserCom 2/2003

[30] H. Schürmann: Konstruieren mit Faser-Kunststoff-Verbunden, Springer Verlag, Berlin, 2005

[31] Aero-Quantum, Boeing 787 materials, http://1.bp.blogspot.com/_TUlGolAmn44/SygW6EhGyfI/ AAAAAAAAADM/esyApTCz4yI/s400/787materials.gif, 20th April 2011

[32] G. Busse, B. H. Kröplin, F. Wittel: Damage and its Evolution in Fiber-Composite Materials: Simulation and Non-Destructive Evaluation, ISD Verlag, 2006

[33] J. P. Hou, C. Ruiz: Measurement of the properties of woven CFRP T300/914 at different strain rates, Composites Science and Technology 60 (2000) page 2829-2834

[34] K. Morioka, Y. Tomita: Effect of lay-up sequences on mechanical properties and Fracture behavior of CFRP laminate composites, Materials Characterization 45 (2000) page 125-136

[35] N. G. Sahooa et al.: Polymer nanocomposites based on functionalized carbon nanotubes, Progress in Polymer Science 35 (2010) page 837–867

[36] J.N.Coleman et al.: Small but strong: A review of the mechanical properties of carbon nanotube–polymer composites, Carbon 44 (2006) page 1624–1652

[37] H. Huang, R. Talreja: Effects of void geometry on elastic properties of unidirectional fiber reinforced composites, Composites Science and Technology 65 (2005) page 1964–1981

[38] Wikipedia, Differential scanning calorimetry, http://en.wikipedia.org/wiki/Differential_scanning_calorimetry, 1st March 2011